

# RADIATION MODELING IN COMBUSTION SYSTEMS USING A GPU-ACCELERATED MONTE CARLO METHOD

By

NICOLAS TRICARD

A thesis submitted to  
the University of Connecticut  
for the degree of  
MASTER OF SCIENCE

Computational Thermal Fluids Lab  
Department of Mechanical Engineering  
School of Engineering  
University of Connecticut  
March 2023

© Copyright by NICOLAS TRICARD, 2023  
All Rights Reserved

## ACKNOWLEDGMENTS

I would like to start by thanking my advisor, Prof. Xinyu Zhao. Your incredible patience and high standards of excellence have pushed me to expand my abilities well beyond what I thought possible, all while supporting a research environment that embraces curiosity and self-motivation. I have you to thank for my tremendous growth throughout my time in your lab, and I will certainly retain the lessons you have taught me throughout life and my career.

Second, my lab-mates: Fraga, Julian, Patrick, Jon, Sam, Joe, Andressa, and (our friendly neighbor) Islam. You have always been open and generous in providing technical advice and thoughts. Our discussions have both shaped my perspective and heightened my curiosity. Fraga, I thank you immensely for joining us at the hackathon, and for your patient explanations of various radiation phenomena. Patrick, your guiding questions and feedback have helped immensely on the side of detonation.

I sincerely thank Drs. Andrey Prokopenko, Wenjun Ge, and Damien Lebrun-Grandié for your technical expertise and for kindly implementing many new features into ArborX to enable the research in this thesis. Your guidance has provided an invaluable contribution to my knowledge of computational science.

I am also grateful to my thesis committee, Prof. Baki Cetegen and Prof. Alexei Poludnenko. I appreciate your being amenable with your time and for your advice. Prof. Poludnenko, I have greatly appreciated our conversations and your expertise during our collaborations.

Lastly, to my siblings, Chris, Jess, and Dave, and my parents Mom and Papa. You have provided the environment to make this thesis possible. I owe you a great deal of gratitude.

# Contents

	Page
<b>1 Introduction . . . . .</b>	<b>1</b>
1.1 Background/Motivation . . . . .	1
1.2 Influences of radiation in combustion . . . . .	2
1.3 Modeling challenge and approach . . . . .	3
1.4 Organization . . . . .	5
<b>2 Background on Radiation in Combustion . . . . .</b>	<b>7</b>
2.1 Fundamentals of radiation . . . . .	7
2.1.1 Basic laws of radiation . . . . .	8
2.1.2 Spectral effects . . . . .	10
2.1.3 Thermal radiation in participating media . . . . .	11
2.1.4 Characterizing the contribution of radiation . . . . .	13
2.1.5 Canonical solutions to the RTE . . . . .	15
2.1.6 Frozen-Field Analysis . . . . .	21
2.2 Influences of radiation in combustion . . . . .	21
2.2.1 Coupling to fluid dynamics . . . . .	21
2.2.2 Radiation in enclosed engines . . . . .	23
2.2.3 Changes to chemistry . . . . .	27
<b>3 Monte Carlo Ray Tracing . . . . .</b>	<b>30</b>
3.1 Forward Monte Carlo Ray Tracing . . . . .	31
3.1.1 Random number selection process . . . . .	32
3.1.2 Raytracing . . . . .	37
3.2 Accelerated approaches to MCRT . . . . .	43
3.2.1 Adaptive Emission Model . . . . .	43
3.2.2 Monte Carlo reformulations . . . . .	44
3.2.3 MPI acceleration . . . . .	49

3.2.4	Ray Tracing in computer graphics . . . . .	54
3.3	Implementation for this Research . . . . .	56
3.3.1	Supplemental Libraries . . . . .	57
3.3.2	Summary of ray tracing procedures presented in this study . . . . .	61
<b>4</b>	<b>Solver Performance . . . . .</b>	<b>66</b>
4.1	One dimensional plane-parallel medium . . . . .	66
4.1.1	Results for a single MPI rank . . . . .	68
4.1.2	Results with multiple MPI ranks . . . . .	72
4.1.3	Results with varying ray counts . . . . .	73
4.2	Backward-Facing Step Combustor . . . . .	76
4.2.1	Case setup . . . . .	77
4.2.2	Results . . . . .	78
4.2.3	Model Performance . . . . .	80
4.3	Direct Numerical Simulation of a Turbulent Pool Fire . . . . .	82
4.3.1	Case Setup . . . . .	82
4.3.2	Verification and Performance of line-by-line MCRT . . . . .	85
4.3.3	Comparison with other radiation solvers using a gray model . . . . .	86
4.4	Transient Small Pool Fire . . . . .	87
4.4.1	Case Setup . . . . .	88
4.4.2	Results . . . . .	88
4.4.3	Profiling . . . . .	91
<b>5</b>	<b>Conclusions and future work . . . . .</b>	<b>94</b>
5.1	Summary of findings . . . . .	94
5.2	Recommendations for Future Work . . . . .	97

## List of Figures

1.1	Run-time breakdown of a Monte Carlo Ray Tracing radiative heat transfer simulation on a backward-facing step combustor (see section 4.2). . . . .	5
2.1	Spectrals lines of CO <sub>2</sub> at 1 bar and 1600 K below 4000 1/cm obtained from a line-by-line database [1]. . . . .	10
2.2	Graphic of a plane parallel medium and a ray being traced. . . . .	18
2.3	The computational domain for the conjugate heat transfer solver from [2]. Various sources of heat transfer rate are labeled, with the red-fonted heat transfer rates accounted for by the conduction solver and the black-fonted heat transfer rates accounted for by the radiation solver. The yellow domain and blue domains are the TBC and metal, respectively. The x direction follows from the flame to the impingement flow. The y and z directions are vertical and into the page, respectively. . . . .	27
3.1	Angle definitions for ray direction from a boundary. $\theta$ is the polar angle and ranges from 0 to $\pi/2$ . $\psi$ is the azimuthal angle and ranges from 0 to $2\pi$ . When a ray is emitted from a point in a medium, a ray may be emitted in any direction across the unit-sphere, and $\theta$ will range from 0 to $\pi$ . . . . .	34
3.2	Visual depiction of a ray traveling through a mesh. . . . .	40
3.3	Visual depiction of a specular ray reflection. . . . .	42

3.4	Flow chart of coupled combustion-CFD and MCRT implementation. The left box refers to the overall coupled code, while the right box details the radiation solver only. The solver at its current state can solve radiation on the Kokkos device (i.e. GPU, if available, else CPU) and CFD on the CPU. A deep-copy is a data transfer from host to device. The ray tracing procedure follows the implementations listed in section 3.3.2. . . . .	58
3.5	A depiction of a ray being traced across multiple MPI ranks simultaneously. Within ArborX, the top-tree is constructed around MPI rank boundaries, and the bottom-trees are constructed of CFD cells. . . . .	62
4.1	A one-dimensional plane parallel medium. Red walls are symmetric and blue walls are cold and black. Ray is in orange. . . . .	67
4.2	Comparison of the absorption source term using variable absorption coefficient $\kappa$ in $\text{m}^{-1}$ with $T=2000\text{K}$ , $N_r=1000$ , $N_{cells}=1000$ on a single MPI rank. . . . .	68
4.3	Variable temperature with $\kappa=10 \text{ m}^{-1}$ , $N_r=1000$ , $N_{cells}=1000$ on a single MPI rank. . . . .	69
4.4	Variable absorption coefficient $\kappa$ in $\text{m}^{-1}$ with $T=2000\text{K}$ , $N_r=1000$ , $N_{cells}=1000$ with eight MPI ranks. . . . .	72
4.5	Variable temperature with $\kappa=10 \text{ m}^{-1}$ , $N_r=1000$ , $N_{cells}=1000$ with eight MPI ranks. . . . .	73
4.6	Variable number of rays emitted per cell ( $N_r$ ) with $\kappa=10 \text{ m}^{-1}$ , $T=2000\text{K}$ , $N_{cells}=1000$ . . . . .	75
4.7	Dimensions of backward-facing step configuration used in this study in addition to a representative line used to sample radiative properties. The sampled line connects the farthest two corners of the bounding box around the domain.	77

4.8	Temperature isocontour of the cross-section(a) and instantaneous streamlines (b) obtained using the <code>multiRegionReactingFoam</code> solver. . . . .	79
4.9	Isocontours of volumetric radiative emission alongside resulting radiative heat flux at the walls. . . . .	79
4.10	MCRT solution results between the present MCRT solver and a well-established Fortran solver of the present backward-facing step after 1.094 seconds of physical time. . . . .	81
4.11	Instantaneous temperature isocontour from the turbulent pool fire used for runtime analysis in this study. The dimension of the geometry is also illustrated.	83
4.12	Mid-plane contours of radiative emissive power and radiative absorption from the Fortran-based solver used in Ref. [3] and the present solver. . . . .	84
4.13	Centerline radiation source term with line-by-line non-gray radiation from the present MCRT solver and the Fortran-based MCRT solver. . . . .	84
4.14	Centerline radiative absorption with gray radiation from the present MCRT solver and the <code>OpenFOAM</code> fvDOM and P-1 radiation solvers. . . . .	87
4.15	An early timestep of the pool fire flame simulation. Isosurface is 0.03 CO <sub>2</sub> mass fraction colored by velocity magnitude in meters per second. Axes dimensions are in meters. . . . .	89
4.16	Isosurface of 0.03 CO <sub>2</sub> mass fraction colored by radiative emission. Wall coloring represents wall radiative heat flux. . . . .	89
4.17	Comparison of center-line temperature profiles of various simulations of the pool fire. . . . .	90
4.18	Profiling results for the GPU. . . . .	91
4.19	Profiling results for the CPU. . . . .	92

# List of Tables

3.1	Variations of the present MCRT solver algorithm. All variations rely on the Kokkos programming model for parallelization and OpenFOAM for CFD computation, while only Bounding Volume Hierarchy and Hybrid approaches use ArborX. Bold solvers are the primary tested versions. . . . .	61
4.1	Maximum normalized standard deviations (using Eq. 4.2) for various MCRT results at various absorption coefficients. . . . .	70
4.2	Maximum normalized standard deviations (using Eq. 4.2) for various MCRT results at various temperatures. . . . .	71
4.3	Average runtimes for each tracing method. . . . .	71
4.4	Maximum normalized standard deviations (using Eq. 4.2) for various MCRT results at various absorption coefficients for with eight MPI-ranks. . . . .	74
4.5	Maximum normalized standard deviations (using Eq. 4.2) for various MCRT results at various temperatures with eight MPI ranks. . . . .	74
4.6	Average runtimes for each tracing method. . . . .	74
4.7	Standard deviations of the percent difference of MCRT and exact solution at various absorption coefficients. Each simulation is run with 1000 computational cells, a temperature of 2000K, and absorption coefficient of $10\text{m}^{-1}$ . .	75
4.8	BFS runtime comparisons with 1 ray emitted per computational cell. . . . .	80

4.9	BFS runtime comparisons with 10 rays emitted per CFD cell. . . . .	81
4.10	Comparison of MCRT runtimes with line-by-line radiation for a single snapshot of a DNS of a turbulent pool-fire. . . . .	86
4.11	Comparison of MCRT runtimes of gray radiation within a single-snapshot of a DNS of a turbulent pool-fire. . . . .	87
4.12	Single time-step runtime profiling. . . . .	92
4.13	Mean runtime contribution of radiation per timestep compared to total runtime. Standard deviations are presented in parentheses. List CPU runtimes consist of radiation parallelized on 30 CPU processors, and CFD calculation occurring on 1 processor. GPU runtimes consist of radiation running on the GPU and CFD calculated using 1 CPU processor. . . . .	93

## ABSTRACT

Thermal radiation contributes significantly to the dynamics and heat transfer within combustion systems. Appropriately capturing its influences during the modeling procedure is essential for a comprehensive prediction of the flame. Monte Carlo Ray tracing (MCRT) is the most robust and accurate method of modeling radiation but is also considered to be the most computationally expensive. Therefore, in order to gather the most accurate depiction of thermal radiation, enhanced mathematical techniques and computational approaches must be implemented for an efficient use of MCRT. Several alternatives have been introduced including backward Monte Carlo, reciprocal Monte Carlo, and null-collision Monte Carlo. Above all, the field of graphics processing has demonstrated the potential of Graphics Processing Units (GPUs) and Bounding Volume Hierarchies (BVHs) to the radiation modeling procedure.

This thesis presents work in the development of a GPU-accelerated MCRT solver with line-by-line non-gray modeling. The solver is connected to the OpenFOAM open-sourced CFD platform to enable transient simulations of joint combustion-radiation calculations. Distributed-memory capabilities are enabled through the use of the Message Passing Interface (MPI). Parallel programming is applied using the Kokkos C++ library for an interchangeable parallel computing backend and performance-portability across CPUs and GPUs. The ArborX geometric search library is applied for a Bounding Volume Hierarchy implementation.

The model is applied to four geometries of varying degrees of complexity. Solver performances are presented for a 1-D plane-parallel participating medium, a 3-D backward-facing step combustor, a direct-numerical simulation of a small pool fire, and a 3-D transient simulation of a pool fire. Observations are also made regarding the influences of radiation in the various configurations. Verifications show excellent agreement between the solvers

with respect to analytical solutions and established radiation models for both 1-D and 3-D geometries with non-gray modeling. Single-timestep frozen-field analyses show GPUs accelerate MCRT up to almost 400 times in research-relevant geometries. The Bounding Volume Hierarchy (BVH) is shown to be less efficient in a shared-memory environment, but there remains a potential advantage for its application in distributed-memory simulations. Analysis of MCRT in transient simulations showed a significant reduction in temperatures of 600K or more compared to simulations without radiation. Loading the line-by-line database contributes significantly to the overall computational cost at each time step, and future work involves minimizing this cost while enabling synchronization between CPUs and GPUs.

# Chapter One

## Introduction

### 1.1 Background/Motivation

The study of thermal radiation in combustion has not only theoretical interest but also great practical importance. Radiant emission from crown fires, for example, has been shown to be the dominant mode of heat transfer and may lead to significantly enhanced flame spread [4]. Conditions for prevalent heat transfer through radiation are also present in combustion devices for useful energy conversion such as gas-turbine engines and steam boilers. Many performance-critical applications operate at high temperatures for optimal thermal efficiency, often exceeding the melting points of the surrounding materials, which requires optimal design of thermal management systems such as thermal barrier coatings. An understanding of thermal radiation is necessary to gauge its dynamic, non-linear, and non-local role in the listed combustion systems and others.

An understanding of radiant heat transfer in combustion can be difficult to achieve experimentally, however, due to the multitude of environmental variables like weather, prohibitively high temperatures that can break sensors and equipment, and the high number of independent variables in the problem. As such, computational tools have become a valuable resource in predicting flame properties under safe and controlled conditions. Modeling of combustion often employs computational fluid dynamics (CFD) combined with a model for

the chemical kinetics of the chemical reaction network. Radiant heat transfer is simulated using a separate radiation model, which predicts the redistribution of thermal energy through electromagnetic wave/photon propagation. In such multi-physics simulations, computational resources may quickly become a limiting factor. For example, the application of the highest fidelity models (i.e., detailed chemical mechanism combined with Kolmogorov-scale cell sizes and line-by-line accurate non-gray radiation modeling) in a combined simulation is computationally prohibitive beyond laboratory-scale flames. Extensive research has been devoted to reducing the computational expense of physical modeling tools while maintaining the necessary degree of fidelity to achieve physically correct results.

This thesis will focus on improving the performance of radiation models in combustion systems. The highest fidelity radiation model, Monte Carlo Ray Tracing, where random rays are emitted and traced through the CFD geometry, is applied alongside enhancements inspired by the computer graphics community: Graphics Processing Units (GPUs) and Bounding volume hierarchy (BVH) data structures. Line-by-line accurate non-gray modeling is used to account for spectral influences within the medium, and various ray-tracing algorithms are proposed.

## 1.2 Influences of radiation in combustion

A brief summary of known influences of radiation in combustion systems is listed here, with a more detailed literature survey provided in Chapter 2. Previous research has highlighted recurring trends, as discussed in reviews from Modest and Haworth [5], Coehlo [6], and Liu et al. [7].

- Radiation contributes thermal energy at the same order of magnitude as convection to the boundaries of many enclosed combustion systems such as aeronautical combustors [8, 9]

- Radiation has significance in pollutant formations (e.g.  $\text{NO}_x$  and soot) and highly temperature-sensitive phenomena due to its redistribution of thermal energy [10, 11, 12]
- Sooting (i.e. luminous) flames often have more pronounced thermal radiation characteristics [5]

Regarding modeling of radiation in combustion simulations:

- Neglecting radiative emission often results in temperature overprediction [13]
- Neglecting radiative absorption often results in temperature underprediction [12]
- Accounting for turbulence-radiation interaction (TRI) increases radiative emission and reduces temperatures [6]
- Non-gray modeling of radiation can increase radiative re-absorption compared to gray modeling [14]

Misrepresentation of radiation in combustion modeling can lead to significant errors in the prediction of flame properties. These errors may present themselves, for example, in 200 K differences of peak flame temperature in gas-turbines [13], 50% under-predictions of heat loss from a piston engine [5], or 90% underpredictions of heat transfer from forest fires [4]. Therefore, comprehensive models of combustion phenomena should include the modeling of radiation to some degree.

### 1.3 Modeling challenge and approach

A number of models and solvers for the radiative transfer equation (RTE) have been introduced to model thermal radiation while minimizing computational burden. Of those, many rely on complex mathematical assumptions and simplifications, such as the P-N method [15], which can be difficult to derive and implement [16].

The Monte Carlo Ray Tracing (MCRT) method stands out as the most accurate, robust, and conceptually simple of the available models [6, 17, 18], and is regarded by many to be the best radiation solver as computational power increases [19]. In MCRT, random rays are initialized and traced from their source computational cell to other cells in the domain to stochastically approximate the transport of radiation throughout the geometry. The resulting process can be intuitively thought of as the tracing of ‘photon packets’ traveling through the domain. As a result of this approach, MCRT can account for many of the same effects that electromagnetic rays undergo during their travel.

Although MCRT is often considered the most accurate, it has also been viewed traditionally as the most computationally expensive. This additional cost results from the stochastic nature of MCRT. A large sample size of rays must be emitted and traced to obtain a statistically meaningful solution. Too few rays may result in excessive noise, while too many require a longer simulation runtime. In most situations, the ray-tracing procedure, in particular, is a bottleneck [20], as shown in Fig. 1.1, which presents the runtime profiling for a decoupled gray simulation of radiation in a backward-facing step combustor. The limitations imposed by this bottleneck significantly inhibit the use of MCRT in combustion simulations. So far, the MCRT methods are mostly employed in decoupled form [21] where single timestep is used for analysis.

Recently, Graphics Processing Units (GPUs) have demonstrated a significant potential to accelerate the Monte Carlo ray tracing process [22, 23] by up to three orders of magnitude [24]. Speedups at this level would significantly improve the applicability of MCRT in radiation modeling. Meanwhile, programming models such as Kokkos, which enable the use of an interchangeable parallel back-end, allow for easier implementation and code portability on CPUs or GPUs without any changes in the coding syntax [25].

In this thesis, we implement an accelerated implementation of MCRT that is coupled with the open-sourced CFD platform `OpenFOAM` [26]. This implementation relies on the Kokkos programming model for parallel computing on high performance computers [27]. Also, the

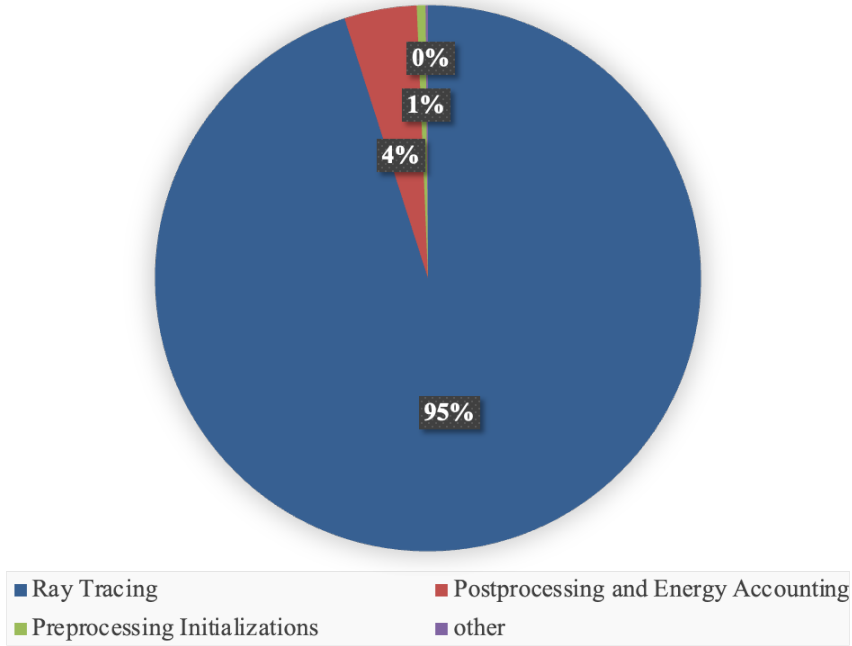


**Figure 1.1** Run-time breakdown of a Monte Carlo Ray Tracing radiative heat transfer simulation on a backward-facing step combustor (see section 4.2).

solver is implemented to utilize distributed-memory computing platforms through the use of the Message Passing Interface (MPI). And finally, as an alternative to a standard ray tracing procedure, a geometric search library named ArborX [28] is introduced to implement a bounding-volume hierarchy data structure with backward Monte Carlo ray tracing (see section 3.3). The present thesis will demonstrate how these changes can be used to bring speedup to the ray tracing procedure for thermal radiation in participating media without sacrificing accuracy.

## 1.4 Organization

In Chapter 2, we present a background on the fundamentals of thermal radiation and its importance in combustion. Then, in Chapter 3, various Monte Carlo-based methods of solving the RTE are presented, including an overview of the present MCRT approaches, the supplemental libraries used, and a description of the solvers' coupling to OpenFOAM. Chapter 4

provides a verification of the solver in a plane-parallel medium and a demonstration of its performance using a backward-facing step combustor, a direct numerical simulation of a small turbulent pool fire, and a transient pool fire. Observations are made regarding the influence of radiation and computational speedup for each configuration. Finally, conclusions and future work are discussed in Chapter 5.

# Chapter Two

## Background on Radiation in Combustion

### 2.1 Fundamentals of radiation

The term *radiative heat transfer* commonly refers to the transfer of thermal energy through electromagnetic waves [29]. This transfer occurs at the speed of light, which is  $2.998 \times 10^8$  meters per second in a vacuum. This results in timescales much faster than the flow and chemical timescales within a combustion system. The effects of thermal radiation can be seen in everyday life. Common examples include the sun, a campfire, and hot pavement. Wavelengths range from picometers ( $10^{-12}$  m) for gamma rays to megameters ( $10^6$  m) for ultra-low frequency radio waves. For thermal radiation in combustion systems, relevant wavelengths generally fall between 1 and 15  $\mu\text{m}$  ( $10^{-6}$  m), in the infrared part of the electromagnetic spectrum [7].

Transport of thermal radiation is known to have a non-local nature. Radiation emitted at one point in space can impact the energy and temperature at another point very far away. This is in contrast to conductive and convective modes of heat transfer where thermal energy is transferred through direct contact (local phenomena). Relevant fundamental laws for radiation in combustion systems are briefly reviewed below. Readers can refer to [18, 19] for more thorough descriptions.

### 2.1.1 Basic laws of radiation

#### The idealized ‘Black body’

The term *black body* refers to a theoretical object that can absorb all incident radiation. The term *black* is used because a body that absorbs perfectly does not reflect any light and therefore appears to be black. In addition, according to arguments posed by Kirchhoff [18], black bodies are also ideal emitters. This idealized nature results in black bodies often appearing in radiation literature.

The emission spectrum of a black body was derived by Max Planck, and is shown in Eq. 2.1, as

$$E_{bv}(T, \nu) = \frac{2\pi\hbar\nu^3 n^2}{c_0^2 \left[ e^{\frac{\hbar\nu}{kT}} - 1 \right]} , \quad (2.1)$$

where  $\hbar$  is Planck’s constant,  $\nu$  is the wave frequency,  $n$  is the refractive index of the medium,  $c_0$  is the speed of light in a vacuum,  $k$  is the Boltzmann constant, and  $T$  is the temperature of the body. The wave frequency can be related to the wavelength  $\lambda$  as,

$$\lambda = \frac{c}{\nu} , \quad (2.2)$$

where  $c$  is the speed of light in the medium. When Eq. 2.1 is integrated across the electromagnetic spectrum (from  $\nu = 0$  to  $\nu = \infty$ ), the overall emissive power from the surface of a black body is evaluated as

$$E_b(T) = n^2 \sigma T^4 , \quad (2.3)$$

where emissive power has dimensions of [ power / area on surface ].

A more fundamental quantity of radiation is the radiative intensity  $I$  which has a dependence on direction and wavelength. Intensity defines the emission in dimensions of [ power / area / unit solid angle ]. A “solid angle” is a description of a differential area along the unit sphere, similar to an angle on the unit circle.

For a black body, the intensity has no directional dependence (i.e. is *diffuse*). Black body emissive power can be evaluated from intensity by integrating over the hemispherical

solid angle of emission from a surface, as

$$E_b(\mathbf{r}, T) = \int_{2\pi} I_b(\mathbf{r}, \hat{\mathbf{s}}, T) d\Omega , \quad (2.4)$$

where the variable of integration,  $\Omega$ , is the solid angle,  $\hat{\mathbf{s}}$  is direction, and  $\mathbf{r}$  is the point of interest. The solution of the integration requires accounting for the change in perspective of the unit area on the surface at different angles and results in

$$I_b(T) = \frac{E_b(T)}{\pi} . \quad (2.5)$$

### Kirchhoff's Law

Kirchhoff's law proves that a black body is both an ideal emitter and absorber and can be described through a simple thought experiment, as follows. Two systems are constructed consisting of an enclosure of black-body surfaces surrounding an object. The object in the first system is a black body, and the object in the second system is a non-ideal absorber. Both systems are thermally insulated from the surroundings. According to the second law of thermodynamics, after a long period of time, the temperatures in both systems will independently equalize to constant values. This implies that the energy emitted and absorbed by the object and the surroundings in each system should be the same. Kirchhoff postulated that since a black body is a better absorber than the gray body, the second law requires it to also be a better emitter. And because the listed 'gray body' can be any non-ideal absorber, then a black body is the most ideal emitter. Further continuation of this argument reveals that the ratio of emission of any object to that of a black body must also equal the ratio of the absorption of that object to that of a black body and that this argument applies to emission at any wavelength  $\eta$  (inverse of  $\lambda$ ) and any direction  $\theta$  for in-going or out-going electromagnetic rays. Kirchhoff therefore established the equality of spectral, directional emissivity  $\epsilon_{\eta\theta}$  and spectral, directional absorptivity  $\alpha_{\eta\theta}$  at thermal equilibrium, as shown in Eq. 2.6,

$$\epsilon_{\eta\theta} = \alpha_{\eta\theta} . \quad (2.6)$$

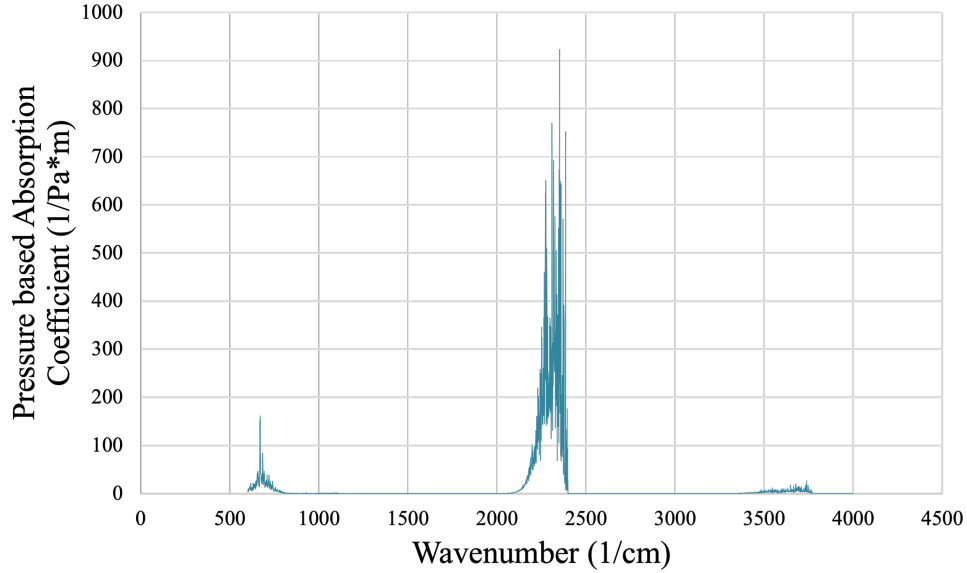


**Figure 2.1** Spectrals lines of  $\text{CO}_2$  at 1 bar and 1600 K below 4000  $1/\text{cm}$  obtained from a line-by-line database [1].

### 2.1.2 Spectral effects

The black body spectrum discussed in section 2.1.1 can approximate the emission spectrum from the surface of many solid materials but is discouraged for use with gas emission. Most solid structures have a multitude of modes of oscillations, from the crystal-lattice structure down to the molecular energy states [30]. As a result, the emission spectra of solids are often continuous and can be approximated as a constant fraction of the black body emission spectrum (i.e. gray) [19]. However, gases are restricted to the oscillation modes of the natural energy states of the individual molecules in the mixture. Quantum mechanics postulates that the energy states of molecules are discrete, and therefore the change in energy states and resulting emission spectra are also discrete [31].

The largest molecular contributors to emission in most hydrocarbon flames are  $\text{CO}_2$ ,  $\text{CO}$ ,  $\text{H}_2\text{O}$ , and soot. Figure 2.1 shows the absorption coefficient spectrum of  $\text{CO}_2$  [7]. *Ab initio* modeling and experimental data are used to obtain approximations for the emission spectra of a molecule at a specified pressure and temperature [31]. This information has been

collected into a series of online databases such as HITEMP [32], which are used to predict absorption coefficients for given gaseous thermodynamic states at different ray wavelengths.

Radiation from soot can make the emission spectra of flames much more continuous. Soot particles are generated through the agglomeration of unburnt hydrocarbons [33]. The resulting particulates contribute much to the visual yellow glow seen in flames, ergo sooting flames are known as *luminous*. Soot particles have sizes of only tens of microns, and volume fractions of order  $10^{-4}\%$  to  $10^{-6}\%$ , but often contribute the majority of radiation from a flame when present [5].

### 2.1.3 Thermal radiation in participating media

The interaction of gases with thermal radiation is more complex than the interaction of surfaces with radiation. The governing equation to describe radiation in an absorbing-emitting medium is the radiative transfer equation (RTE),

$$\frac{dI_\eta}{ds} = \hat{\mathbf{s}} \cdot \nabla I_\eta = \kappa_\eta I_{b\eta} - \kappa_\eta I_\eta - \sigma_{s\eta} I_\eta + \frac{\sigma_{s\eta}}{4\pi} \int_{4\pi} I_\eta(\hat{\mathbf{s}}) \Phi_\eta(\hat{\mathbf{s}}_i, \hat{\mathbf{s}}) d\Omega_i , \quad (2.7)$$

where  $\eta$  represents wavenumber (the inverse of wavelength) and  $i$  marks an incident direction. Also,  $I_\eta$  is the ray intensity at wavenumber  $\eta$ ,  $\hat{\mathbf{s}}$  is the direction vector (with both a direction and a location),  $s$  is a unit path length along this vector,  $\kappa_\eta$  is the absorption coefficient at wavenumber  $\eta$ ,  $I_{b\eta}$  is the black-body intensity at wavenumber  $\eta$ ,  $\sigma_\eta$  is the scattering coefficient at wavenumber  $\eta$ , and  $\Phi_\eta(\hat{\mathbf{s}}_i, \hat{\mathbf{s}})$  is the scattering phase-function at wavenumber  $\eta$  (representing the probability a ray from direction  $\hat{\mathbf{s}}_i$  is scattered into direction  $\hat{\mathbf{s}}$ ). This equation describes how the intensity of a pencil of rays changes along a path length  $\hat{\mathbf{s}}$ . A ray intensity decreases due to absorption ( $\kappa_\eta I_\eta$ ) and out-scattering ( $\sigma_{s\eta} I_\eta$ ) and will increase due to further emission along the path-length ( $\kappa_\eta I_{b\eta}$ ) and scattering of rays from other directions into the path length of interest ( $\frac{\sigma_{s\eta}}{4\pi} \int_{4\pi} I_\eta(\hat{\mathbf{s}}) \Phi_\eta(\hat{\mathbf{s}}_i, \hat{\mathbf{s}}) d\Omega_i$ ).

The RTE, Eq. 2.7, represents the equation that must be solved for thermal radiation to be accurately accounted for in combustion simulations. The intensity at any point, direction,

and wavelength in the medium must be evaluated in order for the net change in energy due to radiation at each point to be known. The existence of both an integral and a differential in Eq. 2.7 makes the RTE an integro-differential equation. This requires knowledge of both local phenomena and the influence of remote phenomena on local conditions. This all-to-all nature is one of the reasons for the immense computational difficulty of solving the RTE. In addition, as is explained in section 2.1.2, in a non-gray medium the radiative emission and absorption also depend on the wavenumber  $\eta$ . This introduces an additional degree of complexity to the problem, especially in gases where emission and absorption are highly intermittent across the spectrum.

The absorption coefficient,  $\kappa_\eta$  and scattering coefficient  $\sigma_\eta$  are often combined into the extinction coefficient  $\beta_\eta$ . Equation 2.7 can then be rewritten as

$$\frac{dI_\eta}{ds} = \beta_\eta [S(\tau_\eta, \hat{\mathbf{s}}) - I_\eta] , \quad (2.8)$$

where  $S_\eta(\hat{\mathbf{s}}', \hat{\mathbf{s}})$  is the ray-intensity source term. Eq. 2.8 demonstrates that the intensity of the pencil of rays,  $I_\eta$ , increases due to a source term and decreases proportional to it's current intensity. The extinction coefficient  $\beta_\eta$ , is often divided from both sides of Eq. 2.7, and the resulting  $\beta_\eta ds$  term is known as the differential optical distance,  $d\tau_\eta$ . Equation 2.8 can be integrated along an arbitrary optical path length  $\tau_\eta$ , resulting in

$$I_\eta(\tau_\eta) = I_\eta(0)e^{-\tau_\eta} + \int_0^{\tau_\eta} S_\eta(\tau'_\eta, \hat{\mathbf{s}})e^{-(\tau_\eta - \tau'_\eta)} d\tau'_\eta . \quad (2.9)$$

Equations 2.7 and 2.9 display an important trait of thermal radiation that is conceptually obvious, but has significant consequences on the modeling procedure: the change in intensity is a function of the current intensity. In other words, the intensity of a pencil of rays at one location cannot be known without knowledge of the ray's intensity directly before. As a result, one cannot accurately predict the variation of intensity of a ray without knowledge of the ray history during traversal. This ordered nature introduces modeling difficulties as will be discussed in Chapter 3.

### 2.1.4 Characterizing the contribution of radiation

A high-level estimation of the contribution of radiation is desired by many scientists and engineers, and a complete solution to the RTE (Eq. 2.7) within their simulated domain is often not necessary to accomplish this. The following physical parameters fundamentally determine the significance of radiative participation within a system.

#### Optical thickness

The optical thickness determine the tendency for a medium to absorb any emitted radiation. The intensity of a pencil of rays at location  $x$  in an absorbing and non-scattering medium can be evaluated as,

$$I_\eta(x) = I_\eta(0) \exp\left(-\int_0^x \kappa_\eta \, ds\right), \quad (2.10)$$

where  $I_\eta(0)$  is the originating intensity of the ray. This equation is known as Beer's law. The quantity in the exponential is known as the optical thickness,  $\tau_\eta = \int_0^x \kappa_\eta \, ds$ , which is a description of the opacity of a medium.  $\tau_\eta$  is a function of not only the tendency for a fluid element to absorb the energy of passing radiation, defined by the absorption coefficient  $\kappa_\eta$ , but also the overall path length the pencil of rays has travelled  $x$ . For a rough estimation, a representative length scale in the geometry  $l_{tot}$  may be used to obtain representative optical thickness of the geometry. Common length scales include the width of a combustion chamber or the height of a pool fire. If one assumes the absorption coefficient remains constant along the path length,  $s$ , the equation for optical thickness can be reduced to

$$\tau_\eta = \kappa_\eta l_{tot}. \quad (2.11)$$

With this simplification, the optical thickness  $\tau_\eta$  becomes a convenient non-dimensional parameter that defines the propensity for a medium to absorb any emitted radiation. Optical thickness values of 1, 2.303, 4.605, and 6.908 define the values necessary to diminish intensities by 36.8%, 90%, 99%, and 99.9%, respectively. Comparing optical thicknesses of

a radiating system to these values may provide an indication if a full solution to the RTE is required or if simplifications may be applied. Media with  $\tau \ll 1$  tend to absorb very little and are known as *optically thin*. Under these conditions, the *optically thin assumption (OTA)* can be applied, where radiation contributes only a volumetric energy loss to the local fluid differential volume, and all radiative absorption is ignored [34]. Media with high absorption coefficients and/or long length scales are known as *optically thick*. Under these circumstances, the absorption component of the RTE becomes more significant and must be modeled. Very optically thick media that find radiative re-absorption to occur on very small length scales relative to the geometry can model radiation using the *diffusion approximation*, where radiation is assumed to act like conductive diffusion [34]. Under moderate absorption coefficients, the full RTE must be modeled for both emission and absorption throughout the volume [18].

Many instances of radiative gases call for an averaged quantity of absorption coefficient across the spectrum. The Planck-mean absorption coefficient is often used in this context, defined as

$$\kappa_p = \frac{\int_0^\infty \kappa_\eta I_{b\eta} d\eta}{\int_0^\infty I_{b\eta} d\eta} = \frac{\pi}{\sigma T^4} \int_0^\infty \kappa_\eta I_{b\eta} d\eta. \quad (2.12)$$

Separate Planck-mean absorption coefficients can be defined for each of the more significant radiatively participating components of the mixture (often CO<sub>2</sub>, H<sub>2</sub>O, CO, CH<sub>4</sub>, and soot for hydrocarbon flames). The net Planck-mean absorption coefficient can then be evaluated as the sum of each weighted by their respective mole fractions. Finally, an overall optical thickness can be defined as  $\tau = \kappa_p l_{tot}$ .

## Radiant fraction

Within combustion systems, a comparison of radiative and chemical heat source terms can also provide perspective as to the relevance of radiation. As discussed by Liu et al. [7], the

radiant fraction can be evaluated as

$$\chi_R = \frac{\dot{Q}_{emi} - \dot{Q}_{abs}}{\dot{Q}_{chem}} = \frac{\int_V 4\pi\kappa_p\sigma T^4 dV - \int_V \left[ \int_0^\infty (\kappa_\eta \int_{4\pi} I_\eta d\Omega) d\eta \right] dV}{\rho_F u_F \Delta h_c \pi d_F^2 / 4}, \quad (2.13)$$

where the numerator defines the radiative divergence of heat flux and the denominator quantifies the contribution of heat through chemistry within the flame.  $d_F$ ,  $\rho_F$ , and  $u_F$  are a length scale, density, and representative velocity for the system. The definition can be reformulated into

$$\chi_R = \left( \frac{4V_f l}{\pi u_F d_F^2} \right) \left( \frac{4\kappa\sigma T_p^4}{\rho_F \Delta h_c} \right) \left( 1 - \frac{\dot{Q}_{abs}}{\dot{Q}_{emi}} \right). \quad (2.14)$$

The first term considers the flow residence time; larger volumes and slower velocities result in a longer period for radiation to have its effect. The second term is inverse of the characteristic radiation cooling time. The third term is the flame transparency. This term quantifies the degree of re-absorption in the flame. A high degree of re-absorption will have a lower flame transparency. Overall, the radiant fraction is a useful metric to measure radiant loss in flames relative to the chemical energy conversion rate.

### Other parameters

It should be noted that additional parameters may be used to estimate the importance of other effects, such as radiative pressure and radiative energy density. While the contribution of these effects are generally small under most conditions studied in combustion, they should be considered under extreme circumstances, such as nuclear fusion processes or within the vacuum of space, and the reader should consult representative texts for further information in this context [35].

#### 2.1.5 Canonical solutions to the RTE

Several analytical solutions to the radiative transfer equation (RTE), described in Eq. 2.7, exist for simple configurations. These simple systems include radiative emission from an

optically thin volume, from a uniform emitting and absorbing sphere, and radiation within a one dimensional plane-parallel medium. Knowledge of the solutions of these simple systems is a prerequisite for the application of MCRT as emission from an optically thin volume is used to determine radiative emission from a computational cell and radiation in a plane-parallel medium is a convenient tool to verify a radiation solver.

### Radiation from an optically-thin, uniform volume

First, the radiative transfer equation (RTE), Eq. 2.15 is repeated for convenience,

$$\frac{dI_\eta}{ds} = \hat{\mathbf{s}} \cdot \nabla I_\eta = \kappa_\eta I_{b\eta} - \beta_\eta I_\eta + \frac{\sigma_{s\eta}}{4\pi} \int_{4\pi} I_\eta(\hat{\mathbf{s}}) \Phi_\eta(\hat{\mathbf{s}}_i, \hat{\mathbf{s}}) d\Omega_i . \quad (2.15)$$

The net radiation source term at a point may be determined by integrating across all solid angles, as

$$\int_{4\pi} \hat{\mathbf{s}} \cdot \nabla I_\eta d\Omega = \int_{4\pi} \kappa_\eta I_{b\eta} d\Omega - \int_{4\pi} \beta_\eta I_\eta d\Omega + \int_{4\pi} \frac{\sigma_{s\eta}}{4\pi} \left[ \int_{4\pi} I_\eta(\hat{\mathbf{s}}) \Phi_\eta(\hat{\mathbf{s}}_i, \hat{\mathbf{s}}) d\Omega_i \right] d\Omega , \quad (2.16)$$

$$\nabla \cdot \int_{4\pi} I_\eta \hat{\mathbf{s}} d\Omega = 4\pi \kappa_\eta I_{b\eta} - \int_{4\pi} \beta_\eta I_\eta d\Omega + \frac{\sigma_{s\eta}}{4\pi} \int_{4\pi} I_\eta(\hat{\mathbf{s}}) \left[ \int_{4\pi} \Phi_\eta(\hat{\mathbf{s}}_i, \hat{\mathbf{s}}) d\Omega_i \right] d\Omega , \quad (2.17)$$

$$\nabla \cdot \dot{\mathbf{q}}_\eta = 4\pi \kappa_\eta I_{b\eta} - \beta_\eta \int_{4\pi} I_\eta d\Omega + \sigma_{s\eta} \int_{4\pi} I_\eta(\hat{\mathbf{s}}) d\Omega , \quad (2.18)$$

where  $\int_{4\pi} \hat{\mathbf{s}} \cdot \nabla I_\eta d\Omega$  is replaced with  $\nabla \cdot \int_{4\pi} I_\eta \hat{\mathbf{s}} d\Omega$  knowing that spatial and directional coordinates are independent of one another. Additionally,  $\int_{4\pi} I_\eta \hat{\mathbf{s}} d\Omega$  is equivalent to  $\dot{\mathbf{q}}_\eta$  and the definition of the scattering phase function  $\Phi$  has been applied to replace  $\frac{1}{4\pi} \int_{4\pi} \Phi_\eta(\hat{\mathbf{s}}_i, \hat{\mathbf{s}}) d\Omega_i$  with 1. Applying the definition of extinction coefficient,  $\beta_\eta = \kappa_\eta + \sigma_{s\eta}$  then allows for simplification of the overall equation to

$$\nabla \cdot \dot{\mathbf{q}}_\eta = 4\pi \kappa_\eta I_{b\eta} - \kappa_\eta \int_{4\pi} I_\eta d\Omega . \quad (2.19)$$

This term represents the divergence of radiative heat flux and is equivalent to the negative of the radiation energy source term that is used when conducting coupled calculations of radiation with CFD. The first term on the right hand side of Eq. 2.19 represents the radiative

emission from a point, and the second term represents the radiative absorption at the point. When the *optically thin assumption* (OTA) (see section 2.1.4) is applied, the right hand side of Eq. 2.19 is reduced to just its first term, and all radiative absorption is ignored, as

$$(\nabla \cdot \dot{\mathbf{q}})_{OTA} = 4\pi\kappa_\eta I_{b\eta} \quad (2.20)$$

Using Eqs. 2.5, and Eq. 2.3, with the assumption of a refractive index of unity, the preceding equation can be integrated across the spectrum and simplified to

$$E_{emi} = 4\pi\kappa_p I_b = 4\kappa_p E_b = 4\kappa_p \sigma T^4 , \quad (2.21)$$

where  $T$  is the temperature at the point. When a small volume is assumed to be uniform and optically thin, the net emission from the volume can be evaluated as

$$E_{emi} = 4\kappa_p \sigma T^4 V, \quad (2.22)$$

where  $V$  is the volume of the emitting volume.

### Radiation in a uniform sphere

Another simple example of radiative heat transfer can be applied to a non-scattering, isothermal sphere that is surrounded by cold and black boundaries. The intensity traveling at a point within a sphere can be described as

$$I_\eta(\tau_R, \theta) = I_{b\eta} (1 - e^{-2\tau_R \cos \theta}) . \quad (2.23)$$

Where  $\tau_R$  is the radius weighted by absorption coefficient and  $\theta$  is the exit angle (angle between the exit direction and the negative norm of the sphere's surface). Then, the radiative heat flux at a point along the surface of the sphere can be evaluated by integration over all incident angles and wavenumbers, as

$$\mathbf{q} = \int_0^\infty \int_0^{2\pi} \int_0^\pi I_\eta(\tau_R, \theta) \cos \theta \sin \theta \, d\theta \, d\psi \, d\eta , \quad (2.24)$$

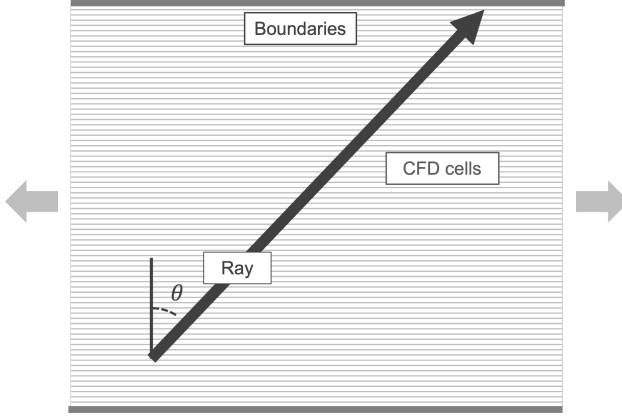


**Figure 2.2** Graphic of a plane parallel medium and a ray being traced.

$$\mathbf{q} = \int_0^\infty \int_0^{2\pi} \int_0^\pi I_{b\eta} (1 - e^{-2\tau_R \cos \theta}) \cos \theta \sin \theta \, d\theta \, d\psi \, d\eta , \text{ and} \quad (2.25)$$

$$\mathbf{q} = n^2 \sigma T^4 \left\{ 1 - \frac{1}{2\tau_R^2} [1 - (1 + 2\tau_R)e^{-2\tau_R}] \right\} . \quad (2.26)$$

Under the conditions of an optically-thin sphere, radiative re-absorption can be ignored, and the equation can be simplified to

$$\mathbf{q} = n^2 \sigma T^4 \frac{4}{3} \tau_R , \quad (2.27)$$

where the heat flux can be integrated across the surface area of the sphere to produce the net energy divergence from the optically thin sphere, as

$$Q_{emi} = 4\kappa n^2 \sigma T^4 V . \quad (2.28)$$

This equation is equivalent to 2.22 and can equally be used to evaluate the emission from an uniform, optically thin volume of arbitrary shape.

### Radiation in a plane-parallel medium

An analytical solution to the RTE can also be obtained for a one-dimensional radiatively participating medium surrounded by walls, as shown in Fig. 2.2.

The modified RTE, Eq. 2.8, is repeated below for convenience as

$$\frac{dI_\eta}{d\tau_\eta} = S(\tau_\eta, \hat{\mathbf{s}}) - I_\eta , \quad (2.29)$$

where  $d\tau_\eta$  has been substituted for  $\beta_\eta ds$ , as discussed in section 2.1.3. An integration factor  $e^{-\tau_\eta}$  may be multiplied through as

$$e^{\tau_\eta} \frac{dI_\eta}{d\tau_\eta} + e^{\tau_\eta} I_\eta = S(\tau_\eta, \hat{\mathbf{s}}) e^{\tau_\eta}, \quad (2.30)$$

$$\frac{dI_\eta e^{\tau_\eta}}{d\tau_\eta} = S(\tau_\eta, \hat{\mathbf{s}}) e^{\tau_\eta}. \quad (2.31)$$

After integration, this becomes,

$$I_\eta(\tau_\eta) = I_\eta(0)e^{-\tau_\eta} + \int_0^{\tau_\eta} S(\tau'_\eta, \hat{\mathbf{s}}) e^{-(\tau_\eta - \tau'_\eta)} d\tau'_\eta. \quad (2.32)$$

The source term  $S(\tau'_\eta, \hat{\mathbf{s}})$  is defined in Eq. 2.33,

$$S(\tau'_\eta, \hat{\mathbf{s}}) = (1 - \omega_\eta) I_{b\eta} + \frac{\omega_\eta}{4\pi} \int_{4\pi} I_\eta(\hat{\mathbf{s}}) \Phi_\eta(\hat{\mathbf{s}}_i, \hat{\mathbf{s}}) d\Omega_i, \quad (2.33)$$

where  $\omega_\eta$  is the single-scatter albedo,  $\omega_\eta = \sigma_\eta / (\sigma_\eta + \kappa_\eta)$ . The first and second components of the source term describe the emission of radiation along  $\hat{\mathbf{s}}$  and the in-scattering of radiation into direction  $\hat{\mathbf{s}}$ . Within a plane-parallel medium, properties only vary along the axis normal to the walls. Therefore, the coordinate  $\tau_\eta$  may be transformed to a wall-perpendicular coordinate as  $\tau_{p\eta} = \tau_\eta \cos \theta$ , where  $\theta$  is the angle between the ray direction and the perpendicular axis. Extending this transformation to Eq. 2.32 results in

$$I_\eta^+(\tau_{p\eta}, \theta) = I_{1\eta} e^{-\tau_{p\eta}/\cos \theta} + \int_0^{\tau_{p\eta}} S(\tau'_{p\eta}, \theta) e^{-(\tau_{p\eta} - \tau'_{p\eta})/\cos \theta} \frac{d\tau_{p\eta}}{\cos \theta}', \text{ and} \quad (2.34)$$

$$I_\eta^-(\tau_{p\eta}, \theta) = I_{2\eta} e^{-(\tau_{Lp\eta} - \tau_{p\eta})/\cos \theta} + \int_{\tau_{Lp\eta}}^{\tau_{p\eta}} S(\tau'_{p\eta}, \theta) e^{(\tau_{p\eta} - \tau'_{p\eta})/\cos \theta} \frac{d\tau_{p\eta}}{\cos \theta}'. \quad (2.35)$$

$I_\eta^+$  and  $I_\eta^-$  are spectral intensities propagating in the positive and negative  $\tau_p$  directions, respectively. Also,  $I_{1\eta}$  and  $I_{2\eta}$  are the emitted intensities from walls 1 and 2 at  $\tau_{p\eta} = 0$  and  $\tau_{p\eta} = \tau_{Lp\eta}$ , respectively. The split of Eq. 2.32 into Eqs. 2.34 and 2.35 is convenient by allowing the emission from each boundary to be individually accounted for. As a whole, Eq. 2.34 represents the emission of radiative intensity from below the point of interest  $\tau_{p\eta}$  (including the boundary at  $\tau_{p\eta} = 0$  with intensity  $I_{2\eta}$ ) up to the point of interest, and Eq. 2.35 represents the same but for above the point of interest.

With the solution for spectral radiative intensity obtained, the overall divergence of heat flux can also be evaluated by completely solving Eq. 2.19. The first term in Eq. 2.19 can be calculated using the provided parameters for  $\kappa_\eta$  and  $I_{b\eta}$ . The second term, which represents the absorption coefficient times irradiance  $G_\eta$  may be calculated as

$$G_\eta(\tau_{p\eta}) = \int_{4\pi} I_\eta d\Omega = \int_0^{2\pi} \int_0^\pi I_\eta(\tau_{p\eta}, \theta) \sin \theta d\theta d\psi , \quad (2.36)$$

$$G_\eta(\tau_{p\eta}) = 2\pi \int_{-1}^{+1} I(\tau_{p\eta}, \mu) d\mu \quad (2.37)$$

where  $\mu = \cos \theta$ . Splitting the intensity into positive and negative components results in

$$G_\eta(\tau) = 2\pi \left[ \int_{-1}^0 I^-(\tau_{p\eta}, \mu) d\mu + \int_0^{+1} I^+(\tau_{p\eta}, \mu) d\mu \right] \quad (2.38)$$

and substituting in the solutions for  $I_\eta^+$  and  $I_\eta^-$ , Eqs. 2.34 and 2.35, leads to

$$\begin{aligned} G_\eta(\tau) &= 2\pi \left[ I_{b1\eta} E_2(\tau_\eta) + I_{b2\eta} E_2(\tau_{Ln} - \tau_\eta) + \int_0^{\tau_\eta} S(\tau'_\eta) E_1(\tau_\eta - \tau'_\eta) d\tau'_\eta \right. \\ &\quad \left. + \int_{\tau_\eta}^{\tau_{Ln}} S(\tau'_\eta) E_1(\tau'_\eta - \tau_\eta) d\tau'_\eta \right] \end{aligned} \quad (2.39)$$

$$E_n(x) = \int_0^1 \mu^{n-2} e^{-x/\mu} d\mu \quad (2.40)$$

where  $I_{b1\eta}$  and  $I_{b2\eta}$  are the spectral black body intensities from the two boundaries, the subscript  $p$  has been removed, and  $E_n$  is the exponential integral defined in eq. 2.40.

Equation 2.39 can be computationally expensive to solve in a scattering medium because the scattering component of  $S(\tau'_\eta)$  is also a function of  $G_\eta(\tau_\eta)$ , rendering Eq. 2.39 implicit. One numerical approach is to provide an initial guess irradiance field  $G_\eta(\tau_\eta)$ , evaluate  $S(\tau'_\eta)$ , and integrate for another solution to  $G_\eta(\tau_\eta)$ . The process can be repeated until  $G_\eta(\tau_\eta)$  has converged. Such a solution procedure is computationally inexpensive in a medium with little to no scattering, but can become expensive under high scattering. Finally, provided a solution to  $G_\eta(\tau_\eta)$ , the spectral radiative absorption at every point may be evaluated as  $\kappa_\eta G_\eta(\tau_\eta)$ , and the overall volumetric radiation source term at any point can be evaluated as

$$Q_{src} = \int_0^\infty \kappa_\eta G_\eta d\eta - 4\kappa_p \sigma T^4. \quad (2.41)$$

### 2.1.6 Frozen-Field Analysis

The speed of light in a vacuum may be much higher than even the fastest processes within a combustion simulation. As such, the flow may be considered static during the traversal of a ray, and the solution of radiation for a timestep may be decoupled from the rest of the physics modeling. A *frozen-field analysis* is one approach used in many thermal radiation models. In frozen-field analysis, a single time-step of a Computational Fluid Dynamics (CFD) simulation is extracted, and a solution for the RTE is evaluated using a radiation model. This approach is convenient and less computationally expensive for testing a radiation solver because a full solution of radiation at every timestep from initial conditions is not required.

## 2.2 Influences of radiation in combustion

### 2.2.1 Coupling to fluid dynamics

There exists a strong coupling between radiation and fluid dynamics within many combustion systems. Redistribution of thermal energy results in changes to local thermodynamic states. This may lead to, for example, density changes that result in buoyant fluid motion. Furthermore, changes in fluid motion from the environment like wind may result in stymied combustion, which can lead to decreases in radiative emission [36].

A key area of study in radiating flames are wild-land fires. The large length scales and high degrees of emissive power from fires result in a significant, non-negligible influence of radiation within the flame and to the surroundings [37]. If surrounding objects are flammable, then radiation can ignite new flames at a distance resulting in increased fire spread and damage [4]. Extensive research has been conducted in determining the exact contribution of radiation in these flames [38] in order develop preventative methods to inhibit flame radiation such as water droplets [39]. Recent technological advances have seen improvements in modeling and diagnostic methods, resulting in more informed computa-

tional and experimental findings, but many fundamental questions on the contributions of radiation to the flame and fluid dynamics remain to be answered [40]. Broadly speaking, it is known the coupling of radiation to momentum fields largely take place over long length and time scales [41]. Turbulent puffing motions and toroidal vortices resulting from buoyant and baroclinic forces [42] may result in changes in soot production [43]. Soot is often a primary radiator from many hydrocarbon flames, amounting to 25 to 35% energy escaping [41]. However, high concentrations of soot surrounding a large flame may also block radiation to the surroundings [44]. Evidence largely supports that larger fires have more significant contribution of radiation [43]. However, Hiroshi and Taro [45] experimentally tested flames ranging from 0.3 and 6 meters in diameter and determined the soot radiation blocking effect appeared in sizes 2 meters and above.

Pool-fires are also a common fire scenario that occurs in chemical process industries [46] and can be used as a surrogate to for many other kinds of real fires [43]. A pool fire is a canonical configuration where a liquid pool of fuel is vaporized, ignited, and reacts with surrounding oxidizer. Much research has been conducted using this configuration to determine the influence of turbulent fluid motion, wind, and flow structures on radiative heat flux and vice versa [43]. For example, Hu [36] discussed the influences of flame tilt to the view-angle of a flame to a boundary. When a powerful gust of wind tilts the flame, less of the flame is visible to an adjacent object, resulting in reduced radiation. This effect results in a decrease of the incident heat flux, and therefore vaporization rate, of the pool, and can therefore limit the fuel supply and have a concomitant influence on all characteristics of the flame.

In general, radiation is a ‘dissipative process’. As a result, redistribution of thermal energy may lead to a reduction in local turbulence intensity [5]. Li [47] studied the influence of radiation in scaled flames and determined increasing radiation resulted in considerable decreases in temperature fluctuation. Wang et al. [48] calculated radiation reductions of 5% in their artificially scaled Sandia D flames. Consalvi [49] presented reductions approaching

10% in simulations with radiation compared to those without. In all, the exact influences of radiation on turbulence are masked due to computational expense and lack of adequate turbulence/radiation interaction (TRI) modeling to accounting for the non-linear influence of unresolved turbulent fluctuations in LES and RANS simulations [5].

### 2.2.2 Radiation in enclosed engines

Relatively few studies have focused specifically on the contribution of radiative heat transfer to the boundaries of enclosed combustion engine systems. Most existing models involve low-fidelity gray models combined with inaccurate radiation solvers, such as P-1. A brief review of existing research of radiation to the boundaries of gas-turbine engines and rocket engines is first provided, followed by a review of radiation modeling within surrounding protective thermal barrier coatings.

#### Radiation incident on the boundaries

Modern gas-turbine combustors operate at temperatures that far exceed the material limits of the enclosing materials [50]. These extreme conditions pose a risk of harmful wear and damage to the combustion chamber or downstream turbine stages. Advanced cooling techniques are employed such as film cooling to mitigate the damaging and potentially dangerous effects of these conditions [51]. However, excessive cooling for material protection may present a significant thermodynamic loss to the system, reducing the overall work contribution from the energy conversion process. As a result, an understanding of the influence of all modes of heat transfer along the boundaries has seen increased importance.

Lefebvre [52] provided an early review on radiation in gas-turbine chambers. Radiative emission is known to contribute significantly to wall heat flux, in particular for high pressure and highly luminous flames. Also, the challenge of predicting radiative emission and absorption rates while accounting for soot formation, non-gray modeling, and other variables were

described. Claus [53] conducted an experimental study of radiation from a Pratt & Whitney JT8D tubular can combustor and found that soot contributed 70–80% of radiative emission in the primary zone, 50–70% in the intermediate zone, and 35–50% in the dilution zone. Berger et al. [8] conducted transient simulations of a helicopter engine combustor to compare the influences of conjugate convection and radiation on the system boundaries. They applied the Discrete Ordinates Method (DOM), a relatively low-cost radiation model with high accuracy, combined with a statistical narrow-band non-gray model accounting for CO<sub>2</sub>, CO, and H<sub>2</sub>O, and a large-eddy simulation with the thickened-flame approach for chemistry modeling. Their results showed convection and radiation contributed similar orders of magnitude to wall heat fluxes, with radiation primarily contributing heat to the colder-wall regions and reducing flame temperatures. Radiative energy was shown to contribute a negligible difference to the thermodynamics of the flame, contributing two orders of magnitude less energy than the chemical heat release. Finally, good agreement was obtained to experimental results. Paul and Jones [54] applied the DOM to a CFD simulation of the Rolls Royce Tay gas turbine geometry. Soot and non-gray absorption were neglected. Emission was shown to maximize in regions where temperature is maximized. However, the authors noted the contribution of soot may effect these results. Gamil et al. [13] compared the contribution of radiation in a Rolls-Royce RB-183 turbofan engine combustor using the DOM and the P-1 approximation, another radiation model. The influences of soot and non-gray absorption were again neglected. The combustor geometry follows a Rich-Quenched-Lean (RQL) design, where a high temperature, non-premixed flame is followed by a high degree of mixing with dilution gases, which is followed by a premixed fuel-lean reaction to the aft section of the combustor. Apparently, radiation resulted in a 10% higher temperature in the liner near the fuel-rich zone, and a 15% reduction of temperature after the dilution zone. In total, radiation was shown to reduce peak flame temperatures by 200K compared to with no radiation for their transient simulation. The P-1 model was shown to over-exaggerate the effect of radiation compared to the more accurate DOM. Ghose et al. [55] conducted similar

transient simulations of a mock gas-turbine combustor using the DOM radiation method with a weighted-sum of gray gases non-gray model and an empirical correlation for soot. They observed that radiation exhibited significant control over the incident heat flux to the injector and combustor walls, and soot played a significant role in emission. They also observed a strong dependence of radiation on the geometry: where increasing injector swirl resulted in an axially tightened flame with lower peak radiative heat flux to the walls.

Radiation has also been shown to contribute significantly in rocket engines. Between 5% and 30% of the overall heat flux at the walls can be attributed to emission from the medium [56, 57, 58]. Leccese et al. [59] evaluated the influence of radiation and convection using a RANS CFD model with gray-gas radiation. They observed radiation contributions totaling to 15% and 11% for liquid methane/liquid oxygen and liquid hydrogen/liquid oxygen, respectively. Leccese et al. [60] later studied the influences of radiation in a Space Shuttle Main Engine (SSME) in a transient simulation, but with no radiative contribution to the energy equation. They observed peak wall-incident radiative heat flux follows where peak temperatures occur, within the combustion chamber rather than the throat or nozzle. They also developed a resource to gather predictions of wall heat transfer coefficients and fractional contributions of radiation as a function of chamber pressure and diameter for both liquid methane/liquid oxygen and liquid hydrogen/liquid oxygen. Radiative contribution was shown to increase with a decrease in pressure and an increase in chamber diameter.

Additional studies have shown that radiation plays a very significant role in the wall heat fluxes in heavy-duty diesel pistons, re-entry vehicles, and many combustion technologies of recent interest such as oxy-fuel combustion [5, 61].

## Thermal Barrier Coatings

In many systems, the high temperatures associated with combustion may exceed the melting points of the materials of the outer casing [62]. This can potentially be a limiting factor to consider during the design of these systems, such as in a gas-turbine combustor. A

Thermal Barrier Coating (TBC) is a protective material often applied to the interior walls of combustion systems to manage the heat loads to the outer surfaces. TBCs are usually constructed from a specialized Zirconia ceramic, which has the capability to resist heat better than most materials [63]. Specifically, Yttria-stabilized zirconia (YSZ) provides adequate performance for modern TBCs [50, 64]. At high temperatures, these materials become more transparent to thermal radiation, and the resulting heat transfer analysis becomes more complex [19, 65]. The introduction of gas-filled pores also induces ray scattering, which has been shown to reduce metal temperatures [66, 67], but further complicates the understanding of the system.

Analysis between the flame, TBC, metal, and cooling impingement flow includes all three forms of heat transfer: conduction, convection and radiation. Conjugate modeling of the three forms can be computationally intensive, especially when using exact methods [30]. The inclusion of radiative heat transfer within the conjugate heat transfer model makes a solution analytically intractable when complex material properties and boundary conditions are involved. As a result, appropriate modeling of TBCs is rare in high temperature systems. A fully comprehensive, one dimensional, analytical method was presented by Siegel [68]. Through the use of the Milne-Eddington approximation for radiation, the method can solve conduction and radiation simultaneously within the semitransparent TBC [69, 70]. The TBC is assumed to have a cutoff wavelength,  $\lambda_c$  where all incident radiation of wavelength below  $\lambda_c$  passes through the TBC surface and is solved according to the RTE. All remaining incident radiation is absorbed at the surface and modeled within the TBC as conductive diffusion [71]. The combined heat transfer solution for the TBC was established to be very accurate in most circumstances and not very computationally expensive according to Siegel [68]. However, assumptions such as gray gases, one-dimensionality, and two flux can limit the applicability of Siegel's method. Johnson and Zhao [9] coupled the Siegel's method with a Monte Carlo ray tracing analysis of a gas turbine combustor, where non-gray radiation from the flame is accounted for. Differences in temperature as large as 150 K were observed within

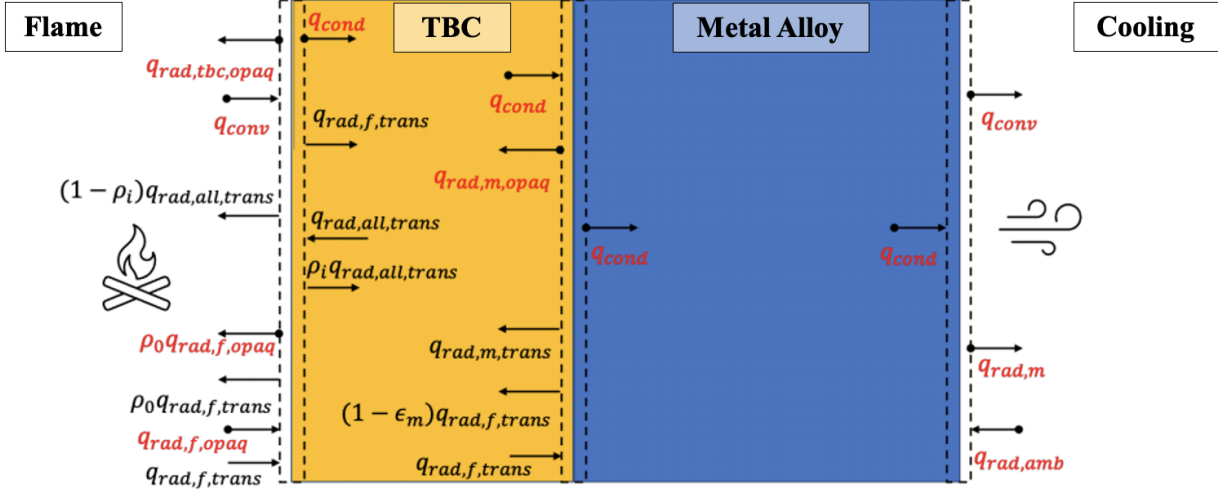


**Figure 2.3** The computational domain for the conjugate heat transfer solver from [2]. Various sources of heat transfer rate are labeled, with the red-fonted heat transfer rates accounted for by the conduction solver and the black-fonted heat transfer rates accounted for by the radiation solver. The yellow domain and blue domains are the TBC and metal, respectively. The x direction follows from the flame to the impingement flow. The y and z directions are vertical and into the page, respectively.

the TBC between non-gray and gray analyses. Finally, Tricard and Zhao [2] generated a 3-D model of conjugate heat transfer in a semitransparent TBC at steady state using MCRT radiation coupled with Finite-Volume Method (FVM) conduction. The simulation followed that of Siegel [68], where a cutoff wavelength was assumed. Results were comparable to Siegel's method, and three dimensional influences were shown to be influential to the steady-state temperature distribution in the domain. Additionally, a parametric study concluded that increasing  $\lambda_c$  results in a decrease in peak temperature and a trend of decreasing heat flux through the TBC as a result of increased net reflectance of heat.

### 2.2.3 Changes to chemistry

The physics of combustion processes are often highly dependent on the accompanying chemical reaction network. The multitude of reactions that proceed during the conversion from the reactant molecules to the product species in combination with changes to the existing

macroscopic thermodynamic properties results in a complex modeling procedure. For one, radiation has been shown to influence the temperature of a system. Temperature has a high degree of control on the chemical reaction rates of combustion. This presents an additional, indirect influence of radiation on the hydrodynamic process, one that requires coupled modeling of thermal, fluid, and chemical processes within a combustion simulation for an adequate analysis.

## Flammability

Characterizing the extinction limits of a flame is a useful measure for many applications. Radiation has been a known contributor to the lean flammability limits of many flames [7, 72]. Many one-dimensional simulations and experiments have been performed for the purpose of investigating this phenomenon. Lakshmisha et al. [73] simulated one-dimensional CH<sub>4</sub>/air flames with the OTA radiation model near lean flammability limits. They demonstrated that radiant heat loss is the primary cause of flame extinction when the lean flammability limit is approached. Ju et al. [74] investigated the influence of radiation absorption within a premixed flame. They determined that accounting for radiation re-absorption can lead to wider extinction limits and higher burning velocities. Further, the optically thin assumption leads to significant decreases in product species temperatures, while absorption will retain product temperatures and additionally allow for pre-heating of the reactants. Additionally, through the use of a statistical narrow-band model, the influences of non-gray emission patterns lead to a significant escape of radiation through the reactant zone. They observed the difference in the emission spectrum from high temperature CO<sub>2</sub> and absorption spectrum of the low temperature CO<sub>2</sub> supplied along with reactants can lead to a significant escape of energy upstream of the flame. And they observed a similar trend for H<sub>2</sub>O, where no H<sub>2</sub>O was readily available in the reactants for absorption.

## Pollutant formation

As discussed previously, radiation carries a strong influence on the temperature of combustion systems. And because temperature and chemistry are coupled, radiation also influences the product species concentrations at the exit of many combustion systems. In particular, the production of pollutant species  $\text{NO}_x$  (nitrous oxides) and soot can be significantly affected [75]. Medwell et al. [76] experimentally measured the influence of radiation in a laminar ethylene flame irradiated by a  $\text{CO}_2$  laser. High incident radiation was shown to increase peak soot volume fraction by 250%, suggesting there exists a strong correlation of soot production with radiation. Ihme and Pitsch [10] demonstrated the influence of radiation on  $\text{NO}_x$  production by including an additional dimension to the flamelet progress variable approach for chemistry tabulation. They applied the optically thin assumption (OTA) to simulations of the Sandia D. flame and the Pratt & Whitney PW6000 combustor. For both cases, production of nitric oxide was reduced by more than 60% compared to simulations without radiation included as a result of the lower peak temperatures. Ren et al. [12] calculated the change in  $\text{NO}_x$  output resulting from radiative emission within a gas-turbine combustion chamber. They determined that radiation modeled with line-by-line Monte Carlo enhanced re-absorption in the flame and enhanced NOx emissions by almost 20% compared to combustors modeled without radiation.

# Chapter Three

## Monte Carlo Ray Tracing

As explained in Chapter 2, thermal radiation can play a significant role in the physics of a combustion system. Consequently, comprehensive simulations of combustion phenomena should include modeling of thermal radiation to some degree. When a medium is at a high temperature and is not optically thin, both the emission and absorption of radiation must be accounted for at all points in the domain. As a result, the modeling of radiation may be difficult and expensive. Furthermore, multiphysics simulations include a number of other processes, from detailed chemistry to compressible fluid dynamics. As a result, the available computational time and resources that can be devoted to modeling radiation is sometimes limited.

Several radiation models exist that promise accurate solutions to the RTE at minimal expense. Two of the most common methods are the method of spherical harmonics (e.g., P-1, P-3) and the discrete ordinates method (DOM). These methods offer a trade-off between accuracy and efficiency. The P-1 method is considered fast, but may be inaccurate. The DOM is more accurate, but requires significant computing time. However, both of these methods are limited in that when they are supplied infinite computational resources, they do not provide exact solutions to the RTE. Alternatively, the Monte Carlo Ray Tracing method does offer this advantage [59], and while many consider Monte Carlo ray tracing to be more computationally intensive, recent studies have shown that by using parallel processing,

MCRT can consume even less runtime than its less accurate counterpart, DOM [77]. With this potential in mind, MCRT is chosen for the present implementation, as it offers the highest accuracy and greatest potential for growth as computational power and parallel processing capabilities increase [7, 19].

This chapter first reviews the present implementation of MCRT. Then, a description of methods of MCRT acceleration through mathematical reformulations will be presented. Finally, a detailed account of the implementation for this research will be discussed.

### 3.1 Forward Monte Carlo Ray Tracing

The Monte Carlo method has long been an accurate method to numerically integrate many equations [22]. Solving the RTE, Eq. 2.7, is one application of this method. The fundamental principle behind the Monte Carlo Ray Tracing (MCRT) method is that the redistribution of thermal energy through radiation can be modeled using a series of random rays. Each computational cell that has a quantity of energy that should be emitted (defined by Eq. 2.22) will delegate the task of redistributing that energy among a number of rays emitted from within the cell’s volume. The rays are first initialized using a set of random numbers to define their points of emission, directions, and wave-numbers (inverse wavelengths). Then, each bundle of energy is ‘traced’. In combustion CFD, this tracing process usually involves the computation of an absorption coefficient  $\kappa_\eta$  and an intersection length  $\Delta s$  between a ray and every cell it intersects. The energy deposition process can either occur gradually (where the ray’s energy gradually decays as it deposits energy into each passing cell, also known as the *energy partitioning method*), or the ray may deposit all of its energy into a cell defined using random numbers [78]. The tracing ends once the rays escape from the domain or have been absorbed entirely.

The MCRT method is highly robust. For one, the raytracing process can be completed in arbitrary domains with cells of arbitrary shape. Furthermore, the similarity between

simulation ‘rays’ and electromagnetic rays not only provides an intuitive understanding of MCRT, but also enables MCRT to model similar physics undergone by real photons. This includes, for example, anisotropic scattering events, specular ray reflections, or changes of refractive index within the medium [78]. Moreover, the selection of different ray wavenumbers allows MCRT to easily adapt to a non-gray implementation. Whereas P-1 and DOM must be solved multiple times for select wavelength bands to obtain a non-gray solution, which can be prohibitively expensive when used with a line-by-line model, MCRT instead needs to only be solved once with varying ray wavenumbers.

### 3.1.1 Random number selection process

In order to ensure a physically realistic solution to the RTE, care must be taken to ensure the predicted distribution of ray attributes matches the expected distribution seen in nature. A *random number relation* is the process used to convert a supplied distribution of random numbers (usually uniform between zero and one) to the actual distribution of a randomized ray’s characteristics (e.g. wavenumber, direction). Random number relations are important to not only obtain accurate solutions, but also maximize the efficiency of the code.

For example, in order to define a ray’s direction of propagation from a face, values for the ray’s polar angle  $\theta$  and azimuthal angle  $\psi$  of propagation must be defined, as shown in Fig. 3.1. The Monte Carlo method dictates that these directions must be decided using random numbers. A naive and inefficient implementation would be to directly select ray emission directions uniformly across the polar and azimuthal angles, as  $\theta = R_\theta\pi/2$ , and  $\psi = 2\pi R_\psi$ , where  $R_\theta$  and  $R_\psi$  are random numbers between zero and one. Calculating the ray’s polar direction in this way would result in a significantly greater ray emission per unit solid angle at the low polar angles than the high polar angles. In other words, ray emission would not be uniform across the hemisphere. Obtaining a physically correct, isotropic solution with this naive method would require the rays’ energies to vary as a function of their polar

angular direction, which adds significantly to the computational runtime.

Alternatively, a more efficient random number selection process employs *importance sampling*. By assigning each ray an equal amount of energy, the attribute selection process can proceed with the knowledge that each ray carries an equal contribution to the overall energy distributed from a cell. This means the energy profile of each attribute also defines the probability distribution of random selection of that attribute. In practice, this requires a transformation from the uniform random number distribution  $R$ , between zero and one, to the non-uniform energy distribution. The subsequent sections define the random number relations used to employ importance sampling in this study and follow descriptions from Modest and Mazumder [78].

### Point of emission

The random number relation for the  $x$  coordinate of emission within a three-dimensional volume is

$$R_x = \int_0^x \int_0^Y \int_0^Z \kappa_p \sigma T^4 \, dz \, dy \, dx \Big/ \int_0^X \int_0^Y \int_0^Z \kappa_p \sigma T^4 \, dz \, dy \, dx , \quad (3.1)$$

where  $R_x$  is a uniformly distributed random number, and  $X$ ,  $Y$ , and  $Z$  are functional representations of the respective coordinate bounds of the volume. Similarly, the  $y$  point of emission and  $z$  point of emission may be calculated as

$$R_y = \int_0^y \int_0^Z \kappa_p \sigma T^4 \, dz \, dy \Big/ \int_0^Y \int_0^Z \kappa_p \sigma T^4 \, dz \, dy \text{ and} \quad (3.2)$$

$$R_z = \int_0^z \kappa_p \sigma T^4 \, dz \Big/ \int_0^Z \kappa_p \sigma T^4 \, dz . \quad (3.3)$$

These equations must be inverted for an explicit solution for  $x$ ,  $y$ , and  $z$  [78]. Solving multi-variate integrals during the solution procedure would be extremely computationally expensive. Fortunately, many MCRT applications apply these random number relations to a computational cell, where the emission term (the integrand) can be assumed spatially constant. Assuming the cell exists in a cartesian, axes-aligned grid with  $X$ ,  $Y$ , and  $Z$  cell

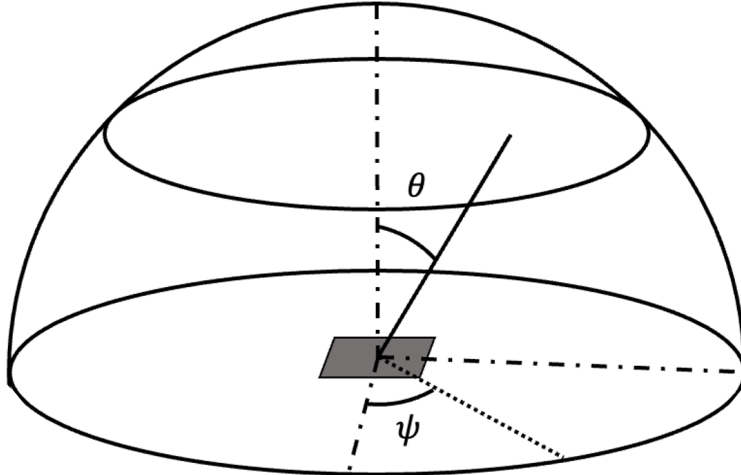


**Figure 3.1** Angle definitions for ray direction from a boundary.  $\theta$  is the polar angle and ranges from 0 to  $\pi/2$ .  $\psi$  is the azimuthal angle and ranges from 0 to  $2\pi$ . When a ray is emitted from a point in a medium, a ray may be emitted in any direction across the unit-sphere, and  $\theta$  will range from 0 to  $\pi$ .

dimensions equal to  $\Delta X$ ,  $\Delta Y$ , and  $\Delta Z$ , the random-number relation can then be simplified to

$$x = R_x \Delta X; \quad y = R_y \Delta Y; \quad z = R_z \Delta Z . \quad (3.4)$$

Therefore, the point of emission is simply a random point within a 3-D rectangular prism. For an unstructured solver such as in `OpenFOAM`, the point of emission within an arbitrarily shaped polyhedron must be defined. Due to a lack of generalized formulation for a random point in an arbitrary shaped polyhedron, the center-point of the cell is used to define the emission point in this research.

### Direction of emission

The direction of emission for a ray can be evaluated using the polar and azimuthal angle along the unit sphere, defined in Fig. 3.1. Local thermodynamic equilibrium guarantees isotropic emission; therefore, the directions can be calculated as

$$\psi = 2\pi R_\psi \text{ and} \quad (3.5)$$

$$\theta = \arccos(1 - 2R_\theta) . \quad (3.6)$$

Note the non-linear dependence of polar direction on the uniformly distributed random variable, unlike the naive approach defined previously.

## Absorption

The spectral absorptivity  $\alpha_\eta$  of ray in a non-scattering medium follows as one minus Beer's law, as

$$\alpha_\eta = 1 - \exp\left(-\int_0^t \kappa_\eta \, ds\right), \quad (3.7)$$

where  $t$  is the distance the ray has traveled. The random number relation for the absorption location of the ray can be defined as

$$R_{abs} = \exp\left(-\int_0^t \kappa_\eta \, ds\right) \quad (3.8)$$

which may be reformulated for ray traversal through a series of  $N$  discrete sub-volumes, where complete ray absorption will occur at  $N$ th intersected cell as

$$R_{abs} = \exp\left(-\sum_{i=1}^N \kappa_i \Delta s_i\right), \text{ or} \quad (3.9)$$

$$\sum_{i=1}^N \kappa_i \Delta s_i = \ln \frac{1}{R_{abs}}, \quad (3.10)$$

where  $\Delta s_i$  is the distance travelled through cell  $i$ .

As mentioned in section 2.1.3, the absorption coefficient may vary unpredictably along its path length. As a result, the change of a ray's intensity requires knowledge of the ray's current intensity (i.e. requires some knowledge of the ray's *history* during traversal). Therefore, with the exception of the null-collision method (see section 3.2.2), a ray must be traced through the mesh sequentially in order to accurately determine the deposited energies. In other words, the summation term in Eq. 3.10 is incrementally evaluated from its emission point until the addition of the  $N$ th cell has exceeded the right hand side, at which point cell  $N$  will absorb the ray in its entirety.

Alternatively, the absorption process can also be modeled using the energy partitioning approach where Eq. 3.7 is used directly in discrete form to define the gradual depletion

of ray intensity. In forward MCRT, each cell that a ray intersects will receive an energy defined by the difference of ray energy at the entrance and exit of the cell. Then, the ray's propagation will continue until its energy has depleted below a threshold value. The energy partitioning approach is known to be more efficient in an optically thin medium where the rays will propagate far in the domain before complete absorption [7, 18], and is employed in this research.

## Wavelength

The random number relation for the wavelength can be described as

$$R_\eta = \frac{\pi}{\kappa_p \sigma T^4} \int_0^\eta \kappa_\eta I_{b\eta} d\eta . \quad (3.11)$$

For most mixtures in combustion modeling, the radiative emission spectrum varies significantly as a function of wavelength due to the highly intermittent modes of oscillation within the gas particles (see section 2.1.2). Therefore, the inversion process of Eq. 3.11 is complex. Adaption of the most accurate non-gray model in radiation, the line-by-line model, to MCRT requires a spectroscopic database such as HITEMP [32] to integrate Eq. 3.11.

In this research, the inversion of Eq. 3.11 follows the multi-step procedure defined by Ren and Modest [1]. This procedure exploits the additive nature of radiative emission, where the net volumetric radiative emission per unit solid angle  $E_{tot}$  can be determined by summing the contribution of each emitting species, as

$$E_{tot} = \sum_{i=1}^{n_s} \int_0^\infty \kappa_{\eta i} I_{b\eta} d\eta , \quad (3.12)$$

for  $n_s$  emitting species. The inversion of Eq. 3.11 may then proceed by first determining the emitting species  $s$  according to

$$s = j \quad \text{if} \quad \frac{\sum_{i=1}^{j-1} E_i}{\sum_{i=1}^{n_s} E_i} < R_\eta \leq \frac{\sum_{i=1}^j E_i}{\sum_{i=1}^{n_s} E_i} , \quad (3.13)$$

rescaling the random number as

$$R_{\eta s} = \frac{R_\eta E_{tot} - \sum_{i=1}^{j-1} E_i}{E_j}, \quad (3.14)$$

and evaluating the emitting wavenumber by inverting the emission spectrum for just the emitting species,

$$R_{\eta s} = \frac{\pi}{\kappa_{ps}\sigma T^4} \int_0^\eta \kappa_{\eta s} I_{b\eta} d\eta. \quad (3.15)$$

This approach is not only more efficient, but also allows for an explicit determination of the chemical species that emits a ray.

To invert Eq. 3.15, the approach used in this research is to create a table of wave-numbers and their corresponding integrated emissive powers  $E_{partial}$ ,

$$E_{partial} = \int_0^\eta \kappa_{\eta s} I_{b\eta} d\eta. \quad (3.16)$$

The table is created by incrementally increasing the  $\eta$ , calculating the integrated emissive power, and tabulating the data. As  $\eta$  approaches wavenumbers of order  $15000 \text{ cm}^{-1}$ , the integral approaches the total emissive power of  $\kappa_{ps} I_b$ , and the integration is concluded. Prediction of wavenumber given an emitting species is then determined by multiplying the species-specific random number  $R_{s\eta}$  by the total emissive power extracted from the last index in the table, and finding the wavenumber that corresponds to that partial emissive power.

### 3.1.2 Raytracing

The conventional MCRT methods rely on a raytracing procedure to determine the optical distances a ray propagates through in each cell, as shown in Fig. 3.2. The ray energy modeled using Eq. 3.7 requires knowledge of the order of cell intersection, as well as the distance travelled through each cell,  $\Delta s$ . While many structured meshes can evaluate tracing procedures using a fast pre-computing approach [79], unstructured meshes, like those used in OpenFOAM, require tracing through one cell at a time to determine the sequence of cells

intersected. Therefore, the traditional approach to raytracing is to incrementally trace the ray through the mesh, one cell at a time in order of intersection, using the exit faces of one cell to determine the next cell that is intersected.

Algorithm 1 defines a traditional forward Monte Carlo approach to MCRT. First, each cell is given an allotment of rays that are responsible for redistributing the radiative emissive power of that cell, defined by variable *emitting\_cell.rays*, and each ray is initialized using the random number relations from section 3.1.1. The number of rays emitted can either be a uniform value ranging from 1 to 1000, or defined using the emissive power of that cell as in the adaptive emission approach, see section 3.2.1. Then, each ray is traced through the mesh while its energy is greater than a certain minimum threshold. Each iteration of the while loop starts with the trigonometric calculation to determine the distance propagated through the cell  $\Delta s$ . Then, the spectral absorption coefficient  $\kappa_\eta$  for the ray is determined given the thermodynamic state of the cell (pressure, temperature and chemical species composition) as well as the ray’s wave-number  $\eta$ . Provided this information, the spectral optical distance traversed within the cell  $\tau_\eta$  is calculated, and the ray’s energy is depleted in accordance with Beer’s law, as on line 11. The depleted energy from the ray is deposited into the *cell.E* to model radiative absorption. Finally, the exit face of the current cell is used to determine the next cell intersected for the next iteration of the while loop.

The procedure requires calculations between every ray (up to tens of millions) and every cell that each ray intersects (up to several thousands). Due to the exceedingly high number of ray-cell interactions that must be computed, raytracing is often responsible for the bulk of the runtime consumed by the MCRT method [80] (see Fig. 1.1). As such, particular attention is dedicated to ensuring these calculations are as efficient as possible in the present MCRT code.

---

**Algorithm 1** Pseudocode for the traditional ray tracing process through a mesh. No ray-boundary interactions, ray scattering, or parallel processing is accounted for.

---

```
1: procedure RAYTRACING(mesh)
2:   for emitting_cell  $\in$  mesh do
3:     for ray  $\in$  emitting_cell.rays do
4:       RAY.INITIALIZE( )            $\triangleright$  point of emission, direction, wavelength
5:       cell  $\leftarrow$  emitting_cell
6:       while ray.energy  $>$  energy_minimum do
7:          $\Delta s \leftarrow$  RAY.GET_INTSEC_LENGTH(cell)
8:          $\kappa_\eta \leftarrow$  CELL.GET_ABSORPTION_COEFF(ray.wavenumber)
9:          $\tau_\eta \leftarrow \Delta s \times \kappa_\eta$             $\triangleright$  optical distance
10:         $E_{temp} \leftarrow ray.E$ 
11:        ray.E  $\leftarrow ray.E * \exp(-\tau_\eta)$ 
12:        cell.E  $\leftarrow cell.E + (E_{temp} - ray.E)$ 
13:        cell  $\leftarrow$  RAY.GET_NEXT_CELL()
14:      end while
15:    end for
16:  end for
17: end procedure
```

---

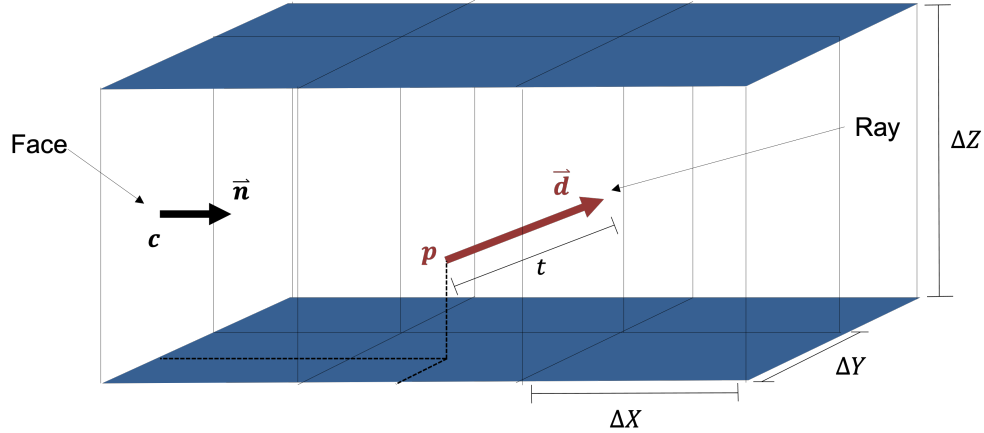


**Figure 3.2** Visual depiction of a ray traveling through a mesh.

### Trigonometric Calculations

Determining the distance travelled within a cell,  $\Delta s$ , requires calculations involving the ray and each of the faces of the cell [81]. The calculation proceeds as follows. Upon initialization, the ray is located within its originating cell. Within an arbitrarily shaped polyhedral cell, the exit face of the ray can only be determined by iterating through each face. While iterating through each face, the ray's intersection point along the face's plane is first calculated, then it is determined if the exit point lies within the boundaries of the face.

To evaluate the distance before intersecting the face, the following procedure is employed. The point of a ray  $\mathbf{r}$  with direction  $\vec{d}$  and origin  $\mathbf{p}$  after propagating a distance of  $t$  along its path length can be calculated as

$$\mathbf{r} = \vec{d}t + \mathbf{p} . \quad (3.17)$$

Meanwhile, the equation of a plane with a normal vector  $\vec{n}$  (which faces the exterior of the cell) and center-point  $\mathbf{c}$  can be represented as

$$\vec{n} \cdot (\mathbf{r} - \mathbf{c}) = 0 . \quad (3.18)$$

Substituting Eq. 3.17 into Eq. 3.18 creates the expression for the distance the ray travels before intersecting the plane  $t_{int}$ ,

$$t_{int} = \frac{d - \vec{n} \cdot \mathbf{p}}{\vec{n} \cdot \vec{d}} , \quad (3.19)$$

where  $d = \vec{n} \cdot \mathbf{c}$ , and can be pre-computed before the ray tracing procedure begins [82]. The calculation of  $t_{int}$  is conducted with each face of the cell to determine the exit face. When the dot product of a ray's direction with the face norm  $\vec{n} \cdot \vec{d}$  is negative, it is known that the face cannot be the exit location of that ray and the face should be skipped. If the dot product is positive, the point of intersection of the ray is then calculated using Eq. 3.17.

Next, it is confirmed whether the ray's exit point exists within the bounds of the face. For this, Sunday's winding number algorithm is applied [83]. This algorithm determines whether a point falls within a two-dimensional polygon of arbitrary shape. The algorithm can be extended for use in three dimensions by ignoring the normal vector coordinate of highest magnitude, and applying the point-in-face test using the other two coordinates.

Finally, assuming the cells are contiguous in space, the exit face of the cell is used to determine the entrance face of the following cell using conveniently defined mesh arrays. The procedure then repeats as discussed in the previous section until the ray has depleted sufficiently (falls below *energy\_minimum* on line 6), or until a boundary has been intersected.

## Boundary Interactions

Three types of boundary conditions are considered in the solver: wall, symmetry and processor boundary. Processor boundaries are applied when the boundary represents the interface with the computational cells situated on another computing process, or MPI rank. When a ray intersects this type of boundary, it is later communicated to the rank for continued tracing. For wall interaction, two models are commonly implemented in MCRT: black boundaries and gray boundaries. A black surface is one that absorbs all incident radiation and emits according to Planck's law, Eq. 2.1 in section 2.1.1. This type of boundary could be used to represent a combustor boundary or an opening to the surroundings (by assigning the boundary a constant, cold temperature). When a ray intersects a black boundary it is absorbed fully. Emission from a black surface is diffuse, and therefore directions of emissions

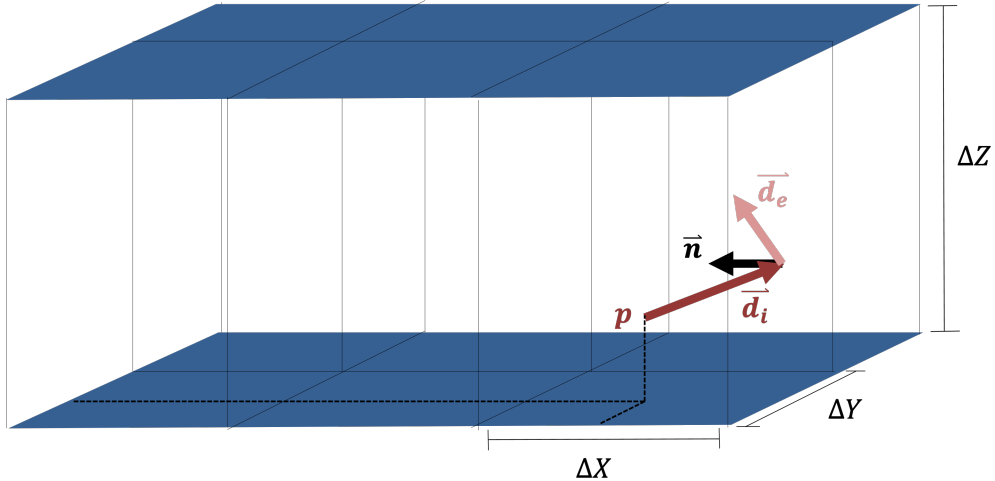


**Figure 3.3** Visual depiction of a specular ray reflection.

are defined by the random number relations for a diffuse, emitting surface, as

$$\psi = 2\pi R_\psi, \text{ and} \quad (3.20)$$

$$\theta = \arcsin \sqrt{R_\theta} . \quad (3.21)$$

A gray boundary has a more complex interaction with the environment. Gray surfaces can absorb, transmit, and reflect incident radiation. Gray surfaces also have only a fraction of the emission as that of a black body. The transmissivity  $\tau$  quantifies the fraction of incident radiation that passes through the surface, the absorptivity  $\alpha$  is defined as the fraction of incident radiation that is absorbed, and the reflectivity  $\rho$  is the fraction that is reflected. These definitions can be re-stated for a non-ideal, rough surface by replacing the -ivity suffix with -ance. Finally, from the emission perspective, the emissivity  $\epsilon$  is the ratio of boundary's emissive power to that of a black body. Kirchoff's law (see section 2.1.1) indicates that  $\epsilon = \alpha$  under the conditions of radiative equilibrium. For opaque and gray surfaces, the reflectivity can be determined by the relation  $\rho = 1 - \epsilon$ , where knowledge of the emissivity is sufficient to determine a boundary's reflectivity because  $\tau = 0$ .

Reflecting boundaries redirect incident rays from a wall-incident direction to a wall-exiting direction. The exit direction can be evaluated using either a *diffuse* or *specular*

model. A diffuse reflection occurs when an incident ray is deflected back in a random direction into the medium. This is accurate for surfaces with a high degree of variability of surface norms (rough surfaces), and the exit direction can be evaluated using Eqs. 3.20 and 3.21. A specular reflection is one that occurs from a smooth material, and can be visualized as Fig. 3.3. An example would be a mirror or the smooth surface of water. Under these conditions, the wall-exit direction can be calculated as

$$\vec{d}_e = 2(\vec{n} \cdot \vec{d}_i)\vec{n} - \vec{d}_i , \quad (3.22)$$

where  $\vec{d}_e$  is the exit direction,  $\vec{d}_i$  is the incident direction, and  $\vec{n}$  is surface norm. During this process, the ray's wavenumber remains constant, but the energy will decrease to a fraction  $\rho$  of its original energy. Symmetry boundaries also can be described by this specular reflection.

## 3.2 Accelerated approaches to MCRT

### 3.2.1 Adaptive Emission Model

Oftentimes, only a small number of computational cells within a combustion-CFD domain have high temperatures and therefore high degrees of radiative emission. Under these circumstances, a uniform emission model, where the number of rays emitted from each cell is the same, will result in a large number of rays with small amounts of energy. These rays may contribute a significant computational expense while contributing little information to the overall RTE solution. The adaptive emission model is a solution to this problem. In this approach, the number of rays emitted from each computational cell is decided by the emissive power of that cell [84]. Given a user-defined target number of rays  $N_{rays,tot,target}$ , the target ray-energy can be calculated as

$$E_{ray,target} = \frac{\sum_i^{N_{cells}} E_i}{N_{rays,tot,target}} , \quad (3.23)$$

where  $E_i$  is the emissive power from cell  $i$  and  $N_{cells}$  is the total number of cells in the mesh. Given this target ray-energy, the number of rays emitted from any given cell  $j$  can be

calculated as

$$N_{rays,cell,actual} = \left\lceil \frac{E_i}{E_{ray,target}} \right\rceil , \quad (3.24)$$

and the actual ray energy as

$$E_{ray,actual} = \frac{E_i}{N_{rays,cell,actual}} . \quad (3.25)$$

### 3.2.2 Monte Carlo reformulations

The forward Monte Carlo method is the most common implementation of MCRT and is useful to provide knowledge of the overall radiation field [78]. However, alternative methods have been proposed that provide unique advantages under various circumstances. Many of these methods rely on an inversion of the radiation problem, so rays can be traced back to their point of origin, a concept that relies on the reciprocity principle of radiation [85].

#### Backwards/Reverse Monte Carlo

It is often necessary to evaluate the incident radiation upon a point or small surface, such as a radiometer or a motion detector. Applying the forward-MC approach would result in be an exhaustive calculation, as only a small portion of the rays would reach the point of interest. It would be more convenient to exclusively compute rays which are known in advance to arrive at that point. Backwards Monte Carlo provides a more efficient route for this type of problem. Instead of tracing rays from their points of emission, rays are instead traced backwards from their points of absorption. Instead of allocating ray energies based on the emitting computational cell, rays are instead backtracked from the "destination cell", back through their "emission cells", while accumulating the energy emitted from each cell along the way. After a sufficient optical distance, it is reasonable to assume that no significant radiation would be contributed from any further radiation along the path length, and the accumulated intensity of the ray is deposited into the "destination cell". This approach is common in

radiation modeling, and can be applied to transient radiative transfer problems [86] and semi-transparent media [87].

The BMC (backwards Monte Carlo) approach is based on the principle of reciprocity approach formally derived by Case [85] and expanded to participating media by Walters and Buckius [88]. Further background regarding the method can be found in texts by Modest [89] and Howell et al. [19].

The RTE, Eq. 2.9, can be inverted for to calculate intensity at a point  $\mathbf{r}_i$  and direction  $-\hat{s}_i$  as

$$I_\eta(\mathbf{r}_i, -\hat{s}_i) = \epsilon_\eta(r_w) I_{b\eta}(r_w) \exp \left[ - \int_0^l \kappa(r') dl' \right] + \int_0^l \left\{ \kappa_\eta(r') I_{b\eta}(r') \exp \left[ - \int_0^{l'} \kappa_\eta(r'') dl'' \right] \right\} dl' , \quad (3.26)$$

where  $l$  defines the distance along the ray's path. Equation 3.26 provides a method to solve the RTE in a reverse manner. Assuming piece-wise homogeneity, Eq. 3.26 can be reformulated into

$$I_\eta(\mathbf{r}_i, -\hat{s}_i) = \epsilon_\eta(r_w) I_{b\eta}(r_w) \exp \left[ - \sum_{m=1}^M \kappa_{\eta,m} (l_{m_{out}} - l_{m_{in}}) \right] + \sum_{m=1}^M \left( I_{b\eta}(T_m) \left\{ \exp \left[ - \sum_{p=1}^{m_{in}} \kappa_{\eta,p} (l_p - l_{p-1}) \right] - \exp \left[ - \sum_{p=1}^{m_{out}} \kappa_{\eta,p} (l_p - l_{p-1}) \right] \right\} \right) . \quad (3.27)$$

for  $M$  intersected cells along the ray's path. Equation 3.27 can then be solved in stochastic form using the Monte Carlo method.

Equation 3.27 offers a physical description of the back-tracking of a ray. As the ray travels in the reverse direction, it passes through a series of computational cells. As the ray is traced, each intersected computational cell contributes a portion of the net energy deposited to the ray's originating cell. The energetic contribution of each of the passing cells is accounted for alongside a transmissivity term to determine their contribution's decay before arriving at the originating cell. After tracing a multitude of ray samples, the net radiative absorption

within the originating cell is evaluated as

$$E_{abs} = \frac{4\pi\kappa_p}{N_{rays}} \sum_j^{N_{rays}} I_j(\mathbf{r}, \mathbf{s}_i) . \quad (3.28)$$

## Reciprocal Monte Carlo

Reciprocal Monte Carlo<sup>1</sup> is a variance reduction technique that relies on evaluations of the net exchange of power between two computational cells or surfaces. Following Howell et al. [90], a close look at the forward and reverse Monte Carlo methods discussed previously reveals that the first law of thermodynamics is enforced by ensuring that the energy emitted from one computation cell and deposited to another computational cell will be equal values. However, the second law of thermodynamics is only imposed stochastically. This is evident when considering the exchange of energy between cells. The second law states that there should be a net energy exchange from a cell of higher temperature to a cell of lower temperature. For the discussed methods so far, this rule may be violated when the higher temperature cell does not emit a statistically significant number of rays that intersect the lower temperature cell, or vice-versa. The approach in the reciprocal Monte Carlo implementation is to embed the requirement of both first and second law satisfaction in the model; as a result, reciprocal Monte Carlo theoretically has lower variance compared to the forward and reverse Monte Carlo methods [90].

Several implementations of reciprocal Monte Carlo methods have been proposed by Tessé et al. [17] and Dupoirieux et al. [91]. These include the Emission reciprocity method (ERM), absorption reciprocity method (ARM), and a hybrid of the two, optimized reciprocity method (ORM).

A complete solution to the RTE would require the evaluation of all power exchanges,  $P_{i,j}^{exch}$ , between every pair of surfaces and cells ( $i, j$ ) in the domain. The net power exchange for one particular object  $P_q$  can thereafter be evaluated as the sum of net power exchange

---

<sup>1</sup>Also referred to as direct-exchange MC in the text by Modest and Mazumder [78].

with every other object as

$$P_q = \sum_{j=1}^{N_v+N_S} P_{qj}^{exch} = - \sum_{j=1}^{N_v+N_S} P_{jq}^{exch}, \quad (3.29)$$

where  $N_V$  and  $N_S$  are all of the volumes and surfaces within the geometry, and  $P_{ab}$  defines the net power exchange from object  $b$  into object  $a$ . ERM and ARM differ in which term they attempt to estimate: ERM estimates the first summational term of Eq. 3.29, and ARM estimates the second summational term of Eq. 3.29. In ERM, the estimated value for a spectral power exchange from a volume  $j$  into a volume  $q$  can be evaluated as

$$P_{qj\eta}^{ERM} = 4\pi\kappa_{q\eta} V_q (I_{bj\eta} - I_{bq\eta}^0) A_{qj\eta}, \quad (3.30)$$

where the spectral power exchange can be related to the net power exchange as  $P_{qj}^{exch} = \int_0^\infty P_{qj\eta}^{exch} d\eta$ . Meanwhile, for ARM, the exchange is evaluated as

$$P_{jq\eta}^{ARM} = 4\pi\kappa_{j\eta} V_j (I_{bq\eta} - I_{bj\eta}^0) A_{jq\eta}. \quad (3.31)$$

$A_{jq\eta}$  represents the fraction of spectral power emitted by cell  $j$  that is absorbed by cell  $q$ , and often requires a stochastic solution using the Monte Carlo method. Additional formulations for  $A$  between surfaces, and surfaces and volumes can be found in Dupoirieux et al. [91].

Dupoirieux et al. [91] later presented a mathematical description of the variance of the two procedures ERM and ARM. It was determined that the standard deviation of ERM is lower than that of ARM when the temperature  $T_q$  is larger than  $T_j$ , and conversely ARM is more precise under the opposite condition. Therefore, the procedure conducted in ORM is to select which to evaluate at runtime for every pair exchange by comparing the relative temperatures between the two objects.

With the net power exchange being evaluated instead of the one-sided contribution of one cell to other cells (forward MC), and from other cells into one cell (backward MC), the total number of ray histories being tracked through one tracing procedure is increased. Therefore, the information obtained through one tracing of reciprocal MC is generally greater than that of the other presented approaches.

## Null-collision Monte Carlo

The null-collision Monte Carlo method applies a Russian-roulette approach to MCRT. The descriptions of the MCRT methods presented so far have implied that it is necessary to trace a ray through the CFD mesh. This requirement exists for determination of either ray energy depositions (forward MC), emission contributions (backward MC), or power exchange (reciprocal MC). The reason for tracing originates from the expected variability of extinction coefficient  $\beta_\eta$  along a ray's path. This variability is nearly guaranteed; the spatial inhomogeneity of the system's temperature, pressure, chemical composition all results in spatial in-homogeneity of the ray's extinction coefficient. The ray must be traced through each computational cell to explicitly evaluate the interaction of the ray with that cell. However, if one could assume homogeneity in  $\beta_\eta$ , no mesh tracing procedure would be required. The interaction of the ray with the surrounding medium could be assumed uniform along the ray's travel. This is the intention behind the null-collision algorithm [20, 92].

The principle of null collision is to redefine the extinction coefficient as,

$$\beta_\eta = \kappa_\eta + \sigma_\eta + \kappa_{\eta,null} , \quad (3.32)$$

where an additional null-collision coefficient  $\kappa_{\eta,null}$  has been introduced in addition to the absorption coefficient  $\kappa_\eta$  and scattering coefficient  $\sigma_\eta$ . The value of this coefficient is defined as the exact value that allows for  $\beta_\eta$  to remain constant throughout the ray's travel. The random number relation for extinction, from Eq. 3.10, is

$$\tau_{extinct} = \ln \frac{1}{R_\beta} . \quad (3.33)$$

and the length propagated before ray extinction,  $s_{ext}$  is evaluated through inversion of

$$\tau_{ext,\eta} = \int_0^{s_{ext}} \beta_\eta \, ds . \quad (3.34)$$

Usually, the inversion of Eq. 3.34 requires tracing through the mesh, as mentioned previously, to calculate the change in  $\beta_\eta$ . However, with the introduction of the null-collision coefficient

$\beta_\eta$  is no longer a function of  $s$  and can be removed from the integral and Eq. 3.34 can be simplified to  $\tau_{ext,\eta} = \beta_\eta s_{ext}$ . Therefore, inversion may be completed analytically as  $s_{ext} = \tau_{ext,\eta}/\beta_\eta$ .

With this change, the tracing procedure may proceed as follows. When the ray is first initialized, the optical distance before extinction is randomly determined using Eq. 3.33, and the resulting extinction distance,  $s_{ext}$ , is evaluated analytically using  $s_{ext} = \tau_{ext,\eta}/\beta_\eta$ . After the ray has travelled this distance, a new absorption coefficient and scattering coefficient are determined, and a random number,  $R$  is drawn again. The random number is used in a round of Russian-roulette. The ray is terminated if  $R < \kappa_\eta/\beta_\eta$ , scattered if  $\kappa_\eta/\beta_\eta < R < (\kappa_\eta + \sigma_\eta)/\beta_\eta$  and continues propagation if  $R > (\kappa_\eta + \sigma_\eta)/\beta_\eta$ . The null collision event can therefore be thought of as a scattering event, but with no change in direction.

Null-collision was re-introduced to the field of stochastic modeling of radiation and graphics rendering by Galtier et al. [20]. Since then, null-collision has seen a growth in usage as an alternative to the traditional approach of tracing through a grid. Various interpretations of the algorithm are offered by El Hafi et al. [93], each revealing a new perspective and application for the method. The method has been applied under a variety of circumstances with recent extensions to Monte Carlo evaluation of spectroscopic parameters [94], Oct-tree methods for an optimal evaluation of extinction locations [95], and combustion simulations [92].

### 3.2.3 MPI acceleration

The all-to-all nature of MCRT results in poor scaling with increasing mesh size. With large enough simulations, the system geometry is divided into separate regions that are computed on different computers, called nodes, on a high performance computing system. When the ray-tracing procedure begins, rays must be traced through the mesh on one node before being communicated to another node for continued tracing. Ray-cell interactions may occur

between a ray emitted on one side of the medium, and a cell located on the other side. The resulting communication overhead required by the Message Passing Interface (MPI)<sup>2</sup>, can dramatically slow the computation. Additionally, the sequential nature of raytracing limits these MPI communications to an iterative sequence of communications between adjacent MPI ranks<sup>3</sup>. This results in a series of "MPI iterations" where rays are forced to wait at the boundary of one MPI rank before being communicated to the adjacent rank as a group. This wait time significantly reduces the performance and limits the scalability of the solver.

## Mesh Coarsening

Mesh coarsening is one approach to alleviate this problem. The approach is to localize all mesh information within a node to prevent any MPI communications. To store the full mesh on one node would violate one of the main purposes of a distributed-memory simulation, so a mesh coarsening approach is imposed, where the mesh is less-refined at increasing distances from the point of emission. The coarsened mesh reduces the memory load required to store the mesh. Several layers can be added of increasing degree of coarsening further from node of interest. The concept capitalizes on the local nature of thermal radiation: while radiation can travel long distances, in many circumstances, the radiation will have its most significant contributions local to the point of emission. The following explanation follows that of Silvestri and Pecnik [24].

The transmitted radiative intensity through a mesh follows an exponential decay function of intersection length and absorption coefficient, proportional to

$$I_{transmit} \sim \exp(-\kappa_\eta \Delta s), \quad (3.35)$$

It is immediately apparent that the majority of ray absorption occurs at lower optical distances. This suggests that a coarsening of the mesh at larger optical distances (further from

---

<sup>2</sup>MPI is the parallel execution standard for distributed memory computers. It defines the syntax in C/C++/Fortran code used to communicate with other nodes in the high performance computer (HPC).

<sup>3</sup>An MPI rank, in this case, is an instance of a parallel execution process within MPI.

the point of emission) can reduce computational runtime while maintaining a similar degree of accuracy. The ray will be emitted and traced within the fine mesh locally, and transferred to a coarsened mesh after a prescribed number of grid steps. Resulting, in total, for a reduced number of ray-cell calculations, and also the potential to store the entirety of the mesh on a single node, in a coarsened manor.

The idea has been implemented a limited number of times, but with much success. Silvestri and Pecnik [24] presented speedups approximately equal to the number of coarsened layers within a structured mesh, along with an method to optimally select the number of cells a ray should travel before coarsening and obtained an order of magnitude reduction in runtime. Humphrey et al. [23] applied a similar concept to a gray reverse Monte Carlo model within a structured mesh. Kelm et al. [96] applied the OpenFOAM-embedded LaGrangian particle tracking library to radiation transport in their solver, `containmentFoam`, which uses a global mesh to prevent MPI communications.

Several possible issues remain within the method, however. For one, the requirement of a user specified number of grid steps inserts a certain degree of potential error into the calculation. The model is restricted in accuracy and applicability to only those who understand its limitations. A sufficiently general model could be applied under any circumstance, without user choice. Additionally, the model has the potential to introduce Turbulence-Radiation Interaction (TRI)-related effects into the simulations. Even if appropriate averaging is conducted (averaging the complete emissive power term from each cell, weighted by cell volume) the usage of a spatially-averaging model is questionable for TRI-related studies, particularly within the context of absorption-TRI. Finally, the implementation of a non-gray modeling with such models appears to be inefficient [80].

## Distributed Raytracing

In this research, a new technique for MCRT on multi-MPI rank simulations is presented for accelerated ray tracing. This approach reformulates the backwards Monte Carlo method

presented previously to accelerate the model on distributed-memory systems. To begin, the formulation for ray back-tracing is repeated for convenience as,

$$I_\eta(\mathbf{r}_i, -\hat{s}_i) = \epsilon_\eta(r_w) I_{b\eta}(r_w) \exp \left[ - \sum_{m=1}^M \kappa_{\eta,m} (l_{m_{out}} - l_{m_{in}}) \right] \\ + \sum_{m=1}^M \left( I_{b\eta}(T_m) \left\{ \exp \left[ - \sum_{p=1}^{m_{in}} \kappa_{\eta,p} (l_p - l_{p-1}) \right] - \exp \left[ - \sum_{p=1}^{m_{out}} \kappa_{\eta,p} (l_p - l_{p-1}) \right] \right\} \right). \quad (3.36)$$

This formulation can be rewritten as,

$$I_\eta(\mathbf{r}_i, -\hat{s}_i) = \epsilon_\eta(r_w) I_{b\eta}(r_w) \exp \left( - \sum_m^{e_1 \rightarrow e_{N+1}} \tau_{\eta,m} \right) \\ + \sum_m^{e_1 \rightarrow e_{N+1}} \left\{ I_{b\eta}(T_m) \left[ \exp \left( - \sum_p^{e_1 \rightarrow m} \tau_{\eta,p} \right) - \exp \left( - \sum_p^{e_1 \rightarrow m+1} \tau_{\eta,p} \right) \right] \right\}, \quad (3.37)$$

where  $\tau_{\eta,m}$  is the spectral optical distance in the  $m$ th cell along the ray's path,  $e_1$  is the emitting computational cell,  $e_i$  is the entrance computational cell in  $i$ th MPI rank along the ray's path,  $N$  is the number of ranks intersected, and  $e_1 \rightarrow i$  represents the sequence of computational cells between the emitting computational cell up to but not including the  $i$ th cell intersected. This formulation is a description of the tracing of a ray accounting for the various MPI ranks, with the exception that the ray terminates at the exit point of its last MPI rank instead of at any computational cell within a rank as before. With this change, the ray tracing procedure can be described as,

$$I_\eta(\mathbf{r}_i, -\hat{s}_i) = \epsilon_\eta(r_w) I_{b\eta}(r_w) \exp \left( - \sum_m^{e_1 \rightarrow e_{N+1}} \tau_{\eta,m} \right) \\ + \sum_n^N \sum_m^{e_n \rightarrow e_{n+1}} \left\{ I_{b\eta}(T_m) \left[ \exp \left( - \sum_p^{e_1 \rightarrow m} \tau_{\eta,p} \right) - \exp \left( - \sum_p^{e_1 \rightarrow m+1} \tau_{\eta,p} \right) \right] \right\}. \quad (3.38)$$

The inner sums can be made independent of all preceding MPI ranks by splitting the sum and factoring the exponential term, as

$$I_\eta(\mathbf{r}_i, -\hat{s}_i) = \epsilon_\eta(r_w) I_{b\eta}(r_w) \exp \left( - \sum_m^{e_1 \rightarrow e_N} \tau_{\eta,m} - \sum_m^{e_N \rightarrow e_{N+1}} \tau_{\eta,m} \right) \\ + \sum_n^N \sum_m^{e_n \rightarrow e_{n+1}} \left\{ I_{b\eta}(T_m) \left[ \exp \left( - \sum_p^{e_1 \rightarrow e_n} \tau_{\eta,p} - \sum_p^{e_n \rightarrow m} \tau_{\eta,p} \right) \right. \right. \\ \left. \left. - \exp \left( - \sum_p^{e_1 \rightarrow e_n} \tau_{\eta,p} - \sum_p^{e_n \rightarrow m+1} \tau_{\eta,p} \right) \right] \right\}, \text{ and} \quad (3.39)$$

$$I_\eta(\mathbf{r}_i, -\hat{s}_i) = \epsilon_\eta(r_w) I_{b\eta}(r_w) \exp \left( - \sum_m^{e_1 \rightarrow e_N} \tau_{\eta,m} \right) \exp \left( - \sum_m^{e_N \rightarrow e_{N+1}} \tau_{\eta,m} \right) \\ + \sum_n^N \exp \left( - \sum_p^{e_1 \rightarrow e_n} \tau_{\eta,p} \right) \sum_m^{e_n \rightarrow e_{n+1}} \left\{ I_{b\eta}(T_m) \left[ \exp \left( - \sum_p^{e_n \rightarrow m} \tau_{\eta,p} \right) \right. \right. \\ \left. \left. - \exp \left( - \sum_p^{e_n \rightarrow m+1} \tau_{\eta,p} \right) \right] \right\}, \quad (3.40)$$

where  $\exp \left( - \sum_p^{e_1 \rightarrow e_n} \tau_{\eta,p} \right)$  has been separated from the interior summational term. The entire equation for  $I_\eta(\mathbf{r}_i, -\hat{s}_i)$  may then be represented as a function of three components

$$I_\eta(\mathbf{r}_i, -\hat{s}_i) = I_{bndry} \exp \left( - \sum_l^N \tau_{\eta,l} \right) + \sum_n^N I_{cont,n} \exp \left( - \sum_l^{n-1} \tau_{\eta,l} \right). \quad (3.41)$$

$I_{bndry}$ ,  $\tau_{\eta,l}$ , and  $I_{cont,n}$  are the intensity contribution from the boundary, the optical distance traversed through rank  $l$ , and the intensity contribution from rank  $n$  without consideration of the decay of that contribution before reaching the absorbing cell, respectively. These three terms are defined as:

$$I_{bndry} = \epsilon_\eta(r_w) I_{b\eta}(r_w) \exp \left( - \sum_m^{e_N \rightarrow e_{N+1}} \tau_{\eta,m} \right), \quad (3.42)$$

$$\tau_{\eta,l} = \sum_p^{e_n \rightarrow e_{n+1}} \tau_{\eta,p}, \text{ and} \quad (3.43)$$

$$I_{cont,n} = \sum_m^{e_n \rightarrow e_{n+1}} \left\{ I_{b\eta}(T_m) \left[ \exp \left( - \sum_p^{e_n \rightarrow m} \tau_{\eta,p} \right) - \exp \left( - \sum_p^{e_n \rightarrow m+1} \tau_{\eta,p} \right) \right] \right\}. \quad (3.44)$$

With this change, both Eqs. 3.43 and 3.44 are each functions of only the cells local to an MPI rank. Therefore, each MPI rank may calculate these terms asynchronously for a given ray. Subsequently, the originating MPI rank of a ray may iterate the  $\tau_{\eta,l}$  and  $I_{cont,n}$  terms from each MPI rank to evaluate the net accumulated intensity Eq. 3.41 which is deposited into the originating cell of the ray. The advantages of this approach are discussed further in section 3.3.2.

### 3.2.4 Ray Tracing in computer graphics

Many improvements to ray tracing have been introduced in recent years capitalizing on advancements in computational hardware and algorithms. These improvements have largely been focused in the field of computer graphics, owing in large part to the dramatic increase in the desire for fast and detailed visualization software [97]. The vast knowledge obtained through extensive work to accelerate ray-tracing would be of significant value to many heat transfer researchers, but has historically been ignored [22]. In particular, the increased involvement of the Graphics Processing Unit (GPU) has resulted in dramatic boosts in computational efficiency, but has been used relatively few times in radiation modeling. Additionally, the bounding volume hierarchy (BVH) provides a optimal data structure to accelerate the geometric search procedure of the ray-tracing process.

#### Graphics Processing Units (GPUs)

GPUs offer high throughput for highly parallelizable, compute-bound problems. GPUs differ from Central Processing Units (CPUs) because of the increased attention to hiding latency through raw data parallelism as opposed to minimizing cache access time [98]. This Single Instruction Multiple Data (SIMD) approach is optimized because the GPU structure has more area dedicated to the data processing as opposed to the cache and control unit on the CPU [97]. At its origin, the GPU was used for the acceleration of graphical visualization of

games and animation rendering. Today, GPUs are applied in vast number of fields for more general purposes (GPGPUs).

Computational scientists in particular have begun to take advantage of GPUs in their fields of study. In the hybrid computing model, a central processing unit (CPU) offloads compute-intensive and time consuming parts of the code to the GPUs. By applying this model, users can selectively offload the necessary parts of the code to the GPU, while maintaining others on the CPU.

While many fields have seen considerable improvements with GPUs, thermal radiation modeling has seen them applied relatively few times. This comes as a surprise seeing that MCRT in particular carries many similarities to the ray-tracing in computer graphics [81]. Alerstam et al. [99] applied GPUs to accelerate their modeling of photon migration in biomedical optics and observed over three orders of magnitude speedup over CPU implementations. Heymann et al. [100] applied GPUs to accelerate their ray tracing in galactic nuclei and observed speedups of over 100 times over serial code. Humphrey et al. [80] applied heterogeneous computing for their combustion CFD code, using GPUs for ray tracing and CPUs for combustion modeling. They recently extended their code to use the `Kokkos` programming model [25] and achieved 80 times speedup using GPUs [101]. Finally, Silvestri and Pecnik [24] applied GPUs to their non-gray code for coupling to turbulent flow calculations and observed speedups approaching three orders of magnitude.

## Bounding Volume hierarchy

At its simplest form, the bounding volume hierarchy (BVH) is a tree-based data structure which can be used to represent a series of objects in space [102, 103]. The usage in computer graphics is to detect intersections between a ray and a far-away object with logarithmic algorithm time complexity (traversal through a tree), rather than linear time complexity (test each object one at a time) [81].

BVHs are constructed by first wrapping the objects, e.g., surfaces in a graphical visual-

ization, in Axis Aligned Bounding Boxes (AABBs). In a cartesian coordinate system, the box cornerpoints can be determined using the maximum and minimum X, Y, and Z coordinates of the object. This ensures that an intersection of the ray with the object cannot occur without an intersection of the ray with the bounding box, and the detection of ray/box intersections is extremely fast [82]. The object-level AABBs represent the leaf nodes of the binary tree. These boxes are then wrapped in larger bounding-boxes, and the procedure repeats until there is one bounding box which wraps around the whole domain, which represents the root node of the BVH. For a binary tree, each node must have only two child nodes. The ray-tracing procedure can then proceed iteratively down the tree, rejecting nodes and their children that the ray does not intersect, until a final list of leaf nodes are left.

Graphics processing exhibits massive speedup with the use of the BVH data structure, especially with recent approaches using GPUs [103, 104, 105]. However, BVHs see almost no usage in thermal radiation modeling [7]. Kuczyńska and Bialecki [106] for one, were able to accelerate computation of thermal radiation between faces with non-participating media. Also, Mazumder [107] compared the BVH approach with a spatial-partitioning approach known as volume-by-volume advancement and found the BVH to be slower for surface-to-surface calculations. There apparently exist no applications of the BVH to participating media in thermal radiation modeling. However, alternative approaches, such as the oct-tree approach where a mesh is refined in regions of increased opacity, have been introduced and shown to provide significant speedups over traditional ray tracing [95, 108].

### 3.3 Implementation for this Research

In this research we create a combined combustion CFD and Monte Carlo radiation solver named MCRT-GPU. This solver applies Graphics Processing Units and Bounding Volume Hierarchies to accelerate the ray tracing process. Multiple variations of the solver are implemented to assess the performance benefits of GPUs and BVHs under different configurations.

The different variations rely on either forward or reverse Monte Carlo formulations and are tested and timed in both shared and distributed-memory environments in Chapter 4.

The flow chart in Fig. 3.4 provides a general summary of how the radiation solver couples to the CFD, and section 3.3.2 details the ray tracing methods. The MCRT solver first reads the mesh and cell parameters from OpenFOAM, including temperature, pressure, and chemical species mole fractions. The radiation-relevant data are then ‘deep-copied’ into the device-accessible memory space in preparation for the ray-tracing procedure (i.e. CPU to GPU memory transfer is conducted, if a GPU is employed). An optional line-by-line non-gray model [109] is included in the solver to account for the non-gray influences of the major emitting chemical species in hydrocarbon flames: CO<sub>2</sub>, H<sub>2</sub>O, CO, and soot. The line-by-line tables are read from a user-defined directory and deep-copied into GPU texture memory if a GPU is in use. *Texture memory* is an NVIDIA feature that enables faster read-only memory. Alternatively, the user has the option to conduct a gray calculation using a uniform absorption coefficient or the local Planck-mean absorption coefficient.

A parallel execution process calculates the radiative emission from each of the computational cells and delegates the emitting energy among the rays emitted from that cell. The number of rays emitted per cell may be defined manually or using the adaptive emission approach, where cells with higher radiative emission are provided more rays (see section 3.2.1). Subsequently, the ray tracing procedure begins the asynchronous tracing of the rays using a multitude of threads.

### 3.3.1 Supplemental Libraries

MCRT-GPU relies on several external libraries for the computation of the CFD, for a bounding volume hierarchy, and for parallelization.

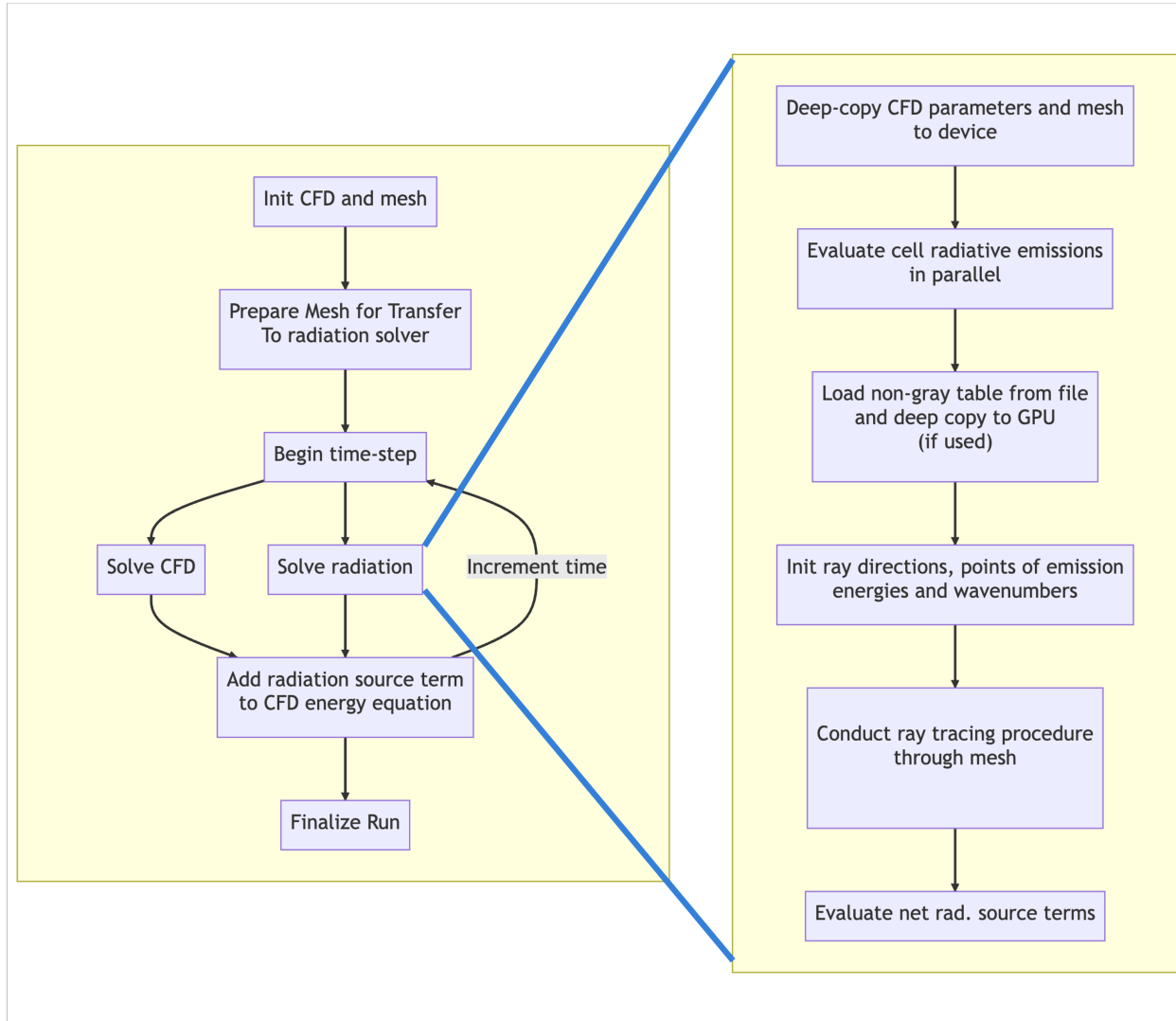


**Figure 3.4** Flow chart of coupled combustion-CFD and MCRT implementation. The left box refers to the overall coupled code, while the right box details the radiation solver only. The solver at its current state can solve radiation on the Kokkos device (i.e. GPU, if available, else CPU) and CFD on the CPU. A deep-copy is a data transfer from host to device. The ray tracing procedure follows the implementations listed in section 3.3.2.

## OpenFOAM

By coupling to the OpenFOAM open-sourced CFD solver, this code can be applied to any combustion application from aeronautical engines to fire suppression and management [26]. OpenFOAM provides an extensive list of supplemental libraries, allowing the user to simulate using Reynolds Average Navier-Stokes (RANS), Large Eddy Simulation (LES), or Direct Numerical Simulation (DNS) approaches with multi-phase flow and detailed chemistry. Transient simulations can be implemented with MCRT-GPU on any polyhedral, unstructured mesh. Users can adapt their own OpenFOAM solvers to use MCRT-GPU, or use the default examples for reactingFoam and fireFoam.

## Kokkos

Kokkos is a performance-portable programming model from the Department of Energy [25, 110]. Targeted for HPCs, Kokkos provides abstractions over the parallel execution process and memory management in many solvers. By programming in Kokkos, the user can avoid the complications of the underlying parallel execution process and maintaining portability and instead focus on implementing code. Kokkos supports CUDA, HIP, SYCL, HPX, OpenMP and C++ threads as parallel backends, which the user can easily switch between at compile time. Additionally, the `Kokkos-tools` repository streamlines the debugging and profiling process [111]. For this solver, Kokkos::Cuda, Kokkos::OpenMP, and Kokkos::Serial back-ends are used as execution and memory spaces. Kokkos includes access to Cuda Unified Virtual Memory (UVM), an abstraction allowing for variables to live in CPU and GPU memory simultaneously, but it is not used in this solver due to performance drawbacks and limitations on multi-GPU computing systems.

## ArborX

Following the Bounding Volume Hierarchy (BVH) description from Karras [105], the ArborX C++ library provides an implementation for both spatial-search and nearest-neighbor geometric search calculations using a BVH [28]. The ArborX application programming interface enables usage of the BVH through a two-step process: construction and traversal. The user can define *primitives*, or underlying objects with labeled bounding-boxes, and ArborX will efficiently construct a balanced BVH around the primitives in parallel. Then, the user can define *predicates* which define the operation the traversal process will be conducting (i.e. spatial or nearest query) while traversing the tree. MCRT-GPU currently contains several code branches that apply the ArborX library to optimize the ray-tracing procedure in different ways.

ArborX uses Kokkos as a backend for on-node parallelism, and implements additional MPI functionality to extend the BVH query process across multi-node runs. Distributed memory executions proceed through an top-tree and bottom-tree approach for each MPI rank. The bottom tree of a rank consists of *primitives* that are CFD cells. The bounding box for every cell is determined using the maximum and minimum X, Y, and Z coordinates of each cell; these boxes are designated leaf nodes in the BVH. Every pair of leaf nodes are wrapped in another bounding box defined using maximum and minimum coordinates for the pair, and those bounding boxes are then paired and wrapped in bounding boxes again. The process repeats with increasing box size until only one bounding box remains, called the *scene* bounding box. Each MPI rank contains one scene bounding box to encompass the entire MPI rank region. The top-tree is constructed using the scene bounding boxes for all MPI ranks as primitives, and each MPI ranks contains a copy of the same top-tree. MCRT-GPU applies ray-tracing procedure by first traversing the top-tree to determine the intersected MPI ranks by each ray. Then, the rays are MPI communicated to their destination ranks and traced using the bottom-trees. Further discussion is provided in section 3.3.2.

**Table 3.1** Variations of the present MCRT solver algorithm. All variations rely on the Kokkos programming model for parallelization and OpenFOAM for CFD computation, while only Bounding Volume Hierarchy and Hybrid approaches use ArborX. Bold solvers are the primary tested versions.

	Standard	Bounding Volume Hierarchy	Hybrid
Forward-MC	<b>Standard-Forward</b>	ArborX-Forward	N/A
Reverse-MC	Standard-Reverse	<b>ArborX-Reverse</b>	<b>Hybrid-Reverse</b>

### 3.3.2 Summary of ray tracing procedures presented in this study

The various implementations of the present ray tracing procedure solver are presented in Table 3.1. Different variations are tested in attempt determine the optimal configuration for performance and scalability. Both forward and reverse Monte Carlo approaches are included, and all methods feature the Kokkos-embedded GPU capabilities discussed previously.

#### Standard-Forward

The Standard-Forward MCRT approach is the classical implementation of MCRT and follows the description in section 3.1 and the pseudocode presented in Algorithm 1. In this model, rays are emitted from their points of emission, traced through the CFD mesh, and deposit energy as they travel. The tracing procedure follows an iterative approach where a ray's exit face in a cell determines the next cell intersected. Likewise, if run with distributed-memory parallelism, the ray's exit boundary of an MPI rank determines the next MPI rank that is intersected. Under these conditions, as discussed in section 3.2.3, the tracing procedure for a given ray must be conducted one MPI rank at a time, and multiple MPI communications may be required before the ray is terminated.

As a whole, each MPI rank first conducts the tracing procedure for all rays emitted from within themselves. For any rays that intersect a "processor boundary", a boundary to another MPI rank, they are sorted by destination MPI rank and then MPI communicated to those ranks. Each MPI rank then traces all of the new rays internally, and the process

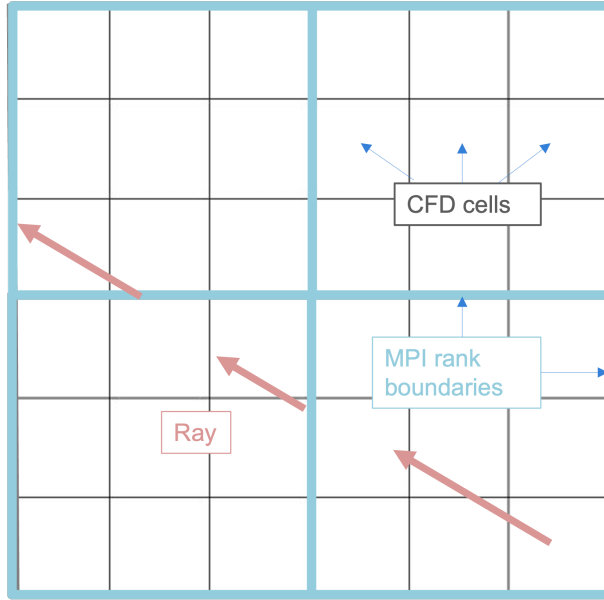


**Figure 3.5** A depiction of a ray being traced across multiple MPI ranks simultaneously. Within ArborX, the top-tree is constructed around MPI rank boundaries, and the bottom-trees are constructed of CFD cells.

repeats until all rays are terminated. The number of "MPI iterations" that are conducted with this approach varies depending on the number of ranks, the opacity of the medium, the boundary conditions, and the case geometry. No ray scattering events are modeled, but ray reflections and wall-absorption are included.

### ArborX-Forward

ArborX-Forward is the first implementation to apply the BVH for acceleration. The ray-tracing procedure is visualized in Fig. 3.5. The process follows the traversal approach defined in the BVH discussion in section 3.2.4 and the ArborX discussion in section 3.3.1 where a top tree is constructed around MPI ranks and each MPI rank's bottom tree is constructed using computational cells. Then, traversal proceeds through the top tree and then the bottom tree.

For each ray, the top-tree is first traversed to determine the remote MPI ranks that a ray intersects. Then, the rays are MPI communicated within ArborX to the remote ranks.

Each MPI rank conducts a traversal of the bottom-tree to determine the computational cells that are intersected by each ray. For every ray/cell intersection that is found, a callback function is invoked to calculate the intersection characteristics of the ray with the cell using the trigonometric calculations defined in section 3.1.2. The distance the ray propagated before entering the cell, the optical distance traversed within the cell, the cell’s ID, the ray’s ID, the ID of any intersected boundaries, and the index intersected along a boundary are then stored in a C-style struct and sent back to the originating MPI rank of the ray. Every ray/cell intersection creates this C struct, and all of these structs are sent back to the ray’s originating rank as a group. This collective send of data from every ray/cell intersection is prohibitively memory intensive, as will be discussed in Chapter 4. The originating rank then receives these lists of structs for each ray, and sorts them by ray intersection distance. The sorted structs are then processed in order of intersection to calculate the energy deposited by each ray to each of its intersected cells. Each MPI rank independently has knowledge of all of its rays’ energetic contributions to all cells, remote and local. To sum the net radiative absorption in all cells, `MPI_AllReduce` is called to conduct an all-to-all summation across every MPI rank. The storage of data for all computational cells in each MPI rank is again memory-intensive and inefficient. An improved method would not `MPI_Allreduce` an array so large, and would instead only accumulate absorption for local cell data. However, due to the computational limitations imposed by the sending of ray/cell data from before, the limitations of this approach are recognized and no further effort is made for improvement.

### **Standard-Reverse**

The standard-reverse tracing procedure applies the reverse Monte Carlo description presented in section 3.2.3. In this method, rays are traced backwards from their points of absorption through emitting cells. The intensities accumulated by all rays from a cell are then averaged and integrated across the field of view ( $4\pi$  steradians for a point in a medium) as shown in Eq. 3.28. The random number relations and algorithm follow exactly that listed in the

Standard-Forward description of section 3.1 with the exception that the rays' accumulate energy gradually instead of deposit energy gradually.

### **ArborX-Reverse**

The ArborX-Reverse implementation follows closely from the ArborX-Forward approach. As before, each ray on every rank is communicated to all of the MPI ranks the ray intersects using the top-tree. After communication, every rank traces each ray using the same bottom-tree traversal discussed previously. However, in reverse ray tracing, the ray/cell interaction determines the energetic contribution of emission of the passing cell to the originating cell of the ray. Therefore, the accumulation of the intensity contribution without decay, the optical distance traversed within the rank, and the boundary intensity contribution is sufficient to predict this intensity, as shown in section 3.2.3, and one struct is created for every ray/rank intersection rather than for every ray/cell intersection. Then, the accumulated values for every ray/rank intersection are sent back to the originating rank of the ray for evaluation of the overall accumulated ray intensity, Eq. 3.41. Finally, the net absorption within the originating cell is calculated by averaging the intensity of all of the cell's rays and integrating over the spherical solid-angle as in Eq. 3.28.

### **Hybrid-Reverse**

The hybrid approach combines standard and ArborX approaches into one. Similar to ArborX-Forward and ArborX-Reverse, Hybrid-Reverse first begins by conducting a traversal of the top-tree to determine the intersected remote ranks. However, unlike either of the two pure-ArborX approaches, the bottom-tree traversal is not conducted using the computational cells as primitives, but instead using the cell faces that fall along the MPI boundaries. In fact, the bottom-tree traversal only determines the first face intersected for each ray sent to a rank. This information is then used to begin a standard-reverse tracing procedure through the mesh where the exit face of the entrance cell determines the next cell intersected. The

solver accumulates the values presented in Eqs. 3.42–3.44 within one C-style struct for every ray/rank intersection, and then sends the C structs back in bulk to the originating ranks. The originating rank then iterates through the collected structs for every ray in order of intersection and completes the evaluation of ray intensities using Eq. 3.41.

# Chapter Four

## Solver Performance

An extensive series of validation and performance studies are conducted in this chapter to demonstrate the effectiveness and efficiency of the present radiation solver. Four test geometries are presented for verification and profiling using the methods discussed in section 3.3.2. The configurations include the canonical one-dimensional plane-parallel medium, a snapshot of large-eddy simulations of a three-dimensional backward-facing step combustor, a snapshot of a direct numerical simulation of a small turbulent pool fire, and a transient small turbulent pool fire. The plane-parallel simulation results are compared against the exact solutions presented in section 2.1.5 as a verification. The three solver implementations presented in section 3.3.2 are used: Standard-Forward, ArborX-Reverse, and Hybrid-Reverse. These three are considered the most-likely candidates for maximized MCRT performance. The best performing method is then used for the remaining studies.

### 4.1 One dimensional plane-parallel medium

The plane-parallel medium is a simple, one dimensional case commonly used to verify radiation solvers. As shown in Fig. 4.1, the geometry consists of two parallel plates surrounding a homogeneous radiatively-emitting and absorbing medium. The blue boundaries are cold, black walls, i.e., they emit negligible radiation but absorb all incident radiation, and the

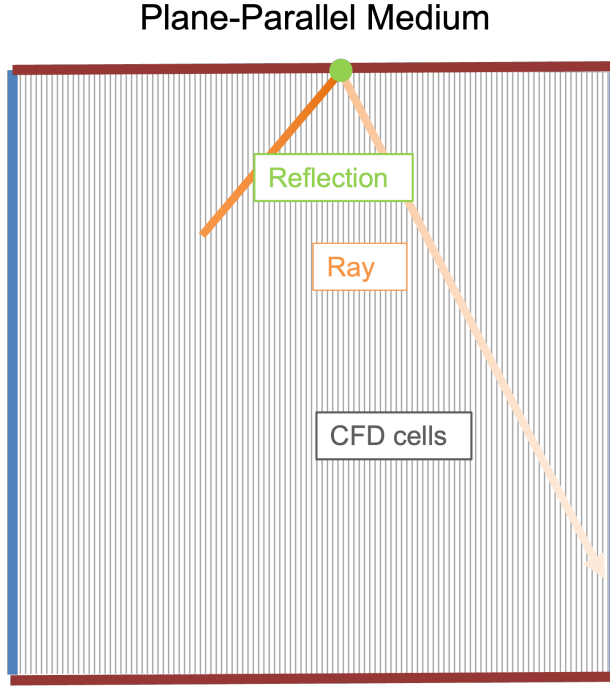


**Figure 4.1** A one-dimensional plane parallel medium. Red walls are symmetric and blue walls are cold and black. Ray is in orange.

red boundaries are symmetry boundary conditions. The boxes in Fig. 4.1 are coarsened representations of the actual cell discretization used in the study. Under present conditions, discretization of 1000 cells in the direction normal to the blue boundary and one cell in the off-normal directions are used. A uniform absorption coefficient and temperature is assigned to the cells, and the medium is frozen in time and simulated for one snapshot. Verification is conducted against the exact solution presented in section 2.1.5. The configuration is first tested under a variety of absorption coefficients and temperatures. The MCRT solution procedure is repeated 50 times for each condition, and 1000 means and standard deviations are calculated for each of the 1000 computational cells in the 1-D domain. Results from all three primary methods listed in section 3.3.2 are tested: Standard-Forward, ArborX-Reverse, and Hybrid-Reverse. First for a single MPI rank and then within multiple MPI ranks. Finally, the effect of varying ray counts is presented.

### 4.1.1 Results for a single MPI rank

The various tracing methods are first tested within a single MPI-rank on a single computing node. Figures 4.2 to 4.3 display comparisons of the volumetric radiative absorption of the mean MCRT results alongside the exact solutions. Results show excellent agreement under all absorption coefficients and temperatures.

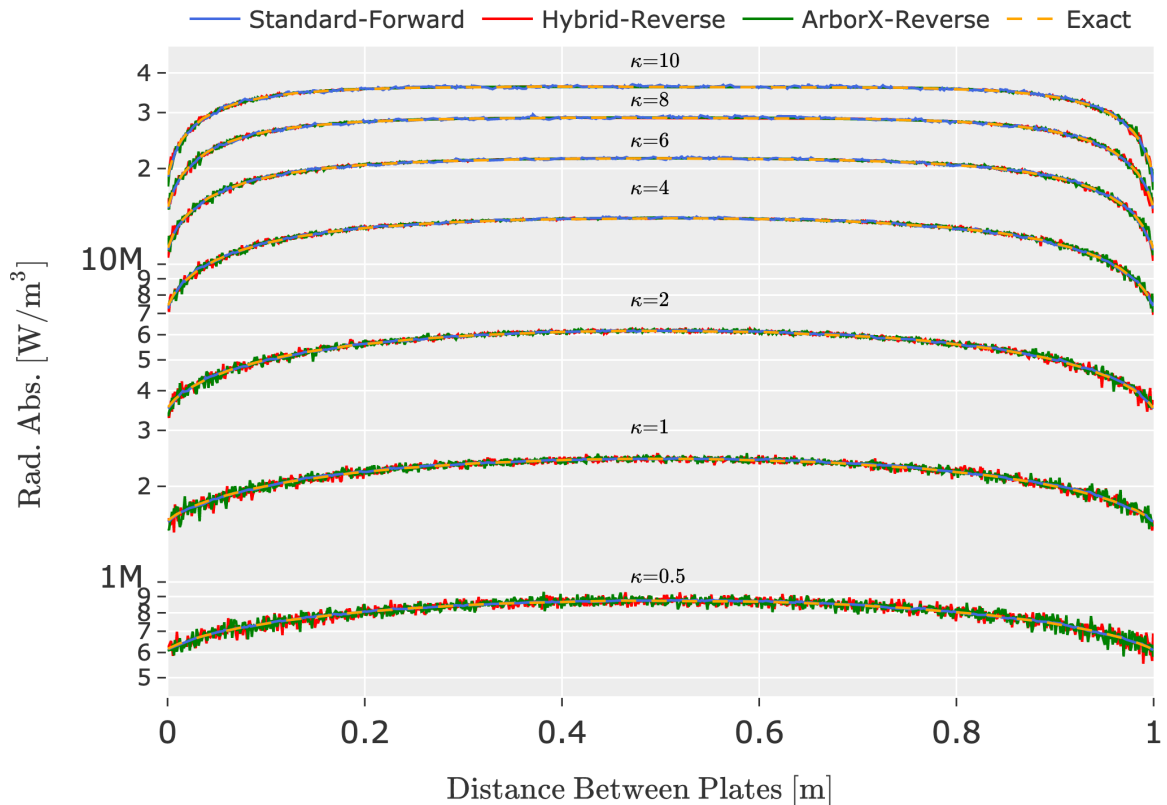


**Figure 4.2** Comparison of the absorption source term using variable absorption coefficient  $\kappa$  in  $\text{m}^{-1}$  with  $T=2000\text{K}$ ,  $N_r=1000$ ,  $N_{cells}=1000$  on a single MPI rank.

Tables 4.1 and 4.2 list the maximum standard deviations normalized by the average of all radiative absorptions for all computational cells and runs at each condition. Normalized standard deviations  $\sigma_{max,norm}$  are evaluated using the method described in Ref. [112], as

$$\sigma(x) = \sqrt{\frac{\sum_{i=1}^{N_s} (Q_{abs,MCRT,i}(x) - \bar{Q}_{abs,MCRT,i}(x))^2}{N_s(N_s - 1)}}, \text{ and} \quad (4.1)$$

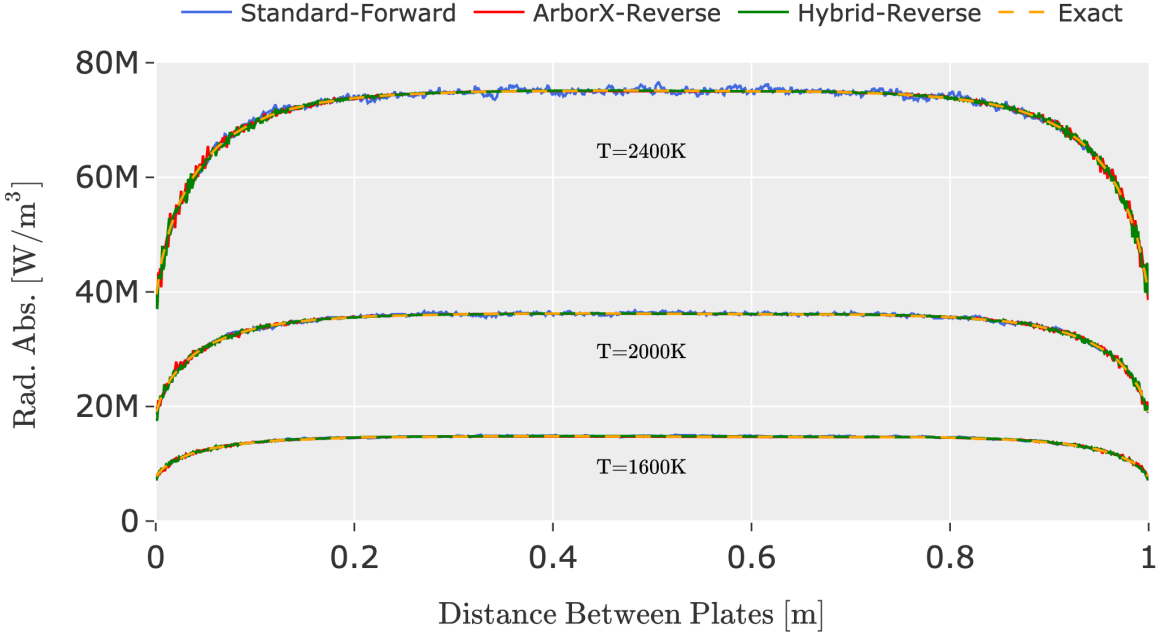


**Figure 4.3** Variable temperature with  $\kappa=10 \text{ m}^{-1}$ ,  $N_r=1000$ ,  $N_{cells}=1000$  on a single MPI rank.

$$\sigma_{max,norm} = \frac{\max_x(\sigma(x))}{\widetilde{Q}_{abs,MCRT}} , \quad (4.2)$$

where  $i$  is one of  $N_s$  samples,  $x$  is the distance between the plates, and  $\bar{\cdot}$  and  $\tilde{\cdot}$  indicate averages over the 50 sampled runs and over all radiative absorptions, respectively. Tables 4.1 and 4.2 again show good agreement with analytical solutions, with maximum normalized standard deviations of less than 5%.

In the reverse methods, a noticeable degree of noise is present near the boundaries of the medium. This is a natural occurrence in the reverse Monte Carlo method [113]. Reverse rays emitted from the center of the medium encounter identical medium composition on all sides and for approximately the same lengths. As a result, cells in this region observe minimal variance in accumulated intensities. However, near the edges, a large fraction of the rays reach the boundary instead of the medium. These rays return different intensities from those directed into the medium, resulting in an increased variance in absorption. This trend occurs in increasing magnitude for lower absorption coefficients [113]. As absorption

**Table 4.1** Maximum normalized standard deviations (using Eq. 4.2) for various MCRT results at various absorption coefficients.

Tracing Method	Abs. Coeffs. [ $\text{m}^{-1}$ ]						
	0.5	1	2	4	6	8	10
Standard-Forward	0.0079	0.0084	0.0068	0.0074	0.0079	0.0088	0.0095
ArborX-Reverse	0.046	0.038	0.032	0.027	0.026	0.024	0.025
Hybrid-Reverse	0.046	0.038	0.030	0.028	0.027	0.026	0.024

coefficient decreases, the optical distance from the center of the medium to the boundaries decreases; subsequently, decreasing absorption coefficient increases the variance towards the center of the medium. Figure 4.2 demonstrates these trends with significant magnification due to the logarithmic axis visually inflating errors for low-absorption coefficient runs.

Figures 4.2 also demonstrates the physical result of increasing absorption coefficient to the reader. It is apparent that higher absorption coefficients result in higher volumetric radiative absorption within the medium. This is evident from Beer’s law, Eq. 2.10, which shows how increasing absorption coefficient results in an increase in attenuation of ray intensity. Furthermore, higher absorption coefficients increase the radiative emission as well, per Eq. 2.23. This increases the amount of energy available to be absorbed. The net effect is a super-linear increase in radiative absorption. Between absorption coefficients of  $1 \text{ m}^{-1}$  and  $2 \text{ m}^{-1}$ , for example, peak radiative absorption increases almost three times.

Regarding the shape of the absorption profiles, towards the center of the media, larger absorption is apparent due to a higher amount of incident radiation from the emitting medium on both sides. Towards the edges, radiative absorption decreases due to the absence of radiation from the adjacent cold-black wall. Additionally, high absorption coefficients result in a flattened radiative absorption profile. This again follows from the exponential nature of Beer’s law. As absorption coefficient increases, rays are attenuated more rapidly by the medium, allowing less energy to escape to the wall.

**Table 4.2** Maximum normalized standard deviations (using Eq. 4.2) for various MCRT results at various temperatures.

Tracing Method	Temperatures [K]		
	1600	2000	2400
Standard-Forward	0.0097	0.0091	0.0091
ArborX-Reverse	0.025	0.025	0.026
Hybrid-Reverse	0.025	0.024	0.024

**Table 4.3** Average runtimes for each tracing method.

	Standard-Forward	ArborX-Reverse	Hybrid-Reverse
Runtime (s)	0.048	0.074	0.052

Likewise, when temperature is increased, as shown in Fig. 4.3, radiative absorption also increases. This follows from the increased emission due to the fourth order scaling of temperature in the black-body emission function, Eq. 2.1. An increase in temperature of 400K approximately doubles the net radiation absorbed.

Solver runtimes are presented in Table 4.3. All solutions are conducted using Intel Xeon Gold 5220 processors using the Kokkos OpenMP back-end with 72 OpenMP threads. Runtimes appeared to be independent of absorption coefficient and temperature with the exception of the Standard-Forward method where rays are terminated in the mesh when they fall below a cutoff energy. As a result, Standard-Forward saw decreasing runtime with increasing absorption coefficient. As such, presented runtimes are averaged across all cases tested except for Standard-Forward where the maximum runtime is presented. Standard-Forward is noticeably faster than ArborX-Reverse. This is likely a result of the BVH tracing procedure. For ArborX-Reverse, the BVH must be traversed once for every ray to determine the intersected cells. A BVH traversal requires more time to compute than the standard computation of determining the next cell intersected by using the exit face of the previous cell. As a result,

ArborX-Reverse requires more time to simulate within a single MPI rank. Hybrid-Reverse, however, requires a similar runtime as both Hybrid-Reverse and Standard-Forward conduct identical tracing operations when run within one MPI rank. Hybrid-Reverse, however, requires rays to propagate until exiting the domain instead of terminating upon falling below a cutoff energy. Therefore, Hybrid-Reverse does not see the trend of decreasing runtime with increasing absorption coefficient.

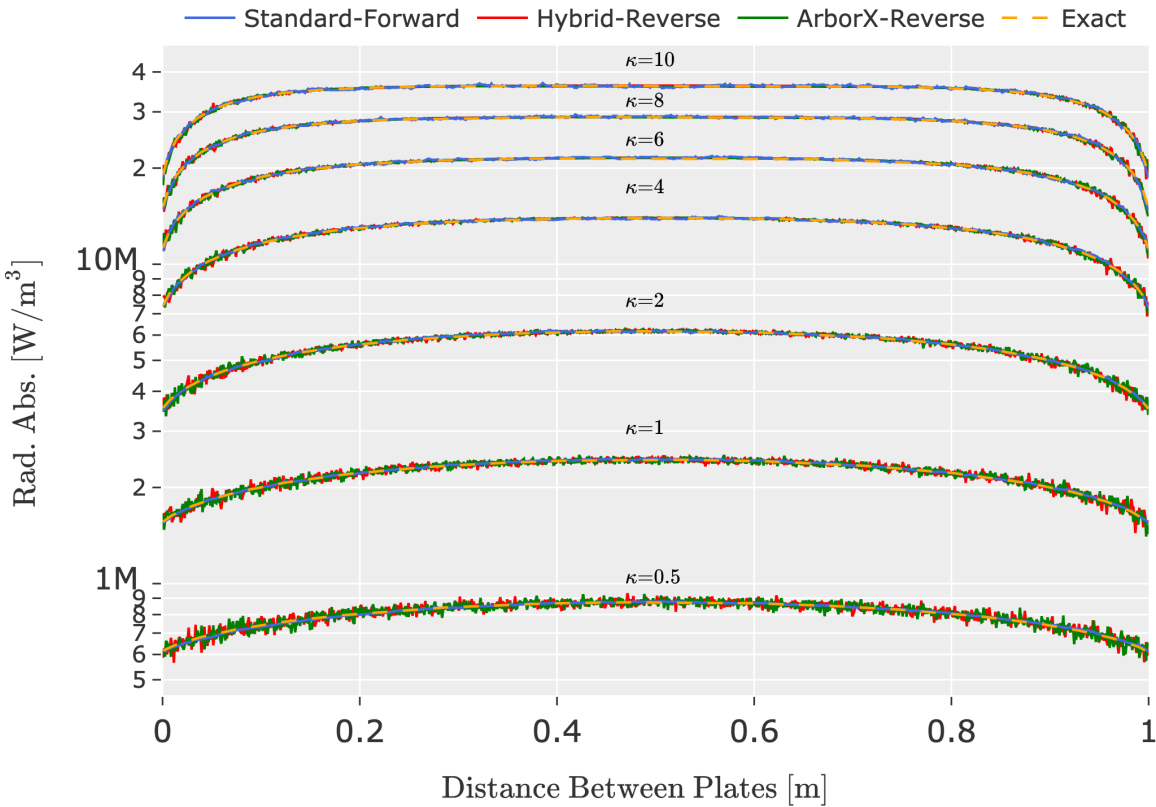


**Figure 4.4** Variable absorption coefficient  $\kappa$  in  $\text{m}^{-1}$  with  $T=2000\text{K}$ ,  $N_r=1000$ ,  $N_{cells}=1000$  with eight MPI ranks.

#### 4.1.2 Results with multiple MPI ranks

The same tracing procedures are tested on the same plane-parallel configuration with eight MPI ranks evenly spaced along the one-dimensional domain. Monte Carlo and exact solutions are compared at varying absorption coefficients and temperatures and results are presented

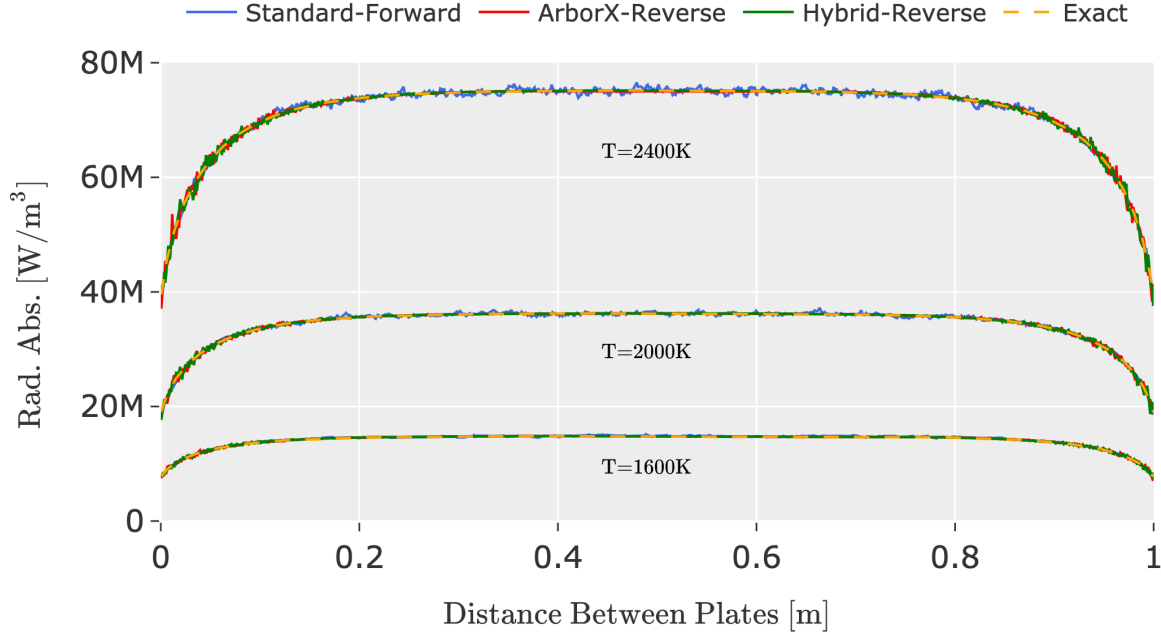


**Figure 4.5** Variable temperature with  $\kappa=10 \text{ m}^{-1}$ ,  $N_r=1000$ ,  $N_{cells}=1000$  with eight MPI ranks.

in Figs. 4.4 and 4.5. As before, results compare extremely well demonstrating the accuracy of the distributed raytracing method of section 3.2.3. Similar to the single-node results, an increase of solution noise is observed for the reverse Monte Carlo solutions at lower absorption coefficients due to the boundary effect discussed previously. Tables 4.4 and 4.5 display maximum normalized standard deviations for all MPI runs. As before, standard deviations are greater in the reverse Monte Carlo results than in the Standard-Forward results. Finally, overall-averaged runtimes are presented in Table 4.6 for each of the solvers. For these results, ArborX-Reverse exhibits greater performance compared to Standard-Forward and Hybrid-Reverse.

### 4.1.3 Results with varying ray counts

Finally, Fig. 4.6 presents the radiative absorption profile for different ray counts. Only Standard-Forward results are presented in this figure to demonstrate the general effect of

**Table 4.4** Maximum normalized standard deviations (using Eq. 4.2) for various MCRT results at various absorption coefficients for with eight MPI-ranks.

Tracing Method	Abs. Coeffs. [m <sup>-1</sup> ]						
	0.5	1	2	4	6	8	10
Standard-Forward	0.0090	0.0066	0.0067	0.0070	0.0085	0.0089	0.0096
ArborX-Reverse	0.0439	0.0375	0.0348	0.0306	0.0309	0.0265	0.0239
Hybrid-Reverse	0.0439	0.0381	0.0345	0.0290	0.0262	0.0248	0.0231

**Table 4.5** Maximum normalized standard deviations (using Eq. 4.2) for various MCRT results at various temperatures with eight MPI ranks.

Tracing Method	Temperatures [K]		
	1600	2000	2400
Standard-Forward	0.0097	0.0091	0.0091
ArborX-Reverse	0.025	0.025	0.026
Hybrid-Reverse	0.025	0.024	0.024

**Table 4.6** Average runtimes for each tracing method.

	Standard-Forward	ArborX-Reverse	Hybrid-Reverse
Runtime (s)	1.25	1.10	1.21

**Table 4.7** Standard deviations of the percent difference of MCRT and exact solution at various absorption coefficients. Each simulation is run with 1000 computational cells, a temperature of 2000K, and absorption coefficient of  $10\text{m}^{-1}$

Rays emitted per cell	10	100	1000
Eq. 4.2	4.83	1.47	0.52
Ratio of standard deviations	$\frac{1.47}{4.83} = 0.30$	$\frac{0.52}{1.47} = 0.35$	

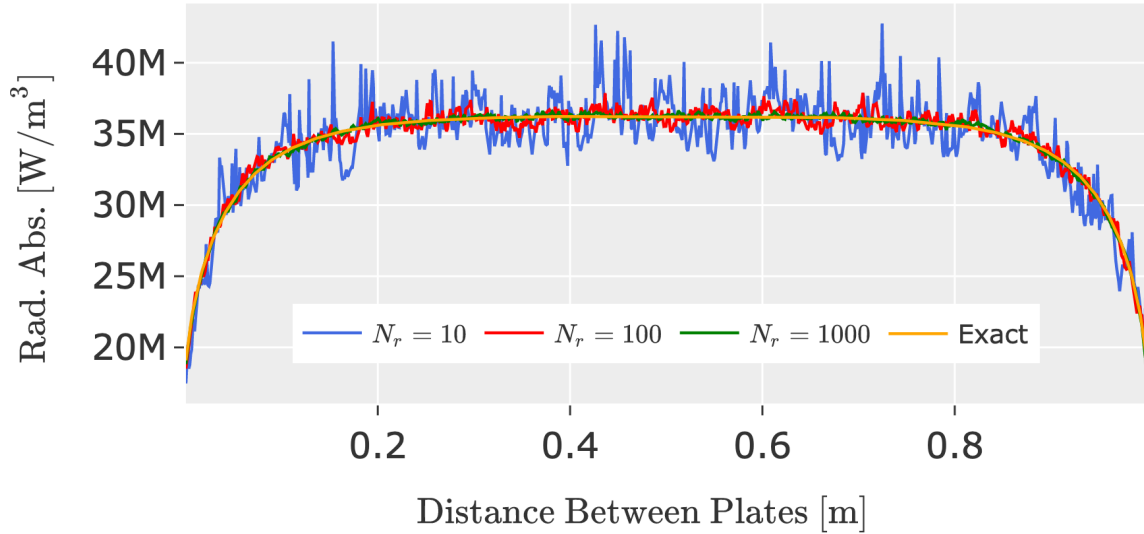


**Figure 4.6** Variable number of rays emitted per cell ( $N_r$ ) with  $\kappa=10\text{ m}^{-1}$ ,  $T=2000\text{K}$ ,  $N_{cells}=1000$ .

ray count on solution variance. Absorption coefficients and temperatures are held constant at  $10\text{ m}^{-1}$  and 2000 K. Increasing ray counts result in decrease of stochastic noise in the solution. Table 4.7 displays maximum standard deviations for each of the three tests. As the number of rays increases, the variability decreases and the solution approaches the exact. As per Modest and Mazumder [112], the standard deviation should be proportional to  $1/N_r^{1/2}$  for  $N_r$  rays. This would mean an increase of ray count by one order of magnitude should decrease standard deviation by a factor of  $\frac{1}{\sqrt{10}} = 0.32$ . Table 4.7 shows that this trend is closely followed by showing the ratio of the maximum standard deviation of higher ray counts to that of lower ray counts.

## 4.2 Backward-Facing Step Combustor

The backward-facing step (BFS) combustor is another simple, repeatable geometry that is used for a variety of case studies in fluid dynamics. The BFS geometry is presented in Fig. 4.7 and is based on an experimental configuration at the Pennsylvania State University. Fluid enters through the inlet and flows over the step towards the outlet. When the gas moves past the step, it forms a large a recirculation zone, which mimics similar fluid dynamic phenomenon within a real combustor.

The interaction between the fluid and the boundaries, the characteristics of turbulent fluctuations, and the resulting mean velocities profiles are all topics of interest when studying backward-facing steps. Numerous examples exist demonstrating its use for experimental and numerical investigations of turbulent fluid flow [114, 115, 116, 117]. Most computational studies in literature are conducted with non-reacting, isothermal conditions. In contrast, studies of combined turbulent and high temperature flow [118, 119], and reacting flows [120] over backward-facing steps have been modeled significantly less frequently. In the relatively few studies that exist, the addition of volumetric heating and composition changes resulting from the exothermic chemical reactions have been shown to influence the flow patterns and turbulence intensity of the fluid [120].

Recent work related to the present radiation solver has focused on quantifying the relative contribution of radiative to convective heat transfer on the boundaries of reacting backward-facing step systems [121]. To that end, a combined experimental and modeling collaboration is underway between the Pennsylvania State University and the University of Connecticut to study this. In the future, results from the Penn-State experimental rig will be compared to computational results obtained using the present radiation solver to better understand the heat transfer mechanism. For this thesis, the same geometry is used to demonstrate the accuracy and efficiency of the radiation solver within a research-relevant geometry.

First, a description of the case setup is provided. Next, results from the Standard-

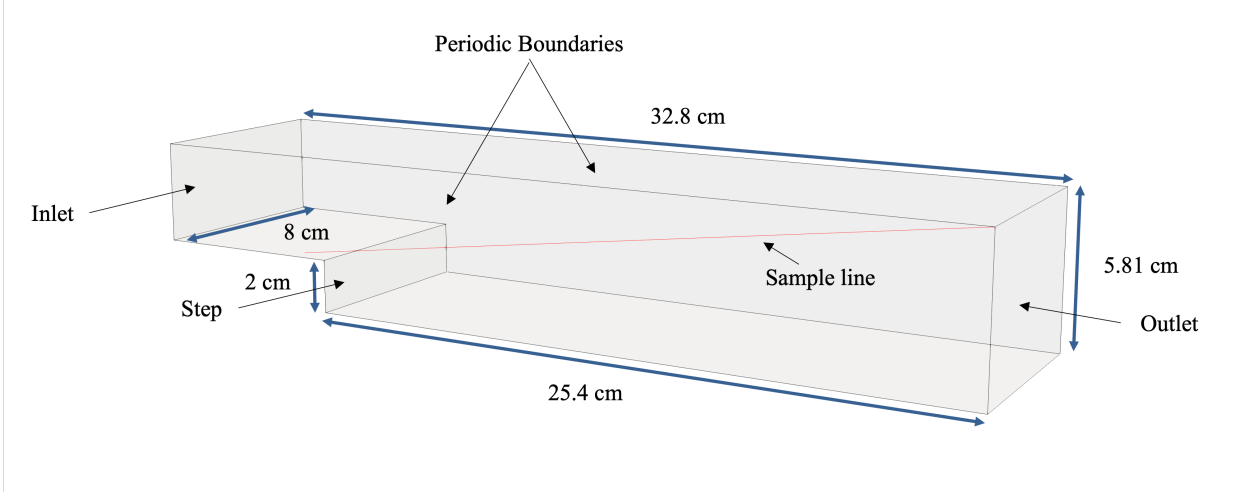


**Figure 4.7** Dimensions of backward-facing step configuration used in this study in addition to a representative line used to sample radiative properties. The sampled line connects the farthest two corners of the bounding box around the domain.

Forward implementation are compared against those of an established Fortran code. Results are obtained using the Standard-Forward solver because it is the most robust solver at the present stage of development. Then, a description of the influences of radiation in the fluid and along the walls is provided. Finally, solver runtimes are presented and compared.

#### 4.2.1 Case setup

The simulation domain is identical to that of a previous study [122]. The geometry is 33 centimeters long between the inlet and the outlet and 8 centimeters in width. The mesh consists of 7,411,200 hexahedral cells of increasing refinement at the recirculation zone and the walls. For this case, no chemically reacting flow is included. The flow is present in vitiated form, where a chemical reaction is initiated in a region upstream of the step, and the resulting "dirty" air with high CO<sub>2</sub> and H<sub>2</sub>O content is diluted with quiescent air before entering the domain. All subsequent chemical reactions are neglected beyond the simulation inlet, resulting in a purely fluid-mechanic and heat-transfer calculation within the simulation domain. Furthermore, the present simulation does not contain any chemical composition data, so accurate absorption coefficients cannot be calculated. Therefore, the

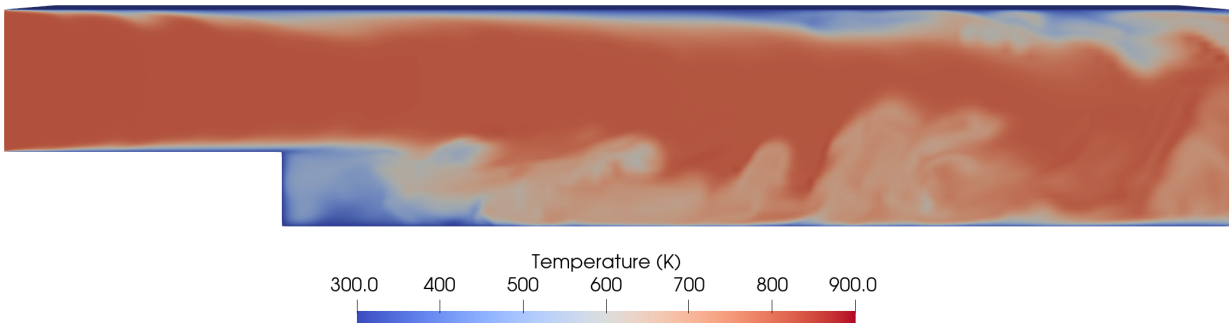
absorption coefficient is assumed to be a uniform value of  $0.5 \text{ m}^{-1}$ . The mixture reaches the main section at a temperature of up to 850K, appreciably lower than expected temperatures of above 1600K when full reactions are present. Pressure is atmospheric, and inlet velocities are approximately 10 m/s. The simulations are conducted using the conjugate heat transfer solver `multiRegionReactingFoam`, which is a compressible solver that accounts for energy transport. The region boundaries are all treated as cold, black boundaries with the exception of the sidewalls that are treated as symmetric planes.

#### 4.2.2 Results

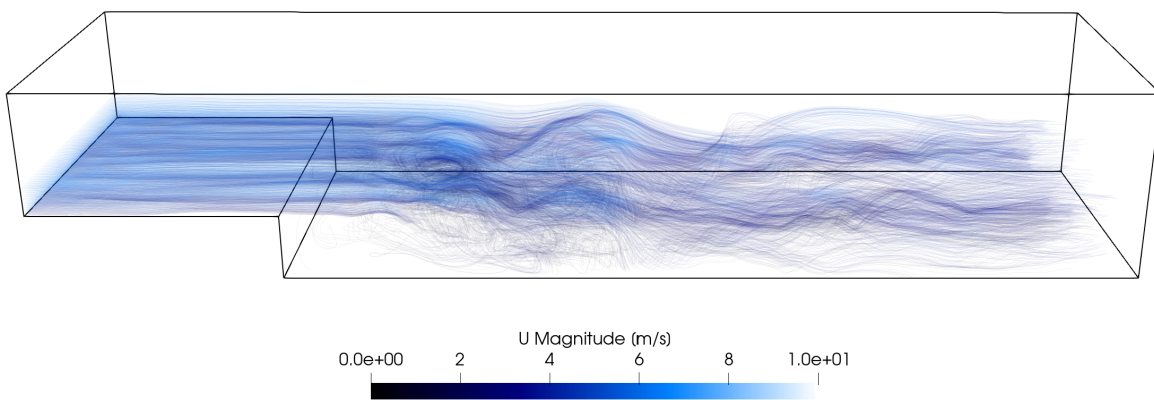
A single time-step of the CFD simulation after 1.094 seconds of physical time was extracted for a frozen field analysis. Ten rays are emitted for each computational cell. Figures 4.8a, 4.8b show temperature contours and velocity streamlines at the frozen timestep in the simulation. The vitiated flow is shown to partially whirl downward and recirculate behind the step. At this point, the mostly laminar entry gas quickly becomes turbulent and chaotic.

The resulting radiative emission and wall-heat flux iso-contours from the MCRT solver are shown in Fig. 4.9. A small degree of emission is present in the re-circulation zone behind the step. In contrast, the high temperature bulk flow that moves downward halfway aft through the geometry appears to be emitting more significantly. Radiation is emitted from the flow and decreases the thermal energy contained in the passing fluid. The fluid is then quickly replaced by the new gas at the entrance, which results in a continuous load of radiation incident on the bottom surface of the domain.

Figures 4.10a, and 4.10b show the radiative absorption, emission, and net energy source along the line shown in Fig. 4.7 using the different solvers for comparison. The radiative participation peaks towards the center section of the geometry. Peak absorption quantities are extremely low under these conditions due to the low temperatures and absorption coefficient. Results from the Standard-Forward implementation compare well to the well-



(a) BFS temperature contour along the mid-plane after 1.094 seconds of physical time in the simulation.



(b) Streamlines traced from the entrance of the BFS.

**Figure 4.8** Temperature isocontour of the cross-section(a) and instantaneous streamlines (b) obtained using the `multiRegionReactingFoam` solver.

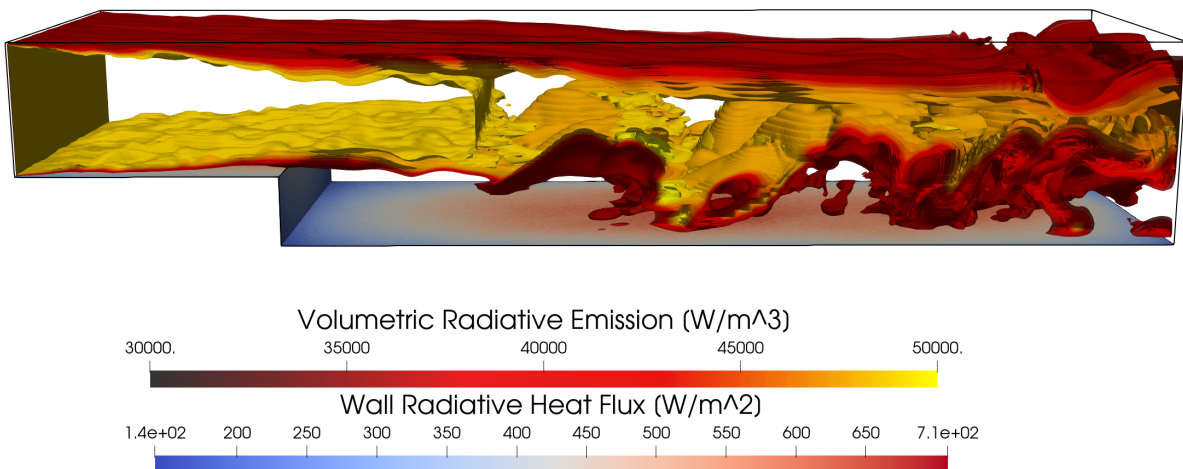


**Figure 4.9** Isocontours of volumetric radiative emission alongside resulting radiative heat flux at the walls.

**Table 4.8** BFS runtime comparisons with 1 ray emitted per computational cell.

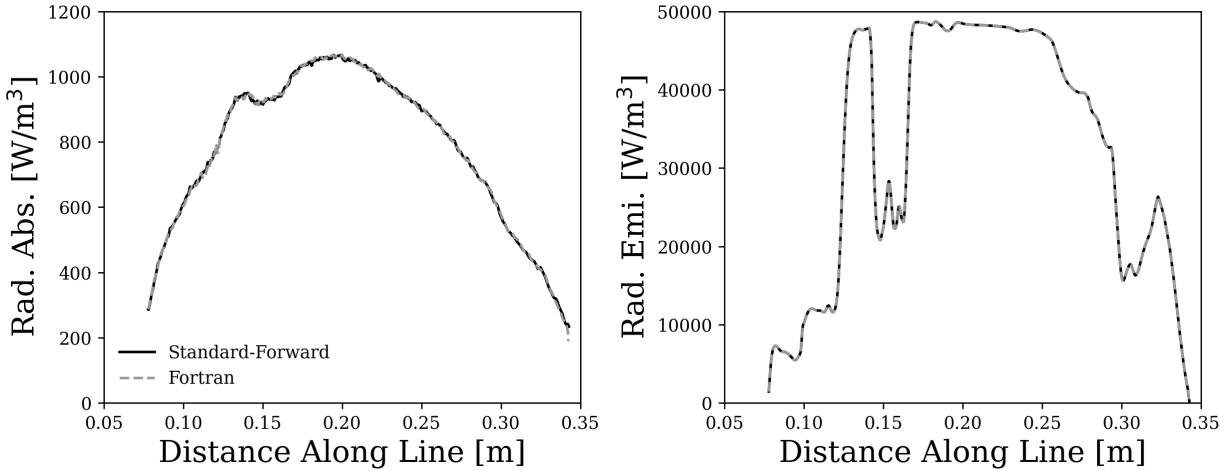
	Serial	128 OpenMP threads	V100 GPU	A100 GPU
Fortran	777.6 s	N/A	N/A	N/A
Standard-Forward	726.2 s	38.2 s	8.0 s	4.3 s

established Fortran implementation. Oscillations are present in the absorption from both solvers because absorption is determined using a stochastic tracing procedure. Oscillations are not present in the emission profiles because emission is calculated directly using Eq. 2.22. The radiation source (absorption–emission) does not show oscillations because the magnitude of the emission component is significantly higher than the magnitude of the oscillating absorption component.

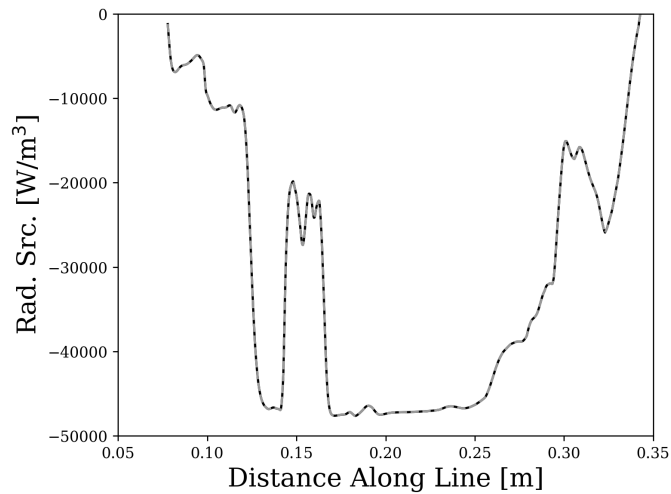
### 4.2.3 Model Performance

Simulation runtimes are presented for the Standard-Forward and Fortran-based solvers. Simulations were performed on the single time-step using 1 ray per cell and 10 rays per cell for all solvers, and serial, OpenMP and Cuda were tested as Kokkos backends for the new MCRT solver. Simulations were performed using a single 64-core AMD EPYC 7713 CPU node for all CPU-parallel computations, and GPU calculations were performed using NVIDIA V100 and NVIDIA A100 GPUs from the high performance computer Hornet at the University of Connecticut with GPU tasks deployed from a host AMD EPYC 7452 CPU.

Results are listed in tables 4.8 and 4.9 for 1 ray emitted per cell and 10 rays per cell, respectively. The performance of the Standard-Forward model is comparable to the Fortran code model for a serial calculation. A runtime improvement of 31% is observed before any parallel routines have been applied due to the improved mesh-transfer method implemented in the new MCRT methods. Almost no mesh data is duplicated during the mesh transfer process, allowing for minimal delay before the raytracing procedure begins.



(a) Volumetric radiative absorption and radiative emission sampled along the line present in Fig. 4.7.



(b) Volumetric radiative source term (absorption - emission). Same legend as in Fig. 4.10a.

**Figure 4.10** MCRT solution results between the present MCRT solver and a well-established Fortran solver of the present backward-facing step after 1.094 seconds of physical time.

**Table 4.9** BFS runtime comparisons with 10 rays emitted per CFD cell.

	Serial	128 OpenMP threads	V100 GPU	A100 GPU
Fortran	7421.7 s	N/A	N/A	N/A
Standard-Forward	6867.8 s	402.7 s	55.4 s	23.7 s

The introduction of a parallel back-end results in dramatic speedups. With 128 OpenMP processes, the Standard-Forward method reduces runtime by 19 times over serial and 20 times over the Fortran-based code with one ray emitted per computational cell. The usage of a GPU enabled an even greater reduction in runtime. Speedups of 169 and 290 are observed when using the A100 GPUs for the 1 ray per cell case and 10 rays per cell case, respectively.

## 4.3 Direct Numerical Simulation of a Turbulent Pool Fire

With successful validation of the solver under 1-D and 3-D configurations, the solver is then tested on a non-gray direct numerical simulation of a turbulent pool flame. The pool flame is a canonical configuration used in the field of fire research as a surrogate for many hazardous combustion scenarios [43]. The flame is a non-premixed turbulent diffusion flame where fuel is supplied through the inlet on the bottom face and buoyant forces drive the high-temperature, reacting flame to rise up and puff periodically. Furthermore, the high temperatures from the chemical reaction alongside the larger length scales provide high radiative emissions with higher optical thickness compared to laboratory jet flames such as the Sandia D flame [123]. For the present study, the configuration is tested first using the Monte Carlo code using a line-by-line non-gray model with various hardware back-ends. Next, a gray model is used in the MCRT solver to allow for a fair comparison against existing finite volume Discrete Ordinates Method (fvDOM) and P-1 models embedded in `OpenFOAM`.

### 4.3.1 Case Setup

The simulation geometry, mesh, and case conditions are identical to those of Ref. [3] where the Fortran based Monte Carlo ray tracing solver was applied with a line-by-line non-gray model [109] for a DNS. The original simulation was conducted using an in-house `reactingDFoam` solver within `OpenFOAM` [124] and consisted of an n-heptane/air non-premixed

turbulent flame. The geometry is presented in Fig. 4.11. The mesh resolution is 9.6 million hexahedral cells in a cylindrical domain of diameter 0.781 m and height 0.600 m. The pool is centered and has a diameter of 7.1 cm. The grid resolution is approximately 1 mm in the axial direction and 0.5 mm in the radial direction with additional refinement around the pool location. The Kolmogrov scale is approximately 0.5 mm, which is considered resolved in this study, and subgrid modeling is not included in the original simulation. The flame itself is a highly sooting flame with a radiant fraction of 29% [3].

The present study solves radiation for a single snapshot at exactly 1.25 s of physical time. Time is frozen, and the ray-tracing procedure is conducted within a static field. The adaptive radiative emission model is used where the number of rays emitted from a cell scales proportionally with the cell's radiative emissive power [84], as per section 3.2.1. This resulted in a total of 103,907,333 rays emitted, with most emission occurring from within the flame. Twenty solutions to the radiation transport equation are evaluated using MCRT and averaged over to obtain mean solver runtimes. Non-gray CO<sub>2</sub>, H<sub>2</sub>O, CO, and soot are

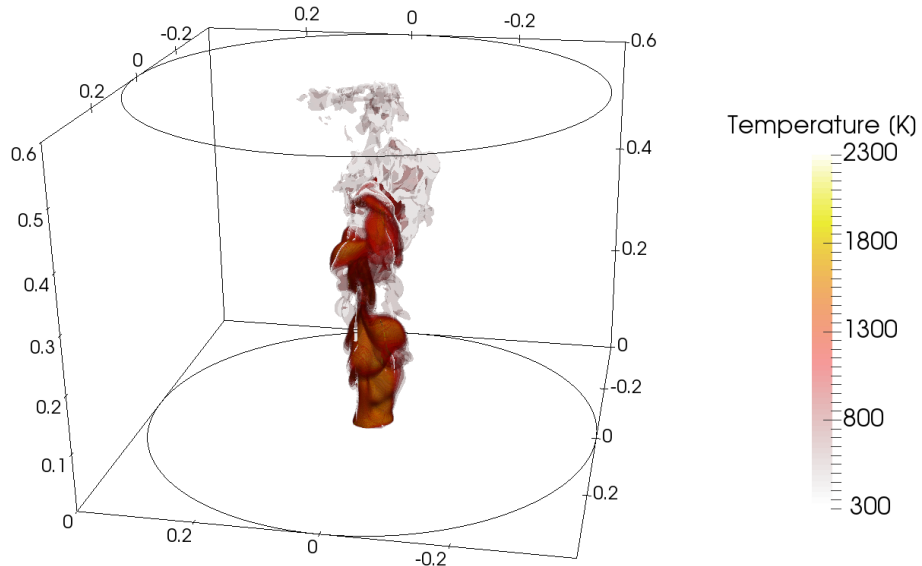


**Figure 4.11** Instantaneous temperature isocontour from the turbulent pool fire used for runtime analysis in this study. The dimension of the geometry is also illustrated.

modeled using a line-by-line model of Ref. [109].

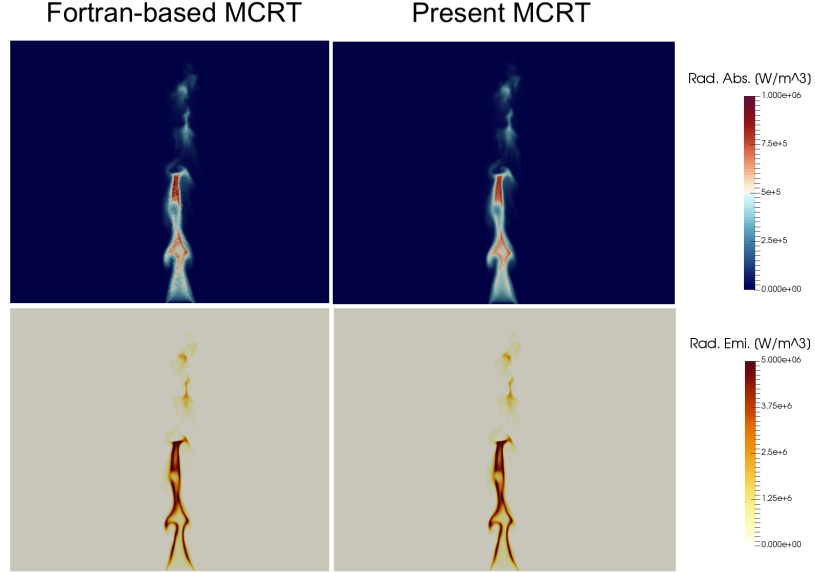


**Figure 4.12** Mid-plane contours of radiative emissive power and radiative absorption from the Fortran-based solver used in Ref. [3] and the present solver.

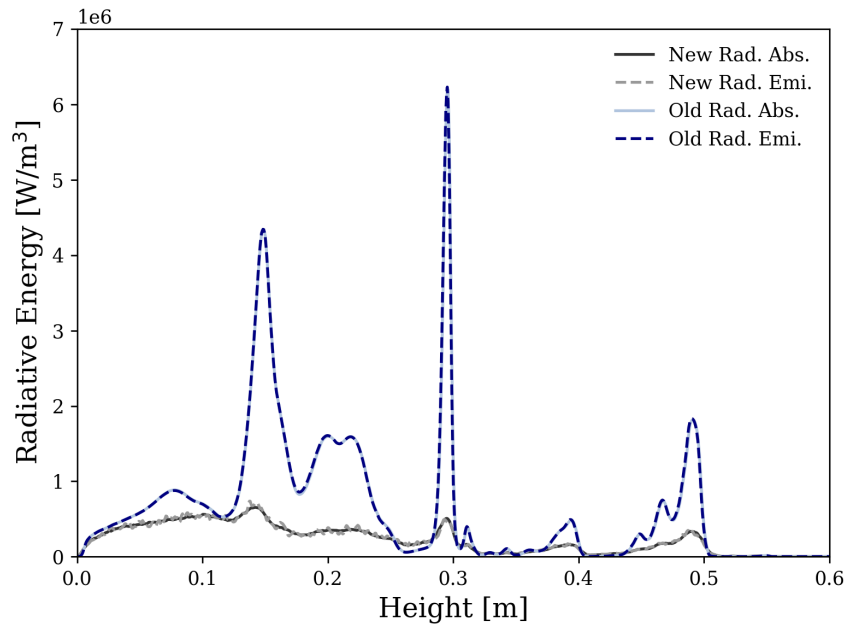


**Figure 4.13** Centerline radiation source term with line-by-line non-gray radiation from the present MCRT solver and the Fortran-based MCRT solver.

### 4.3.2 Verification and Performance of line-by-line MCRT

To verify the new radiation solver with the line-by-line database, Fig. 4.12 visually compares the radiative emissive power and radiative absorption across the centerplane between the new MCRT solver and the previous one used in Ref. [3]. One ray per cell was emitted for each computational cell in Ref. [3] and radiation was solved on the fly in that study. Identical line-by-line tables are employed in both studies. Figure 4.13 further presents a more quantitative comparison along the centerline of the pool. The agreement in both the emission and absorption source terms is excellent, with more fluctuations in the absorption source observed from previous results because fewer rays were used in that study.

Radiation execution times are presented in Table 4.10 for various `Kokkos` back-ends. No changes to the radiation code are made across the various hardwares tested. Both CPU and GPU parallelism display a significant speedup over serial CPU calculations. The NVIDIA A100 GPU requires approximately 1/400<sup>th</sup> of the computational time to simulate an equivalent radiation problem as one CPU thread running in serial. Likewise, the V100 also shows speedups greater than two orders of magnitude. Interestingly, the NVIDIA A100, released in 2020, shows a greater than two times speedup over the NVIDIA V100, released in 2017. Meanwhile, OpenMP with the AMD Epyc 7713 CPU shows speedups an order of magnitude faster than serial and an order of magnitude slower than the A100 GPU.

Run-times are also presented with MPI enabled on 2 ranks, both MPI ranks are present in the aft direction. The two MPI ranks are situated on separate computing nodes with different NVIDIA A100 GPUs. Run-time decreases because of the greater resources present. The decrease is limited, however, because of the additional MPI communication overhead incurred. Future work will integrate the Hybrid-Reverse algorithm in this configuration to improve multi-rank scalability.

**Table 4.10** Comparison of MCRT runtimes with line-by-line radiation for a single snapshot of a DNS of a turbulent pool-fire.

	A100 GPU	V100 GPU	OpenMP	Serial	A100/2ranks
Runtime	117.9 s	278.0 s	1333.3 s	44844.5 s	102.2 s
Speedup over serial	380	161	34	1	439
Speedup over OpenMP	11	5	1	0.03	13

### 4.3.3 Comparison with other radiation solvers using a gray model

The pool-fire simulation is then employed to compare the new MCRT solver with other popular solvers including the fvDOM solver and P-1 solver from `OpenFOAM-5.x`. A constant absorption coefficient of  $0.5 \text{ 1/m}$  is prescribed to each computational cell in the same snapshot to maintain identical spectral models between all solvers. Adaptive emission is turned on for the MCRT method resulting in 101,000,825 total rays. The fvDOM solutions were obtained using `OpenFOAM` default settings, but with 16 azimuthal discretizations and 4 polar discretizations. Each fvDOM solution required 50 iterations to converge to final residuals of  $O(10^{-5})$ , and 20 fvDOM solutions were obtained for runtime averaging. Twenty P-1 solutions were also obtained for runtime averaging using `OpenFOAM` default settings.

A comparison of solutions within the gray medium are presented in Fig. 4.14. MCRT and fvDOM show comparable profiles. The P-1 solution shows significant deviation of radiative absorption in both magnitude and shape from the more-accurate MCRT and fvDOM solutions.

Solver runtimes are presented in Table 4.11. The GPU accelerated MCRT solver is again shown to improve solver performance significantly over both the serial and OpenMP versions. Moreover, the GPU solution is shown to be faster than fvDOM and, interestingly, the P-1 serial calculations. This indicates that such a GPU-accelerated MCRT solver has great potential to replace some reduced-order solvers and be applied on the fly in combustion simulations.

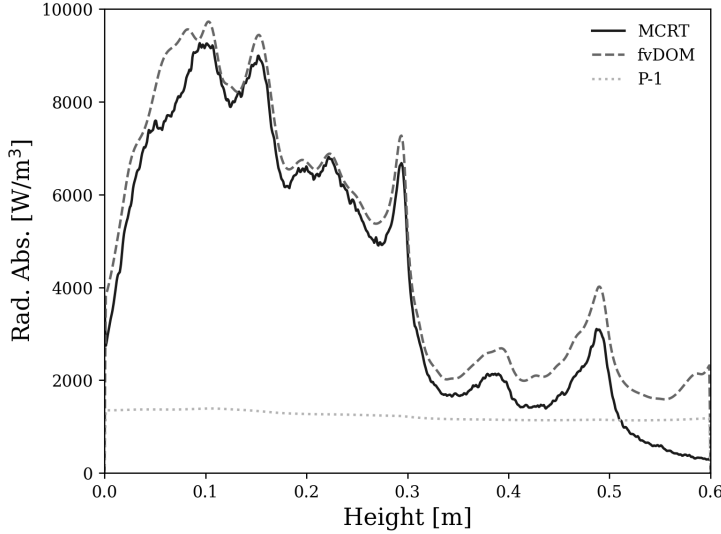


**Figure 4.14** Centerline radiative absorption with gray radiation from the present MCRT solver and the OpenFOAM fvDOM and P-1 radiation solvers.

**Table 4.11** Comparison of MCRT runtimes of gray radiation within a single-snapshot of a DNS of a turbulent pool-fire.

	MCRT			OpenFOAM	
	A100 GPU	OpenMP	Serial	fvDOM serial	P-1 serial
Runtime (s)	74.3 s	1070.4 s	33262.5 s	4426.3 s	112.5 s
Speedup over fvDOM	60	4	0.13	1	39
Speedup over P-1	1.5	0.1	0.003	0.03	1

## 4.4 Transient Small Pool Fire

Finally, the solver is applied to a transient turbulent pool-fire, to demonstrate its feasibility of coupling with CFD applications. Similar to the study of section 4.3, the domain consists of turbulent non-premixed flame fueled by a circular fuel source along the bottom face. However, unlike the previous study, radiation is fully coupled to fluid dynamics from its initial conditions, and radiation quantities are directly extracted from the simulation.

#### 4.4.1 Case Setup

The simulation is based on a `OpenFOAM-5.x` tutorial case, `smallPoolFlame3D`, where mesh refinement has been doubled and the default discrete-ordinates radiation model has been deactivated. In the tutorial case, a mass-source is provided through the inlet at the bottom of the domain, where a reaction is also initiated. A turbulent non-premixed flame is then simulated with infinitely-fast chemistry for four seconds of physical time. Both a frozen-field analysis on a single-timestep and a full transient simulation are conducted and analysed. The single-timestep analysis is conducted using the original `smallPoolFlame3D fireFoam` tutorial case, but with radiation turned off, and the timestep is obtained at 0.8s of physical time and is shown in Fig. 4.15.

The geometry is a cubic  $1 \times 1 \times 1$ m domain with a grid consisting of 1,728,000 hexahedral cells with 120 divisions per side. The size of the pool fire is much larger than the pool fire presented in section 4.3 and is not feasible to be modeled by DNS. This configuration is studied for both planck-mean gray and line-by-line spectral models, and no turbulence-radiation interaction (TRI) is accounted for in this study.

#### 4.4.2 Results

Figure 4.16 displays the radiative emission and wall absorption patterns for the flame. Wall heat flux is maximized near the inlet section, directly adjacent to the location of ignition. The radiative emission contours drop towards the outer edges and top section of the mushroom-like shape. The turbulent mixing of the reacting flow with surrounding quiescent fluid results in a reduction in temperature and decreased volumetric emission.

##### Transient simulation

The pool-fire is simulated from initial conditions until 4 seconds of physical time. The simulation is run with line-by-line accurate non-gray emission, and radiation source terms

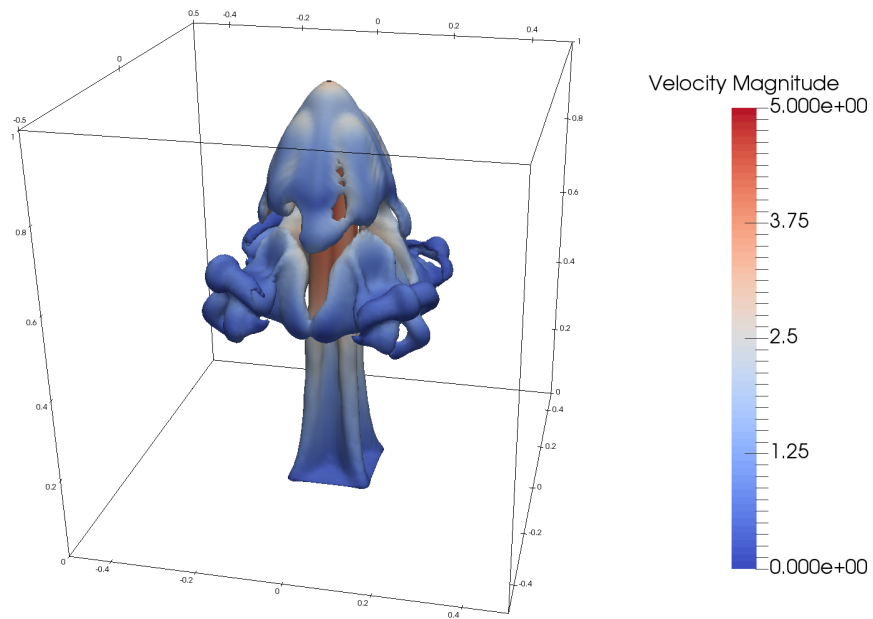


**Figure 4.15** An early timestep of the pool fire flame simulation. Isosurface is 0.03 CO<sub>2</sub> mass fraction colored by velocity magnitude in meters per second. Axes dimensions are in meters.

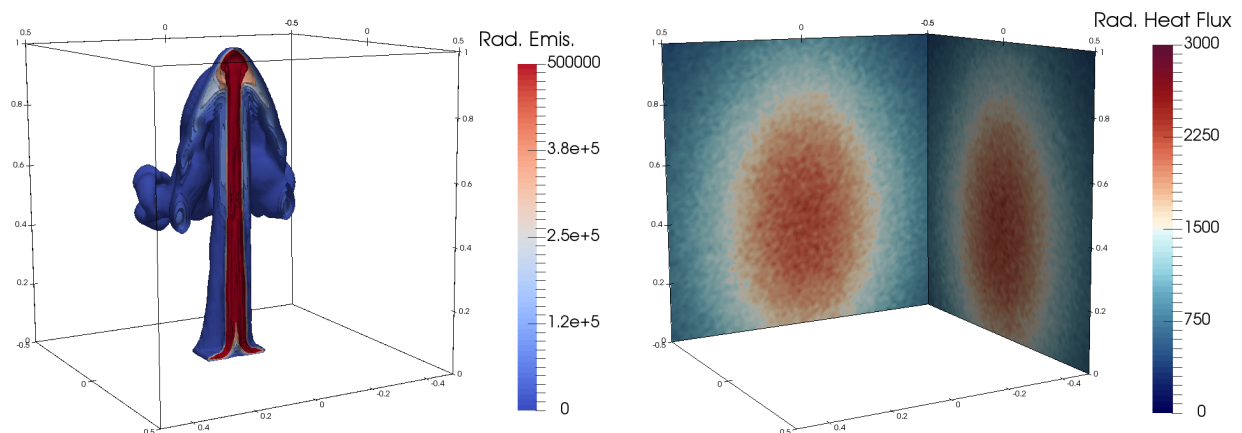


**Figure 4.16** Isosurface of 0.03 CO<sub>2</sub> mass fraction colored by radiative emission. Wall coloring represents wall radiative heat flux.

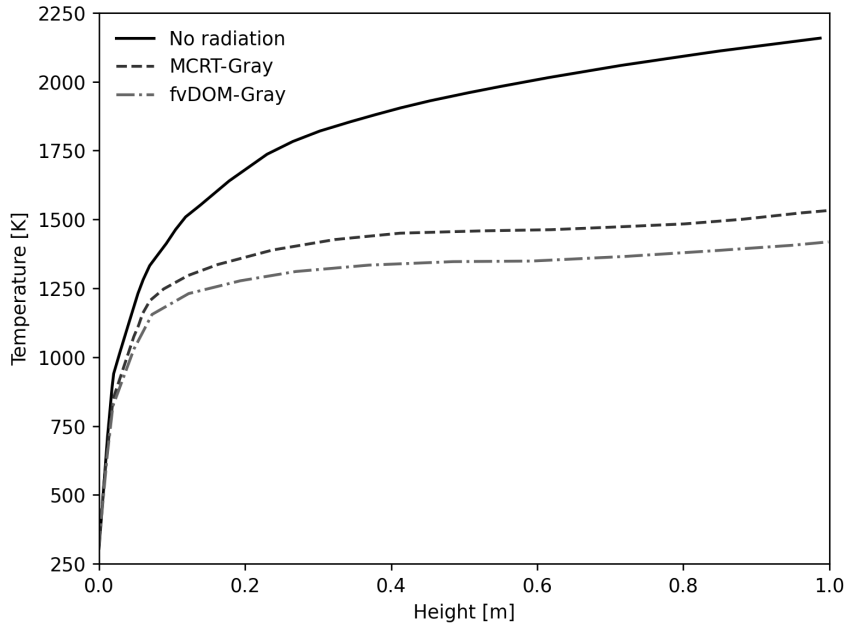


**Figure 4.17** Comparison of center-line temperature profiles of various simulations of the pool fire.

are updated each simulation time-step. Chemistry is infinitely-fast, and the case setup is identical to that of the frozen-field analysis. The pool fire first appears as a mushroom near inlet, then the reacting, billowing cloud rises upwards, and finally exits through the top boundary of the domain. The pool fire periodically fluctuates according to a *puffing period*. These oscillations are buoyancy driven and result in turbulent eddies and substantial cooling of the flame as it mixes with the oxidizer.

Radiation contributes significantly to the reduction of flame temperature, and therefore has a significant effect on the density-driven buoyant forces fluctuating the flame profile. Figure 4.17 compares the center-line temperature of the pool fire for a simulation without radiation, with the gray OpenFOAM-5.x DOM radiation solver, and the gray MCRT model. Significant variations in temperature are apparent, up to 600K at locations far from the inlet.

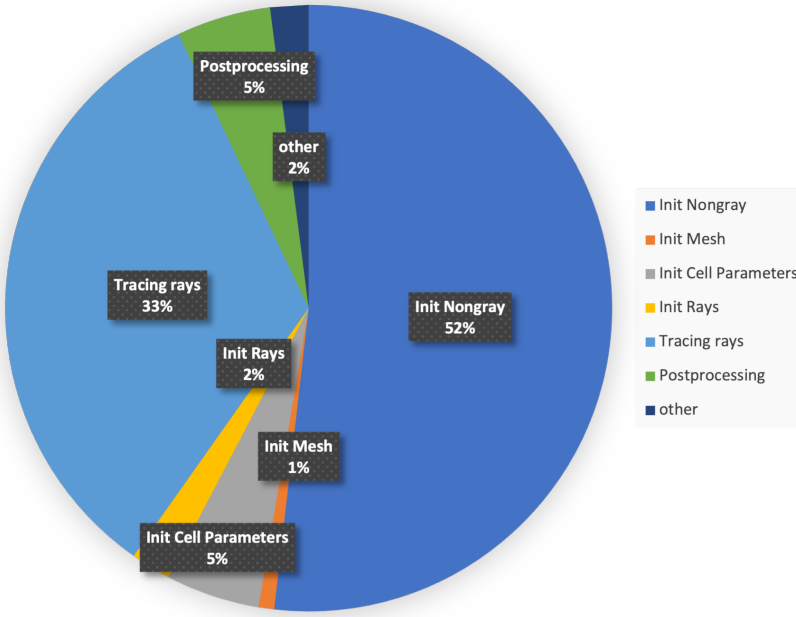


**Figure 4.18** Profiling results for the GPU

#### 4.4.3 Profiling

##### Single time-step

The run-times of various sections of the radiation solver are presented in Figs. 4.18 and 4.19 for both CPU and GPU simulations. Simulations are conducted with adaptive emission resulting in a total of 3,429,003 rays. CPU ray-tracing is completed using 30 CPU processes.

For both CPU and GPU simulations, the runtime is dominated by the loading of the non-gray database, which is over a gigabyte in size. The tracing region is proportionally smaller on the GPU as a result of the significant speedup when conducting raytracing in a SIMD-favorable architecture. The loading process consists of first loading the data into memory, initializing the representative data structures, conducting various sanity checks on the database to ensure proper loading, and deep copying the data onto the GPU, if present. Numerical time-step comparisons are present in Table 4.12.

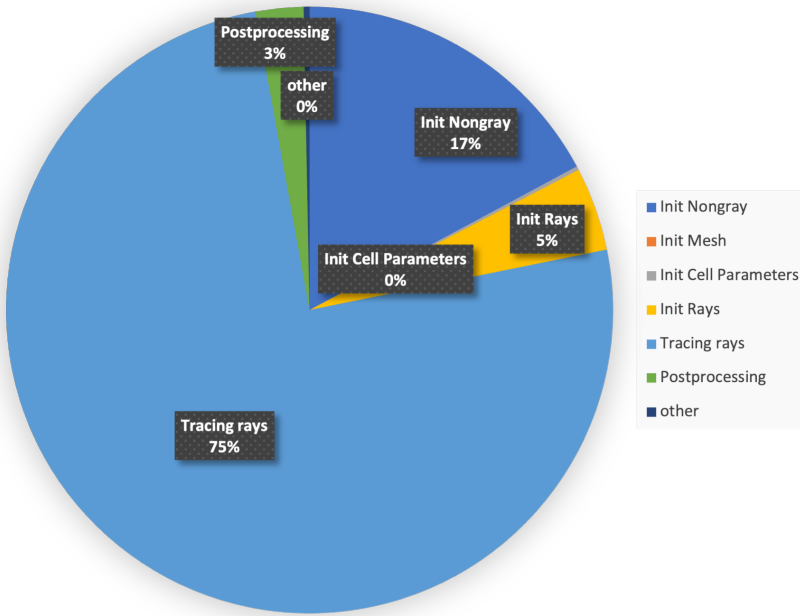


**Figure 4.19** Profiling results for the CPU.

**Table 4.12** Single time-step runtime profiling.

Parallel Variation	Init non-gray	Tracing rays	Init cell parameters	Total
30 CPU processors	0.997s	4.38s	0.0119s	5.81s
V100 GPU	2.25s	1.44s	0.218s	4.34s

### Transient simulation

Transient simulations are conducted with adaptive emission, totaling approximately 3,400,000 rays emitted and traced per time-step. Both CPU and GPU versions were run for four seconds of simulation time. Mean and standard deviations of run-times are presented in table 4.13.

For the CPU-run case, radiation encompassed approximately 37% of the runtime for each timestep, on average. It should be noted that both the non-gray database and CFD mesh are re-initialized every time step, resulting in significantly increased run-time. Future

**Table 4.13** Mean runtime contribution of radiation per timestep compared to total runtime. Standard deviations are presented in parentheses. List CPU runtimes consist of radiation parallelized on 30 CPU processors, and CFD calculation occurring on 1 processor. GPU runtimes consist of radiation running on the GPU and CFD calculated using 1 CPU processor.

Parallel Variation	Radiation Execution	Total Execution	Percent contribution
30 CPU processors	8.1s( $\pm 0.58$ s)	21.7s( $\pm 0.84$ s)	37.4%( $\pm 2.10$ %)
V100 GPU	4.7s( $\pm 0.28$ s)	16.2s( $\pm 2.21$ )s	29.4%( $\pm 2.30$ %)
A100 GPU	3.5s( $\pm 0.10$ )	14.1s( $\pm 0.16$ )s	24.8%( $\pm 0.70$ %)

work will include initializing these components at the beginning of the simulation to prevent unnecessary overhead. After these changes, it is projected that the overall radiation runtime targets approximately 6.7 s, or 33% of the total runtime. Similarly, the projected GPU runtime targets at 3.1 s, or 21% of the total runtime per timestep.

# Chapter Five

## Conclusions and future work

### 5.1 Summary of findings

The Monte Carlo method is broadly known to be the most accurate, robust, but also one of the most computationally expensive radiation models. However, with rapid development of computing hardwares, it has been used more frequently and recognized to be a promising alternative for coupled combustion simulations in the future. The fundamentals of MCRT, including the random number relations of point of emission, direction and wavenumber for forward Monte Carlo ray tracing is discussed in detail in this thesis. A description of the tracing procedure through the mesh and to the boundaries is provided. Several alternative mathematical techniques, as well as re-formulations of the Monte Carlo ray tracing method are presented, along with their various advantages.

Inspired by the recent development of computer graphics, including the usage of Graphics Processing Unit (GPU) and the algorithm of Bounding Volume Hierarchy (BVH), previous literature is reviewed on applications of these methods to ray tracing. It is found that the few studies that have applied GPUs to MCRT for thermal radiation modeling observed tremendous runtime reductions, and that no existing studies have leveraged the BVH algorithm in

the calculation of a radiatively participating medium.

Based on these understandings, a MCRT-based radiation solver is constructed using both GPUs and BVHs, for a robust tracing procedure through an unstructured polyhedral mesh. A high fidelity line-by-line spectral model is also incorporated to allow for accurate non-gray modeling. The solver is integrated with the OpenFOAM CFD software package, which enables its use with coupled, transient combustion simulations through a source term contribution to the energy equation. Additionally, the Kokkos programming model and ArborX geometric search library are used for interchangeable GPU/CPU compatibility and scalable BVH implementation, respectively. Three primary ray tracing implementations are presented: Standard-Forward, ArborX-Reverse, and Hybrid-Reverse. Each offers a different approach to ray tracing, utilizing standard forward ray tracing, BVH-based reverse ray tracing, and a combination of both, respectively. A novel distributed ray tracing procedure, where rays are emitted and traced across multiple MPI ranks simultaneously, is presented for use with both ArborX-Reverse and Hybrid-Reverse to improve performance in high performance computing systems.

The present solvers are verified using three geometries of varying complexity: a one-dimensional plane-parallel participating medium, a three-dimensional vitiated backward-facing step combustor, and a DNS of a small turbulent pool fire. Frozen field analyses were conducted for all of these configurations. Additionally, the solver is applied to a LES of a larger turbulent pool fire, to demonstrate its applicability in coupled combustion simulations.

One dimensional plane-parallel results compare excellently against exact solutions for all three primary versions of the solver. Tests are conducted for a variety of absorption coefficients, medium temperatures, and ray counts. Radiative absorption increased with absorption coefficient and temperature, and stochastic variability becomes more apparent with lower ray-counts. ArborX-Reverse and Hybrid-Reverse tracing methods demonstrate increased variance near the boundaries and for lower absorption coefficients due to greater numbers of reverse-rays exiting the domain. The solvers demonstrated small differences in

runtime performance for all configurations, and results compare equally well when run with eight MPI ranks.

For the 3-D backward-facing step combustor, results are compared against those of an established Fortran-radiation solver as a further verification. Excellent agreement is obtained between the two solvers. It is found that GPU parallel processing reduces runtimes by approximately two orders of magnitude.

The previous two configurations involve only gray media, while the 3-D DNS of a small pool-fire flame is employed to further verify the implementation of the line-by-line database. Runtimes for various parallel back-ends including GPU, CPU, and serial are compared. Both NVIDIA V100 and NVIDIA A100 GPUs are shown to accelerate the solver over two orders of magnitude, with the A100 showing almost 400 times speedup. OpenMP parallel execution also shows an order of magnitude speedup over serial. To facilitate comparison with two OpenFOAM stock solvers, radiation is simulated again using a uniform-absorption coefficient gray model, and compared amongst the MCRT, fvDOM and P1 solvers. fvDOM is shown to have reasonably good accuracy while P-1 deviates significantly from baseline MCRT results. Meanwhile, the GPU-accelerated MCRT solver is shown to run faster than both serial fvDOM and serial P-1 radiation solutions within a gray medium, indicating its great potential to replace these solvers in time-accurate combustion simulations.

Lastly, a similar turbulent pool fire is simulated from its initial conditions in a transient simulation. Results show a significant decrease in temperature of up to 600 K compared to the simulation without radiation. Detailed account of runtime consumption in the solver within one timestep is described through the use of a Kokkos profiling tool [111]. It is found that a significant portion of the runtime is consumed through the loading and transferal of the line-by-line database. These results were magnified for the GPU, where several deep copies of CPU to GPU memory must be performed. Profiling results display a consistent 25% of the runtime was consumed by radiation for each time-step, on average. Noting the results from the profiling of the frozen-field analysis, it was predicted that the consumption

in runtime would decrease if the mesh and non-gray information are maintained in memory between time-steps, which is recommended as an immediate future development.

## 5.2 Recommendations for Future Work

The present implementation of MCRT with GPUs has shown significant speedup compared to CPU implementations. However, it is anticipated that further speedups can be obtained by implementing improved GPU-favorable memory coalescence and by sorting rays by absorption coefficient [24]. Furthermore, a fully asynchronous computation of radiation and CFD on the GPU and CPU simultaneously would reduce the apparent runtime of radiation to only the communication time between the two. The potential for the Bounding Volume Hierarchy was limited in the present demonstration, however, the BVH may have potential to provide improvements for a larger distributed-memory simulations. Null-collision Monte Carlo has demonstrated significant potential to accelerate MCRT. Combining this method with advanced mesh approaches, such as the BVH, could bring measurable speedups to the ray-tracing calculation. Improvements such as these, along with those presented in this thesis, will enable scientists and engineers to have more complete understanding of the influence of radiation within their combustion systems.

# Bibliography

- [1] Tao Ren and Michael F. Modest. A hybrid wavenumber selection scheme for line-by-line photon Monte Carlo simulations in high- temperature gases. *Journal of Heat Transfer*, 135(8), 2013. ISSN 00221481. doi: 10.1115/1.4024385.
- [2] Nicolas Tricard and Xinyu Zhao. Modeling of conjugate heat transfer within thermal barrier coatings for combustion environments. In *International Symposium on Advances in Computational Heat Transfer*, 2021.
- [3] Bifen Wu, Somesh P Roy, and Xinyu Zhao. Detailed modeling of a small-scale turbulent pool fire. *Combustion and Flame*, 214:224–237, 2020. ISSN 0010-2180. doi: <https://doi.org/10.1016/j.combustflame.2019.12.034>. URL <https://www.sciencedirect.com/science/article/pii/S0010218019305929>.
- [4] E Valendik and Ivan Kosov. Effect of thermal radiation of forest fire on the environment. *Contemporary Problems of Ecology*, 1:399–403, 9 2008. doi: 10.1134/S1995425508040012.
- [5] Michael F. Modest and Daniel C. Haworth. *Radiative Heat Transfer in Turbulent Combustion Systems*. Springer Cham, 1 edition, 2016. ISBN 978-3-319-27289-4. doi: 10.1007/978-3-319-27291-7.
- [6] P J Coelho. Radiative transfer in combustion systems. In *Handbook of Thermal Science and Engineering*, pages 1173–1199. 8 2018. doi: 10.1007/978-3-319-26695-4{\\_\\_}61.
- [7] Fengshan Liu, Jean-Louis Consalvi, Pedro J Coelho, Frédéric Andre, Mingyan Gu, Vladimir Solovjov, and Brent W Webb. The impact of radiative heat transfer in combustion processes and its modeling – with a focus on turbulent flames. *Fuel*, 281: 118555, 2020. ISSN 0016-2361. doi: <https://doi.org/10.1016/j.fuel.2020.118555>. URL <https://www.sciencedirect.com/science/article/pii/S0016236120315519>.
- [8] S Berger, S Richard, F Duchaine, G Staffelbach, and L Y M Gicquel. On the sensitivity of a helicopter combustor wall temperature to convective and radiative thermal loads. *Applied Thermal Engineering*, 103:1450–1459, 2016. ISSN 1359-4311. doi: <https://doi.org/10.1016/j.applthermaleng.2016.04.054>. URL <https://www.sciencedirect.com/science/article/pii/S1359431116305403>.

## BIBLIOGRAPHY

---

- [9] Andressa L. Johnson and Xinyu Zhao. Analysis of the Heat Transfer Within Combustor Liners Using a Combined Monte Carlo and Two-Flux Method. *Journal of Turbomachinery*, 143(3):31006–, 3 2021. ISSN 0889-504X. doi: 10.1115/1.4049913.
- [10] Matthias Ihme and Heinz Pitsch. Modeling of radiation and nitric oxide formation in turbulent nonpremixed flames using a flamelet/progress variable formulation. *Physics of Fluids - PHYS FLUIDS*, 20, 9 2008. doi: 10.1063/1.2911047.
- [11] Ali Habibi, Bart Merci, and D Roekaerts. Turbulence radiation interaction in Reynolds-averaged Navier-Stokes simulations of nonpremixed piloted turbulent laboratory-scale flames. *Combustion and Flame*, 151:303–320, 9 2007. doi: 10.1016/j.combustflame.2007.06.003.
- [12] Tao Ren, Michael Modest, and Somesh Roy. Monte Carlo Simulation for Radiative Transfer in a High-Pressure Industrial Gas Turbine Combustion Chamber. *Journal of Engineering for Gas Turbines and Power*, 140, 1 2017. doi: 10.1115/1.4038153.
- [13] Abdelaziz Gamil, Theoklis Nikolaidis, Indrit Lelaj, and Panagiotis Laskaridis. Assessment of numerical radiation models on the heat transfer of an aero-engine combustion chamber. *Case Studies in Thermal Engineering*, 22:100772, 8 2020. doi: 10.1016/j.csite.2020.100772.
- [14] Bifen Wu, Matthias Ihme, and Xinyu Zhao. Limitations of flamelet formulation for modeling turbulent pool fires. *Combustion and Flame*, 227:346–358, 5 2021. ISSN 00102180. doi: 10.1016/j.combustflame.2021.01.023.
- [15] Michael F Modest and Jun Yang. Elliptic PDE formulation and boundary conditions of the spherical harmonics method of arbitrary order for general three-dimensional geometries. *Journal of Quantitative Spectroscopy and Radiative Transfer*, 109(9):1641–1666, 2008. ISSN 0022-4073. doi: <https://doi.org/10.1016/j.jqsrt.2007.12.018>. URL <https://www.sciencedirect.com/science/article/pii/S0022407307003676>.
- [16] Wenjun Ge, Ricardo Marquez, Michael F. Modest, and Somesh P. Roy. Implementation of High-Order Spherical Harmonics Methods for Radiative Heat Transfer on openfoam. *Journal of Heat Transfer*, 137(5):137–142, 5 2015. ISSN 0022-1481. doi: 10.1115/1.4029546.
- [17] Lionel Tessé, F Dupoirieux, Bernard Zamuner, and Jean Taine. Radiative transfer in real gases using reciprocal and forward Monte Carlo methods and a correlated-k approach. *International Journal of Heat and Mass Transfer*, 45:2797–2814, 8 2002. doi: 10.1016/S0017-9310(02)00009-1.
- [18] M F Modest. *Radiative heat transfer*. Elsevier, 3 edition, 2013. doi: <https://doi.org/10.1016/C2010-0-65874-3>.
- [19] John R. Howell, M. Pinar Menguc, and Robert Siegel. *Thermal Radiation Heat Transfer*. CRC Press, 9 2010. ISBN 9780429190575. doi: 10.1201/9781439894552.

---

## BIBLIOGRAPHY

- [20] Mathieu Galtier, Stéphane Blanco, C Caliot, Christophe Coustet, Jérémie Dauchet, El Hafi Mouna, V Eymet, Richard Fournier, Jacques Gautrais, Anaïs Khuong, B Piaud, and Guillaume Terrée. Integral formulation of null-collision Monte Carlo algorithms. *Journal of Quantitative Spectroscopy and Radiative Transfer*, 125:57–68, 10 2013. doi: 10.1016/j.jqsrt.2013.04.001.
- [21] Michael F Modest and Sandip Mazumder. Chapter 13 - Exact Solutions for One-Dimensional Gray Media. In Michael F Modest and Sandip Mazumder, editors, *Radiative Heat Transfer (Fourth Edition)*, pages 467–495. Academic Press, fourth edition edition, 2022. ISBN 978-0-323-98406-5. doi: <https://doi.org/10.1016/B978-0-12-818143-0.00021-3>. URL <https://www.sciencedirect.com/science/article/pii/B9780128181430000213>.
- [22] John Howell and Kyle Daun. The Past and Future of the Monte Carlo Method in Thermal Radiation Transfer. *Journal of Heat Transfer*, 143, 9 2021. doi: 10.1115/1.4050719.
- [23] Alan Humphrey, Todd Harman, Martin Berzins, and Phillip Smith. A scalable algorithm for radiative heat transfer using reverse monte carlo ray tracing. In *Lecture Notes in Computer Science (including subseries Lecture Notes in Artificial Intelligence and Lecture Notes in Bioinformatics)*, volume 9137 LNCS, 2015. doi: 10.1007/978-3-319-20119-1\\_\\_16.
- [24] Simone Silvestri and Rene Pecnik. A fast GPU Monte Carlo radiative heat transfer implementation for coupling with direct numerical simulation. *Journal of Computational Physics: X*, 3:100032, 8 2019. doi: 10.1016/j.jcpnx.2019.100032.
- [25] Christian R Trott, Damien Lebrun-Grandié, Daniel Arndt, Jan Ciesko, Vinh Dang, Nathan Ellingwood, Rahulkumar Gayatri, Evan Harvey, Daisy S Hollman, Dan Ibanez, Nevin Liber, Jonathan Madsen, Jeff Miles, David Poliakoff, Amy Powell, Sivasankaran Rajamanickam, Mikael Simberg, Dan Sunderland, Bruno Turcksin, and Jeremiah Wilke. Kokkos 3: Programming Model Extensions for the Exascale Era. *IEEE Transactions on Parallel and Distributed Systems*, 33(4):805–817, 2022. doi: 10.1109/TPDS.2021.3097283.
- [26] H G Weller, Gavin Tabor, Hrvoje Jasak, and Christer Fureby. A Tensorial Approach to Computational Continuum Mechanics Using Object Orientated Techniques. *Computers in Physics*, 12:620–631, 8 1998. doi: 10.1063/1.168744.
- [27] Christian Trott, Damien Lebrun-Grandie, Daniel Arndt, Jan Ciesko, Vinh Dang, Nathan Ellingwood, Rahulkumar Gayatri, Evan Harvey, Daisy Hollman, Daniel Ibanez, Nevin Liber, Jonathan Madsen, Jeff Miles, David Poliakoff, Amy Powell, Siva Rajamanickam, Mikael Simberg, Dan Sunderland, Bruno Turcksin, and Jeremiah Wilke. Kokkos 3: Programming Model Extensions for the Exascale Era. *IEEE Transactions on Parallel and Distributed Systems*, PP:1, 8 2021. doi: 10.1109/TPDS.2021.3097283.

---

## BIBLIOGRAPHY

- [28] D Lebrun-Grandié, Andrey Prokopenko, B Turcksin, and S Slattery. ArborX: A Performance Portable Search Library, 8 2019.
- [29] Michael F Modest and Sandip Mazumder. Chapter 1 - Fundamentals of Thermal Radiation. In Michael F Modest and Sandip Mazumder, editors, *Radiative Heat Transfer (Fourth Edition)*, pages 1–29. Academic Press, fourth edition edition, 2022. ISBN 978-0-323-98406-5. doi: <https://doi.org/10.1016/B978-0-12-818143-0.00009-2>. URL <https://www.sciencedirect.com/science/article/pii/B9780128181430000092>.
- [30] R. Viskanta and E. E. Anderson. Heat Transfer in Semitransparent Solids. *Advances in Heat Transfer*, 11(C):317–441, 1 1975. ISSN 00652717. doi: 10.1016/S0065-2717(08)70077-7.
- [31] Ronald Hanson, Raymond Spearrin, and Christopher Goldenstein. *Spectroscopy and Optical Diagnostics for Gases*. 8 2016. ISBN 9783319232515. doi: 10.1007/978-3-319-23252-2.
- [32] L S Rothman, I E Gordon, R J Barber, H Dothe, R R Gamache, A Goldman, V I Perevalov, S A Tashkun, and J Tennyson. HITEMP, the high-temperature molecular spectroscopic database. *Journal of Quantitative Spectroscopy and Radiative Transfer*, 111(15):2139 – 2150, 2010. ISSN 0022-4073. doi: <https://doi.org/10.1016/j.jqsrt.2010.05.001>. URL <http://www.sciencedirect.com/science/article/pii/S002240731000169X>.
- [33] Michael E Mueller and Heinz Pitsch. Large eddy simulation of soot evolution in an aircraft combustor. *Physics of Fluids*, 25(11):110812, 2013. doi: 10.1063/1.4819347. URL <https://doi.org/10.1063/1.4819347>.
- [34] Michael F Modest and Sandip Mazumder. Chapter 14 - Approximate Solution Methods for One-Dimensional Media. In Michael F Modest and Sandip Mazumder, editors, *Radiative Heat Transfer (Fourth Edition)*, pages 497–511. Academic Press, fourth edition edition, 2022. ISBN 978-0-323-98406-5. doi: <https://doi.org/10.1016/B978-0-12-818143-0.00022-5>. URL <https://www.sciencedirect.com/science/article/pii/B9780128181430000225>.
- [35] Shih-I Pai. *Radiation Gas Dynamics*. Springer, Vienna, 1 edition, 1966. ISBN 978-3-7091-5733-6. doi: 10.1007/978-3-7091-5730-5.
- [36] Longhua Hu. A review of physics and correlations of pool fire behaviour in wind and future challenges. *Fire Safety Journal*, 91:41–55, 2017. ISSN 0379-7112. doi: <https://doi.org/10.1016/j.firesaf.2017.05.008>. URL <https://www.sciencedirect.com/science/article/pii/S0379711217303405>.
- [37] Dougal Drysdale. *An Introduction to Fire Dynamics*. Wiley, 3 edition, 8 2011. ISBN 9780470319031. doi: 10.1002/9781119975465.
- [38] J F Sacadura. Radiative heat transfer in fire safety science. *Journal of Quantitative Spectroscopy and Radiative Transfer*, 93(1):5–24, 2005. ISSN 0022-4073. doi: <https://doi.org/10.1016/j.jqsrt.2004.09.001>.

---

## BIBLIOGRAPHY

- //doi.org/10.1016/j.jqsrt.2004.08.011. URL <https://www.sciencedirect.com/science/article/pii/S0022407304003188>.
- [39] Bifen Wu and Xinyu Zhao. Radiation characteristics of water droplets in a fire-inspired environment: A Monte Carlo ray tracing study. *Journal of Quantitative Spectroscopy and Radiative Transfer*, 212:97–111, 2018. ISSN 0022-4073. doi: <https://doi.org/10.1016/j.jqsrt.2018.03.023>. URL <https://www.sciencedirect.com/science/article/pii/S0022407318300360>.
  - [40] Mark A Finney, Jack D Cohen, Sara S McAllister, and W Matt Jolly. On the need for a theory of wildland fire spread. *International Journal of Wildland Fire*, 22(1):25, 2013. doi: 10.1071/wf11117. URL <https://doi.org/10.1071%2Fwf11117>.
  - [41] Sheldon R Tieszen. ON THE FLUID MECHANICS OF FIRES. *Annual Review of Fluid Mechanics*, 33(1):67–92, 2001. doi: 10.1146/annurev.fluid.33.1.67. URL <https://doi.org/10.1146/annurev.fluid.33.1.67>.
  - [42] Baki M Cetegen and Tarek A Ahmed. Experiments on the periodic instability of buoyant plumes and pool fires. *Combustion and Flame*, 93(1):157–184, 1993. ISSN 0010-2180. doi: [https://doi.org/10.1016/0010-2180\(93\)90090-P](https://doi.org/10.1016/0010-2180(93)90090-P). URL <https://www.sciencedirect.com/science/article/pii/001021809390090P>.
  - [43] Yuhang Chen, Jun Fang, Xiaolei Zhang, Yanli Miao, Yujie Lin, Ran Tu, and Longhua Hu. Pool fire dynamics: Principles, models and recent advances. *Progress in Energy and Combustion Science*, 95:101070, 2023. ISSN 0360-1285. doi: <https://doi.org/10.1016/j.pecs.2022.101070>. URL <https://www.sciencedirect.com/science/article/pii/S0360128522000776>.
  - [44] Anthony Hamins, Takashi Kashiwagi, and R Buch. Characteristics of Pool Fire Burning. American Resistance of Industrial Fluids, Indianapolis, IN, 3 1995. URL [https://tsapps.nist.gov/publication/get\\_pdf.cfm?pub\\_id=909541](https://tsapps.nist.gov/publication/get_pdf.cfm?pub_id=909541).
  - [45] Koseki Hiroshi and Yumoto Taro. Air entrainment and thermal radiation from heptane pool fires. *Fire Technology*, 24(1):33–47, 1988. ISSN 1572-8099. doi: 10.1007/BF01039639. URL <https://doi.org/10.1007/BF01039639>.
  - [46] Zhang Miao, Song Wenhua, Wang Ji, and Chen Zhen. Accident Consequence Simulation Analysis of Pool Fire in Fire Dike. *Procedia Engineering*, 84:565–577, 2014. ISSN 1877-7058. doi: <https://doi.org/10.1016/j.proeng.2014.10.469>. URL <https://www.sciencedirect.com/science/article/pii/S1877705814017901>.
  - [47] Genong Li. *Investigation of turbulence-radiation interactions by a hybrid FV/PDF Monte Carlo method*. PhD thesis, Pennsylvania State University, University Park, 5 2002.
  - [48] Anquan Wang, Michael F Modest, Daniel C Haworth, and Liangyu Wang. Monte Carlo simulation of radiative heat transfer and turbulence interactions in methane/air

---

## BIBLIOGRAPHY

- jet flames. *Journal of Quantitative Spectroscopy and Radiative Transfer*, 109(2):269–279, 2008. ISSN 0022-4073. doi: <https://doi.org/10.1016/j.jqsrt.2007.08.030>. URL <https://www.sciencedirect.com/science/article/pii/S0022407307002464>.
- [49] J L Consalvi. Influence of turbulence–radiation interactions in laboratory-scale methane pool fires. *International Journal of Thermal Sciences*, 60:122–130, 2012. ISSN 1290-0729. doi: <https://doi.org/10.1016/j.ijthermalsci.2012.05.013>. URL <https://www.sciencedirect.com/science/article/pii/S1290072912001639>.
- [50] Nitin Padture. Advanced structural ceramics in aerospace propulsion. *Nature Materials*, 15:804–809, 1 2016. doi: 10.1038/nmat4687.
- [51] Ryoichi Amano and Bengt Sundén. *Thermal Engineering in Power Systems*, volume 22. 2 2008. ISBN 978-1-84564-062-0.
- [52] Arthur H Lefebvre. Flame radiation in gas turbine combustion chambers. *International Journal of Heat and Mass Transfer*, 27(9):1493–1510, 1984. ISSN 0017-9310. doi: [https://doi.org/10.1016/0017-9310\(84\)90262-X](https://doi.org/10.1016/0017-9310(84)90262-X). URL <https://www.sciencedirect.com/science/article/pii/001793108490262X>.
- [53] Russell Claus. Spectral Flame Radiance From a Tubular-Can Combustor . Technical report, NASA Lewis, Cleveland, OH, 2 1981.
- [54] M. C. Paul and W. P. Jones. Radiative heat transfer in a model gas turbine combustor. In *Advanced Computational Methods in Heat Transfer IX*, pages 413–421, Southampton, UK, 6 2006. WIT Press. ISBN 1845641760. doi: 10.2495/HT060401.
- [55] Prakash Ghose, Jitendra Patra, Amitava Datta, and Achintya Mukhopadhyay. Prediction of soot and thermal radiation in a model gas turbine combustor burning kerosene fuel spray at different swirl levels. *Combustion Theory and Modelling*, 20(3):457–485, 2016. doi: 10.1080/13647830.2016.1147607. URL <https://doi.org/10.1080/13647830.2016.1147607>.
- [56] George Sutton and Oscar Biblarz. Rocket Propulsion Elements. *JOHN WILEY & SONS, INC.*, 7, 2001.
- [57] Mohammad Naraghi, Stuart Dunn, and Douglas Coats. Modeling of Radiation Heat Transfer in Liquid Rocket Engines. In *41st AIAA/ Joint Propulsion Conference*, Tucson, Arizona, 7 2005. American Institute of Aeronautics and Astronautics. ISBN 978-1-62410-063-5. doi: 10.2514/6.2005-3935.
- [58] Marco Pizzarelli. Overview and analysis of the experimentally measured throat heat transfer in liquid rocket engine thrust chambers. *Acta Astronautica*, 184:46–58, 2021. ISSN 0094-5765. doi: <https://doi.org/10.1016/j.actaastro.2021.03.028>. URL <https://www.sciencedirect.com/science/article/pii/S0094576521001417>.

---

## BIBLIOGRAPHY

- [59] Giuseppe Lecce, Daniele Bianchi, Barbara Betti, Diego Lentini, and Francesco Nasuti. Convective and Radiative Wall Heat Transfer in Liquid Rocket Thrust Chambers. *Journal of Propulsion and Power*, 34(2):318–326, 3 2018. ISSN 0748-4658. doi: 10.2514/1.B36589.
- [60] Giuseppe Lecce, Daniele Bianchi, and Francesco Nasuti. Numerical Investigation on Radiative Heat Loads in Liquid Rocket Thrust Chambers. *Journal of Propulsion and Power*, 35(5):930–943, 9 2019. ISSN 1533-3876. doi: 10.2514/1.B37536.
- [61] R Viskanta and M P Mengüç. Radiation heat transfer in combustion systems. *Progress in Energy and Combustion Science*, 13(2):97–160, 1987. ISSN 0360-1285. doi: [https://doi.org/10.1016/0360-1285\(87\)90008-6](https://doi.org/10.1016/0360-1285(87)90008-6). URL <https://www.sciencedirect.com/science/article/pii/0360128587900086>.
- [62] Quentin Flamant and David R Clarke. Opportunities for minimizing radiative heat transfer in future thermal and environmental barrier coatings. *Scripta Materialia*, 173: 26–31, 2019. ISSN 1359-6462. doi: <https://doi.org/10.1016/j.scriptamat.2019.07.041>. URL <https://www.sciencedirect.com/science/article/pii/S135964621930449X>.
- [63] R. A. Miller. Thermal barrier coatings for aircraft engines: history and directions. *Journal of Thermal Spray Technology*, 6(1):35–42, 3 1997. ISSN 1059-9630. doi: 10.1007/BF02646310.
- [64] N. P. Padture. Thermal Barrier Coatings for Gas-Turbine Engine Applications. *Science*, 296(5566):280–284, 4 2002. ISSN 00368075. doi: 10.1126/science.1068609.
- [65] Robert Siegel and Charles M. Spuckler. Analysis of thermal radiation effects on temperatures in turbine engine thermal barrier coatings. *Materials Science and Engineering A*, 245(2):150–159, 5 1998. ISSN 09215093. doi: 10.1016/S0921-5093(97)00845-9.
- [66] G. Boissonnet, G. Bonnet, A. Pasquet, N. Bourhila, and F. Pedraza. Evolution of thermal insulation of plasma-sprayed thermal barrier coating systems with exposure to high temperature. *Journal of the European Ceramic Society*, 39(6):2111–2121, 6 2019. ISSN 09552219. doi: 10.1016/j.jeurceramsoc.2019.01.026.
- [67] C. M. Spuckler and R. Siegel. Two-Flux and Diffusion Methods for Radiative Transfer in Composite Layers. *Journal of Heat Transfer*, 118(1):218–222, 2 1996. ISSN 0022-1481. doi: 10.1115/1.2824043.
- [68] Robert Siegel. Internal radiation effects in zirconia thermal barrier coatings. *Journal of Thermophysics and Heat Transfer*, 10(4):707–709, 10 1996. ISSN 0887-8722. doi: 10.2514/3.851.
- [69] E. A. Milne. Thermodynamics of the Stars. In *Handbuch der Astrophysik*, pages 65–255. Springer Berlin Heidelberg, Berlin, Heidelberg, 1930. doi: 10.1007/978-3-642-90705-0{\\_}2.

---

## BIBLIOGRAPHY

- [70] A. S. Eddington. The Internal Constitution of the Stars. *Nature*, 106(2653):14–20, 9 1920. ISSN 0028-0836. doi: 10.1038/106014a0.
- [71] G Yang, C Y Zhao, and B X Wang. Experimental study on radiative properties of air plasma sprayed thermal barrier coatings. *International Journal of Heat and Mass Transfer*, 66:695–698, 2013. ISSN 0017-9310. doi: <https://doi.org/10.1016/j.ijheatmasstransfer.2013.07.069>. URL <https://www.sciencedirect.com/science/article/pii/S0017931013006236>.
- [72] Yiguang Ju, Goro Masuya, Fengshan Liu, Yuji Hattori, and Dirk Riechelmann. Asymptotic analysis of radiation extinction of stretched premixed flames. *International Journal of Heat and Mass Transfer*, 43(2):231–239, 2000. ISSN 0017-9310. doi: [https://doi.org/10.1016/S0017-9310\(99\)00130-1](https://doi.org/10.1016/S0017-9310(99)00130-1). URL <https://www.sciencedirect.com/science/article/pii/S0017931099001301>.
- [73] K N Lakshmisha, P J Paul, and H S Mukunda. On the flammability limit and heat loss in flames with detailed chemistry. *Symposium (International) on Combustion*, 23(1): 433–440, 1991. ISSN 0082-0784. doi: [https://doi.org/10.1016/S0082-0784\(06\)80288-2](https://doi.org/10.1016/S0082-0784(06)80288-2). URL <https://www.sciencedirect.com/science/article/pii/S0082078406802882>.
- [74] Yiguang Ju, Goro Masuya, and Paul D Ronney. Effects of radiative emission and absorption on the propagation and extinction of premixed gas flames. *Symposium (International) on Combustion*, 27(2):2619–2626, 1998. ISSN 0082-0784. doi: [https://doi.org/10.1016/S0082-0784\(98\)80116-1](https://doi.org/10.1016/S0082-0784(98)80116-1). URL <https://www.sciencedirect.com/science/article/pii/S0082078498801161>.
- [75] Raymond Viskanta. Radiative transfer in combustion systems, 9 2010.
- [76] Paul R Medwell, Graham J Nathan, Qing N Chan, Zeyad T Alwahabi, and Bassam B Dally. The influence on the soot distribution within a laminar flame of radiation at fluxes of relevance to concentrated solar radiation. *Combustion and Flame*, 158(9): 1814–1821, 2011. ISSN 0010-2180. doi: <https://doi.org/10.1016/j.combustflame.2011.01.006>. URL <https://www.sciencedirect.com/science/article/pii/S0010218011000216>.
- [77] Alan Humphrey, Daniel Sunderland, Todd Harman, and Martin Berzins. Radiative Heat Transfer Calculation on 16384 GPUs Using a Reverse Monte Carlo Ray Tracing Approach with Adaptive Mesh Refinement. pages 1222–1231, 8 2016. doi: 10.1109/IPDPSW.2016.93.
- [78] Michael F Modest and Sandip Mazumder. Chapter 20 - The Monte Carlo Method for Participating Media. In Michael F Modest and Sandip Mazumder, editors, *Radiative Heat Transfer (Fourth Edition)*, pages 737–773. Academic Press, fourth edition edition, 2022. ISBN 978-0-323-98406-5. doi: <https://doi.org/10.1016/B978-0-12-818143-0.00028-6>. URL <https://www.sciencedirect.com/science/article/pii/B9780128181430000286>.
- [79] John Amanatides and Andrew Woo. A Fast Voxel Traversal Algorithm for Ray Tracing. *Proceedings of EuroGraphics*, 87, 10 1987.

---

## BIBLIOGRAPHY

- [80] Alan Humphrey, Qingyu Meng, Martin Berzins, and Todd Harman. Radiation modeling using the Uintah heterogeneous CPU/GPU runtime system. *ACM International Conference Proceeding Series*, 8 2012. doi: 10.1145/2335755.2335791.
- [81] Charles Zeeb and John Dolaghan. An Efficient Monte Carlo Particle Tracing Algorithm for Large, Arbitrary Geometries. *Numerical Heat Transfer Part B - Fundamentals*, 39, 9 2001. doi: 10.1080/104077901750106606.
- [82] Timothy L Kay and James T Kajiya. Ray Tracing Complex Scenes. In *Proceedings of the 13th Annual Conference on Computer Graphics and Interactive Techniques*, SIGGRAPH '86, pages 269–278, New York, NY, USA, 1986. Association for Computing Machinery. ISBN 0897911962. doi: 10.1145/15922.15916. URL <https://doi.org/10.1145/15922.15916>.
- [83] D Sunday. *Practical Geometry Algorithms: With C++ Code*. Amazon Digital Services LLC - KDP Print US, 2021. ISBN 9798749449730. URL <https://books.google.com/books?id=YBN0zgEACAAJ>.
- [84] Anquan Wang and Michael F Modest. An adaptive emission model for Monte Carlo simulations in highly inhomogeneous media represented by stochastic particle fields. *Journal of Quantitative Spectroscopy and Radiative Transfer*, 104(2):288–296, 2007. ISSN 0022-4073. doi: <https://doi.org/10.1016/j.jqsrt.2006.07.023>. URL <https://www.sciencedirect.com/science/article/pii/S0022407306001920>.
- [85] K Case. Transfer Problems and the Reciprocity Principle. *Revs. Mod. Phys.*, Vol: 29, 10 1957. doi: 10.1103/RevModPhys.29.651.
- [86] X Lu and Pei-Feng Hsu. Reverse Monte Carlo Method for Transient Radiative Transfer in Participating Media. *Journal of Heat Transfer-Transactions of the Asme*, 126:621–627, 10 2004. doi: 10.1115/IMECE2003-41932.
- [87] B X Li, X J Yu, and L H Liu. Backward Monte Carlo simulation for apparent directional emissivity of non-isothermal semitransparent slab. *Journal of Quantitative Spectroscopy and Radiative Transfer*, 91:173–179, 10 2005. doi: 10.1016/j.jqsrt.2004.05.055.
- [88] Donald V Walters and Richard O Buckius. Rigorous development for radiation heat transfer in nonhomogeneous absorbing, emitting and scattering media. *International Journal of Heat and Mass Transfer*, 35(12):3323–3333, 12 1992.
- [89] Michael F. Modest. Backward Monte Carlo simulations in radiative heat transfer. *Journal of Heat Transfer*, 125(1), 2003. ISSN 00221481. doi: 10.1115/1.1518491.
- [90] John R. Howell, M. Pinar Mengüç, Kyle Daun, and Robert Siegel. *Thermal Radiation Heat Transfer*. CRC Press, Seventh edition. | Boca Raton : CRC Press, 2021. | Revised edition of: Thermal radiation heat transfer / John R. Howell, M. Pinar Menguc, Robert Siegel. Sixth edition. 2015., 7th edition, 12 2020. ISBN 9780429327308. doi: 10.1201/9780429327308.

---

## BIBLIOGRAPHY

- [91] Francis Dupoirieux, Lionel Tessé, Sébastien Avila, and Jean Taine. An optimized reciprocity Monte Carlo method for the calculation of radiative transfer in media of various optical thicknesses. *International Journal of Heat and Mass Transfer*, 49(7):1310–1319, 2006. ISSN 0017-9310. doi: <https://doi.org/10.1016/j.ijheatmasstransfer.2005.10.009>. URL <https://www.sciencedirect.com/science/article/pii/S0017931005006289>.
- [92] Vincent Eymet, Damien Poitou, M Galtier, Mouna El-Hafi, Guillaume Terrée, and Richard A Fournier. Null-collision meshless Monte-Carlo-Application to the validation of fast radiative transfer solvers embedded in combustion simulators. *Journal of Quantitative Spectroscopy and Radiative Transfer*, 129:145–157, 11 2013. doi: 10.1016/j.jqsrt.2013.06.004. URL <https://hal.archives-ouvertes.fr/hal-01688108>.
- [93] Mouna El Hafi, Stephane Blanco, Jérémie Dauchet, Richard Fournier, Mathieu Galtier, Loris Ibarrart, Jean-Marc Tregan, and Najda Villefranque. Three viewpoints on null-collision Monte Carlo algorithms. *Journal of Quantitative Spectroscopy and Radiative Transfer*, 260:107402, 2021. ISSN 0022-4073. doi: <https://doi.org/10.1016/j.jqsrt.2020.107402>. URL <https://www.sciencedirect.com/science/article/pii/S0022407320302983>.
- [94] Mathieu Galtier, Stéphane Blanco, Jérémie Dauchet, El Hafi Mouna, Vincent Eymet, Richard Fournier, Maxime Roger, Christophe Spiesser, and Guillaume Terrée. Radiative transfer and spectroscopic databases: A line-sampling Monte Carlo approach. *Journal of Quantitative Spectroscopy and Radiative Transfer*, 172, 10 2015. doi: 10.1016/j.jqsrt.2015.10.016.
- [95] Najda Villefranque, Richard Fournier, Fleur Couvreux, Stéphane Blanco, Céline Cornet, Vincent Eymet, Vincent Forest, and Jean-Marc Tregan. A Path-Tracing Monte Carlo Library for 3-D Radiative Transfer in Highly Resolved Cloudy Atmospheres. *Journal of Advances in Modeling Earth Systems*, 11(8):2449–2473, 2019. doi: <https://doi.org/10.1029/2018MS001602>. URL <https://agupubs.onlinelibrary.wiley.com/doi/abs/10.1029/2018MS001602>.
- [96] Stephan Kelm, Manohar Kampili, Xiongguo Liu, Allen George, Daniel Schumacher, Claudia Druska, Stephan Struth, Astrid Kuhr, Lucian Ramacher, Hans-Josef Allelein, K Arul Prakash, G Vijaya Kumar, Liam M F Cammiade, and Ruiyun Ji. The Tailored CFD Package 'containmentFOAM' for Analysis of Containment Atmosphere Mixing, H<sub>2</sub>/CO Mitigation and Aerosol Transport. 2021. doi: 10.3390/fluids6030100. URL <https://doi.org/10.3390/fluids6030100>.
- [97] Pradeep Gupta. CUDA Refresher: Reviewing the Origins of GPU Computing, 4 2020.
- [98] Brian Caulfield. What's the Difference Between a CPU and a GPU?, 12 2009. URL <https://blogs.nvidia.com/blog/2009/12/16/whats-the-difference-between-a-cpu-and-a-gpu/>.
- [99] Erik Alerstam, Tomas Svensson, and Stefan Andersson-Engels. Parallel computing with graphics processing units for high-speed Monte Carlo simulation of photon mi-

---

## BIBLIOGRAPHY

- gration. *Journal of Biomedical Optics*, 13(6):60504, 2008. doi: 10.1117/1.3041496. URL <https://doi.org/10.1117/1.3041496>.
- [100] Frank Heymann and Ralf Siebenmorgen. GPU-based Monte Carlo dust radiative transfer scheme applied to AGN. *Astrophysical Journal*, 751, 9 2012. doi: 10.1088/0004-637X/751/1/27.
  - [101] John Holmen, Alan Humphrey, Daniel Sunderland, and Martin Berzins. Improving Uintah’s Scalability Through the Use of Portable Kokkos-Based Data Parallel Tasks. pages 1–8, 9 2017. doi: 10.1145/3093338.3093388.
  - [102] Peter Shirley. Ray Tracing: The Next Week, 12 2020. URL <https://raytracing.github.io/books/RayTracingTheNextWeek.html>.
  - [103] Daniel Meister, Shinji Ogaki, Carsten Benthin, Michael Doyle, Michael Guthe, and Jiri Bittner. A Survey on Bounding Volume Hierarchies for Ray Tracing. *Computer Graphics Forum*, 40:683–712, 9 2021. doi: 10.1111/cgf.142662.
  - [104] Alexandre Solon Nery, Nadia Nedjah, Felipe Maia Galvão França, and Lech Józwiak. Parallel processing of intersections for ray-tracing in application-specific processors and GPGPUs. *Microprocess. Microsystems*, 37:739–749, 2013.
  - [105] Tero Karras. Maximizing Parallelism in the Construction of BVHs, Octrees, and k-d Trees. In *Proceedings of the Fourth ACM SIGGRAPH/Eurographics conference on High-Performance Graphics*, pages 33–37, 8 2012. doi: 10.2312/EGGH/HPG12/033-037.
  - [106] P Kuczyńska and Ryszard Bialecki. Radiation heat transfer model using Monte Carlo ray tracing method on hierarchical ortho-Cartesian meshes and non-uniform rational basis spline surfaces for description of boundaries. *Archives of Thermodynamics*, 35: 65–92, 9 2014. doi: 10.2478/aoter-2014-0014.
  - [107] Sandip Mazumder. Methods to Accelerate Ray Tracing in the Monte Carlo Method for Surface-to-Surface Radiation Transport. *Journal of Heat Transfer*, 128:945, 8 2006. doi: 10.1115/1.2241978.
  - [108] Waad Safty, Peter Camps, Maarten Baes, K Gordon, Sebastiaan Vandewoude, Awat Rahimi, and Marko Stalevski. Using hierarchical octrees in Monte Carlo radiative transfer simulations (Research Note). *Astronomy and Astrophysics*, 554:10, 9 2013. doi: 10.1051/0004-6361/201220854.
  - [109] Tao Ren and Michael F. Modest. Line-by-line random-number database for Monte Carlo simulations of radiation in combustion system. *Journal of Heat Transfer*, 141 (2), 2019. ISSN 15288943. doi: 10.1115/1.4041803.
  - [110] H Carter Edwards, Christian R Trott, and Daniel Sunderland. Kokkos: Enabling many-core performance portability through polymorphic memory access patterns . *Journal of Parallel and Distributed Computing*, 74(12):3202 – 3216, 2014. ISSN 0743-7315.

## BIBLIOGRAPHY

---

- doi: <https://doi.org/10.1016/j.jpdc.2014.07.003>. URL <http://www.sciencedirect.com/science/article/pii/S0743731514001257>.
- [111] Christian Trott, Luc Berger-Vergiat, David Poliakoff, Sivasankaran Rajamanickam, Damien Lebrun-Grandie, Jonathan Madsen, Nader Al Awar, Milos Gligoric, Galen Shipman, and Geoff Womeldorff. The Kokkos EcoSystem: Comprehensive Performance Portability for High Performance Computing. *Computing in Science Engineering*, 23(5):10–18, 2021. doi: 10.1109/MCSE.2021.3098509.
  - [112] Michael F Modest and Sandip Mazumder. Chapter 7 - The Monte Carlo Method for Surface Exchange. In Michael F Modest and Sandip Mazumder, editors, *Radiative Heat Transfer (Fourth Edition)*, pages 235–259. Academic Press, fourth edition edition, 2022. ISBN 978-0-323-98406-5. doi: <https://doi.org/10.1016/B978-0-12-818143-0.00015-8>. URL <https://www.sciencedirect.com/science/article/pii/B9780128181430000158>.
  - [113] Jeffery T Farmer and John R Howell. Comparison of Monte Carlo Strategies for Radiative Transfer in Participating Media. volume 31 of *Advances in Heat Transfer*, pages 333–429. Elsevier, 1998. doi: [https://doi.org/10.1016/S0065-2717\(08\)70243-0](https://doi.org/10.1016/S0065-2717(08)70243-0). URL <https://www.sciencedirect.com/science/article/pii/S0065271708702430>.
  - [114] B Armaly, F Durst, Jose Pereira, and B Schönung. Experimental and Theoretical Investigation of Backward-Facing Step Flow. *Journal of Fluid Mechanics*, 127:473 – 496, 9 1983. doi: 10.1017/S0022112083002839.
  - [115] Aristeu Neto, Grand Dominique, Olivier Metais, and Lesieur Marcel. A numerical investigation of coherent vortices in turbulence behind a backward-facing step. *Journal of Fluid Mechanics*, 256:1 – 25, 9 1993. doi: 10.1017/S0022112093002691.
  - [116] Srba Jovic and David Driver. Backward-facing step measurements at low Reynolds number,  $Re_{\text{sub h}} = 5000$ . *NASA Technical Memorandum 108807*, 9 1994.
  - [117] Hung Le, Parviz Moin, and John Kim. Direct Numerical Simulation of Turbulent Flow over a Backward-Facing Step. *Journal of Fluid Mechanics*, 330, 9 1997. doi: 10.1017/S0022112096003941.
  - [118] Martin Niemann and Jochen Fröhlich. Buoyancy-affected backward-facing step flow with heat transfer at low Prandtl number. *International Journal of Heat and Mass Transfer*, 101:1237–1250, 9 2016. doi: 10.1016/j.ijheatmasstransfer.2016.05.137.
  - [119] W A Xie and G N Xi. Geometry effect on flow fluctuation and heat transfer in unsteady forced convection over backward and forward facing steps. *Energy*, 132, 9 2017. doi: 10.1016/j.energy.2017.05.072.
  - [120] Paul Pouech, Florent Duchaine, and Thierry Poinsot. Premixed flame ignition in high-speed flows over a backward facing step. *Combustion and Flame*, 229:111398, 9 2021. doi: 10.1016/j.combustflame.2021.111398.

---

## BIBLIOGRAPHY

- [121] Jennifer Colborn and Jacqueline A O'Connor. Variation in Convective and Radiative Heat Transfer with Reynolds Number and Temperature in a Backward-Facing Step Combustor. In *AIAA SCITECH 2023 Forum*, 2023. doi: 10.2514/6.2023-0923. URL <https://arc.aiaa.org/doi/abs/10.2514/6.2023-0923>.
- [122] Julian Toumey. Development of a Large Eddy Simulation Solver with Conjugate Convective and Radiative Heat Transfer, 8 2021.
- [123] R S Barlow and J H Frank. Effects of turbulence on species mass fractions in methane/air jet flames. *Symposium (International) on Combustion*, 27(1):1087–1095, 1998. ISSN 0082-0784. doi: [https://doi.org/10.1016/S0082-0784\(98\)80510-9](https://doi.org/10.1016/S0082-0784(98)80510-9). URL <https://www.sciencedirect.com/science/article/pii/S0082078498805109>.
- [124] Bifen Wu, Xinyu Zhao, Bikram Roy Chowdhury, Baki M Cetegen, Chao Xu, and Tianfeng Lu. A numerical investigation of the flame structure and blowoff characteristics of a bluff-body stabilized turbulent premixed flame. *Combustion and Flame*, 202:376–393, 2019. ISSN 0010-2180. doi: <https://doi.org/10.1016/j.combustflame.2019.01.026>. URL <https://www.sciencedirect.com/science/article/pii/S0010218019300446>.